

THE EFFECTS OF CONDUCTIVE WELL CASINGS ON ELECTROMAGNETIC
SURVEYS: EXPERIMENTAL STUDIES AND NUMERICAL MODELLING

by

Ethan Cole Anderson

A thesis submitted to the Faculty and the Board of Trustees of the Colorado School of Mines in partial fulfillment of the requirements for the degree of Master of Science (Geophysics).

Golden, Colorado

Date _____

Signed: _____

Ethan Anderson

Signed: _____

Dr. Andrei Swidinsky

Thesis Advisor

Golden, Colorado

Date _____

Signed: _____

Dr. John Bradford

Professor and Head

Department of Geophysics

ABSTRACT

Controlled source electromagnetic (CSEM) surveys can be used in petroleum exploration to supplement seismic reflection data because electrical resistivity is highly sensitive to pore space fluid content. Traditionally, CSEM has been used in greenfields exploration, but the method has the potential for application later in the life of a producing field. However, such monitoring would be performed in the presence of electrically conductive steel infrastructure, such as well casings and pipelines. These features introduce considerable artifacts into data gathered for development, production and monitoring purposes. Numerical techniques can be used to model and remove the electromagnetic response from steel infrastructure; one such is the Method of Moments (MoM), which is being actively developed at Mines and will be used throughout this thesis to support experimental data.

Although characterizing the effects of steel infrastructure on EM data is of ultimate interest to industry, much can be learned by studying the zero-frequency DC resistivity counterpart of the finite frequency (AC) problem. Throughout this thesis I theoretically examine the relationship between EM data and well casing properties to best design proper experiments at the lab and field scales. In particular, I examine the relationships between the casing response and properties such as length, width, wall thickness and material composition of the casing. I then describe experimental DC resistivity data that I have collected at three scales: lab, mid-, and large-scale and compare results to those predicted by MoM. Modelled responses in zones dominated by the casing response show differences of less than 20% when compared with experimental data, providing confidence in the MoM method. Results show that the most important parameters affecting casing responses are the orientation of the casing with respect to survey geometry, total volume of metal present in the casing, and the casing material - an important finding as industry casings vary extensively in physical properties. Finally, I discuss a series of AC modelling tests conducted at the same three scales to understand the viability of further EM experiments. Results indicate that at the mid-scale and large-scale, such experiments should be possible using transmitting frequencies of 50 kHz and 1 kHz, respectively; however, lab-scale tests will require transmitting frequencies too high for standard EM equipment.

TABLE OF CONTENTS

ABSTRACT.....	iii
LIST OF FIGURES	vii
LIST OF TABLES.....	xvii
ACKNOWLEDGMENTS	xviii
CHAPTER 1 INTRODUCTION	1
1.1 Background.....	1
1.2 Marine CSEM Background.....	3
1.3 Marine CSEM in the Presence of Conductive Infrastructure	5
1.4 Thesis Outline	5
CHAPTER 2 THEORY AND FINITE-ELEMENT MODELLING FOR EXPERIMENTAL STUDIES.....	8
2.1 An Analytic Expression for Electric Fields in a Wholespace.....	8
2.1.1 Derivation of Analytic Expression for our Interaction Matrix	8
2.1.2 Derivation of Analytic Expression for Both Primary and Secondary Electric Fields	11
2.1.3 Analytic VS MoM Accuracy Check	13
2.2 Field Variations with Changing Casing Properties: Analytic Solution	15
2.2.1 Analysis of Analytic Expressions for Cross-Sectional Area	17
2.2.2 Analysis of Analytic Expressions for Varying Length	18
2.2.3 Analysis of Analytic Expressions for Varying Casing Width	19
2.2.4 Analysis of Analytic Expression for Host Conductivity.....	20
2.3 Field Variations with Changing Casing Properties: MoM Solution.....	21
2.3.1 Analysis of Fully Converged MoM Solution for Cross-Sectional Area...21	
2.3.2 Analysis of Fully Converged MoM Solution for Varying Length	23
2.3.3 Analysis of Fully Converged MoM Solution for Varying Casing Width..25	
2.3.4 Analysis of Fully Converged MoM Solution for Host Conductivity	26
2.4 Theory Conclusions	27
2.5 Finite-Element Modelling.....	29
2.5.1 Model Parameters	29

2.5.2	Model Results and Conclusions.....	33
CHAPTER 3	DC RESISTIVITY EXPERIMENTS AND COMPARISONS WITH METHOD OF MOMENTS MODELLING	37
3.1	Introduction of Lab-Scale Experimental and Method of Moments Data	37
3.1.1	Homogeneous Lab-Scale Data.....	38
3.1.2	Control Casing Lab-Scale and Method of Moments Data.....	39
3.1.3	A Study on the Secondary Field with Changing Casing Width.....	44
3.1.4	The Mystery of an Asymmetric Pant Leg.....	48
3.1.5	A Study on the Secondary Field with Changing Casing Length	50
3.1.6	A Study on the Secondary Field with Changing Wall Thickness.....	54
3.1.7	A Study on the Secondary Field with Changing Casing Material	59
3.1.8	On the Effects of Varying Casing Positioning.....	61
3.1.9	On Multiple Adjacent Casings.....	66
3.1.10	Lab-Scale Experiment Conclusions.....	76
3.2	Introduction of Mid-Scale Experimental and Method of Moments Data	80
3.2.1	Analysis of Vertical Borehole Survey	81
3.2.2	Analysis of Horizontal Aluminum Pipe Survey	85
3.2.3	Mid-Scale Conclusions	89
3.3	Introduction of Large-Scale Experimental and Method of Moments Data	89
3.3.1	Analysis of Large-Scale DC Resistivity Data.....	90
3.3.2	Large-Scale Experiment Conclusions.....	94
CHAPTER 4	AC MODELLING	95
4.1	Lab-Scale (Pool) AC Modelling.....	95
4.1.1	High Frequency to DC Amplitude Ratios and Phase Difference	95
4.1.2	Primary Field Amplitudes and Phase.....	97
4.1.3	Secondary Fields Amplitudes and Phase	98
4.1.4	Total Fields Amplitudes and Phase.....	100
4.1.5	Lab-Scale (Pool) Conclusions.....	102
4.2	Mid-Scale (Kafadar Commons) AC Modelling.....	103
4.2.1	High Frequency to DC Amplitude Ratios and Phase Difference	103

4.2.2	Mid-Scale (Kafadar Commons) Conclusions	105
4.3	Large-Scale AC Modelling	106
4.3.1	High Frequency to DC Amplitude Ratios and Phase Difference	106
4.3.2	Large-Scale Conclusions	108
CHAPTER 5 CONCLUSIONS		109
5.1	Summary of Work.....	109
5.2	Conclusions and Speculations.....	109
5.3	Future Work	112
REFERENCES CITED.....		114

LIST OF FIGURES

Figure 1.1	3D CSEM survey geometry over complex seafloor pipeline system (Price et al., 2010).	1
Figure 1.2	Diagram of casing stages extending through the Earth (http://www.drillingformulas.com/basic-understanding-of-oil-well-casing-and-tubing/ accessed 4/25/19).	2
Figure 1.3	Traditional steel production casings used in the petroleum industry. Image used from (https://www.collidril.it/our-production/ accessed 4/25/19).	3
Figure 1.4	Diagram of typical marine CSEM survey utilizing towed dipole transmitter and nodal dipole receivers. (Constable, 2010).	4
Figure 2.1	Schematic diagram showing the geometry of the theoretical survey being using to derive the analytic expressions for primary and secondary electric fields as well as the interaction matrix within this chapter. Tx and Rx correspond to our transmitter and receiver locations respectively, x_{Tx} and x_{Rx} are the lateral distances from the transmitter or receiver to the center of the survey line, r_{Tx} and r_{Rx} are the distances from the transmitter or receiver to the center of the casing segment being tested, Z_c is the vertical distance from the surface to the center of the subject casing segment, σ_H represents the electrical conductivity of the host body, a is the outer casing radius, b is the casing's inner radius and σ_C is the electrical conductivity of the casing itself. E_{tx} is the electric field observed at the casing center, E_p is the direct electric field observed at Rx from Tx, and E_s is the electric field produced from the energized casing observed at Rx.	9
Figure 2.2	Percent difference plots between the ratio of secondary to primary electric fields calculated using the derived analytic expressions and a fully converged MoM approach at multiple different scales.	14
Figure 2.3	Method of Moments calculated E_s/E_p values plotted against number of segments (N) point to where secondary field calculations converge.	15
Figure 2.4	Secondary to primary electric field ratio plot in the presence of a 0.0164 m outer radius, 0.0131 inner radius, 0.3048 m long steel casing which allows me to observe where I see the strongest secondary field response. This leads to choosing transmitter and receiver locations for the following studies which best represent a true secondary response.	16
Figure 2.5	One segment analytic secondary to primary electric field ratio variations with increasing total volume of metal produced by an increasing wall thickness at four different given casing conductivities.	17

Figure 2.6	One segment analytic secondary to primary electric field ratio variations produced by a steadily increasing casing length. The outer and inner radius are kept constant at 0.0381 m and 0.03429 m respectively.	18
Figure 2.7	Variations in ratios of one segment analytic secondary to primary electric fields produced from a steadily increasing total casing width. Both length and wall thickness are held constant. Outer and inner radius are increased together from 0.0164 m outer radius to 0.1905 m.	19
Figure 2.8	One segment analytic secondary to primary electric field variations with an increasing host conductivity at 4 different casing conductivities. Here the X-axis is ρ_H/ρ_C meaning a decrease in host conductivity is an increase along the axis. Spatial casing properties are held constant at a length of 0.3048 m and outer and inner radius of 0.0381 m and 0.03429 m respectively. Background conductivities of 0.02, 0.025, 0.0333, 0.05, 0.0666, 0.1, and 0.2 S/m were analyzed.	20
Figure 2.9	Fully converged MoM secondary to primary electric field ratio variations with increasing cross-sectional area produced by an increasing wall thickness at four different given casing conductivities.	22
Figure 2.10	Fully converged MoM secondary to primary electric field ratio variations produced from a steadily increasing casing length. Both outer and inner radius are held constant at 0.0381 m and 0.03429 m respectively.	23
Figure 2.11	Secondary to primary electric field ratio variations produced from a steadily increasing casing length at both analytic and fully converged MoM levels. Both outer and inner radius are held constant at 0.0381 m and 0.03429 m respectively. Length increases from 0.1524 m to 0.7759 m by increments of 0.0692 m.	24
Figure 2.12	Variations in ratios of fully converged MoM secondary to primary electric fields produced from increasing total casing width. The casing length and wall thickness are kept constant.	25
Figure 2.13	Shows variations in ratios of fully converged MoM and derived analytic secondary to primary electric fields produced from a steadily increasing total casing width. Both length and wall thickness are held constant.	26
Figure 2.14	Fully converged MoM secondary to primary electric field variations with an increasing host conductivity at four different casing conductivities. Here the X-axis is ρ_H/ρ_C meaning a decrease in host conductivity is an increase along the axis. Casing dimensions are kept constant at a length of 0.3048 m and outer and inner radius of 0.0381 m and 0.03429 m respectively. Background conductivities of 0.02, 0.025, 0.0333, 0.05, 0.0666, 0.1, and 0.2 S/m were analyzed.	27
Figure 2.15	Image of the lab-scale pool environment with dimensions.	30

Figure 2.16	Finite-element modelling domain with dimensions of pool (6 m X 3.5 m X 1.2 m).	31
Figure 2.17	Cross-section through the pool modelling domain showing mesh discretization in area surrounding electrically conductive casing and surface electrodes.	32
Figure 2.18	Finite-element modelling domain with dimensions of pseudo-half space (25 m X 25 m X 20 m).	32
Figure 2.19	Finite-element modelled data with a background resistivity of 1 Ω m shown with a homogeneous medium (a) in our pseudo-halfspace scale and (b) at the pool-scale.	33
Figure 2.20	Point-by-point percent difference between the two different modelling scales with a homogeneous model space.	34
Figure 2.21	Finite-element modelled data with a background resistivity of 1 Ω m shown in the presence of an electrically conductive rod (a) in our pseudo-halfspace scale and (b) at the pool-scale.	35
Figure 2.22	Point-by-point percent difference plot between the two different modelling scales in the presence of an electrically conductive rod.	36
Figure 3.1	Photograph of the lab-scale pool experiment. A 2-inch-thick PVC pipe is suspended between two large pieces of lumber by rope allowing the PVC pipe to be lowered down to the water. Nineteen galvanized steel electrodes are driven through the pipe at 0.10 m intervals for a total array length of 1.8 m. The electrodes are attached to insulated 12 AWG wire running out of the pool and connected via banana plugs to the AGI USA SuperSting R8 DC resistivity instrument.	37
Figure 3.2	Apparent resistivity pseudosection taken within the lab-scale pool environment in a perfect homogeneous case.	38
Figure 3.3	Apparent resistivity pseudosection showing experimental data versus MoM model over the reference casing composed of galvanized steel and of length 0.3048 m, outer radius 0.0164 m and inner radius 0.0131 m. This casing, of intermediate dimensional properties, will be used in many of the following sections of chapter three to compare variations in properties such as length, width, wall thickness and material composition that are either more or less extreme than our reference.	40
Figure 3.4	Point-by-point percent difference between the MoM model and the experimental data. There is a maximum of ~10% difference near the top center of the pseudosection. The larger misfit with depth correlates to the resistive edge effects produced from the bottom of the pool.	41

Figure 3.5 Isolated secondary response of the reference casing with both experimental and MoM background removed. 42

Figure 3.6 MoM modelled reference casing with a horizontal resistive boundary placed at 0.8 m depth. 43

Figure 3.7 Schematic diagram of current flow in the pool environment (a) and in MoM model with lower resistive layer (b). 43

Figure 3.8 Experimental and MoM model apparent resistivity pseudosections of the narrowest casing having an outer radius of 0.01305 m and inner radius of 0.00785 m with equal length to that of our reference casing. 44

Figure 3.9 Percent difference between the MoM model and experimental data gathered over the narrow casing. There is a slightly higher discrepancy between experimental and MoM model data in this case than observed in figure 3.4.. 45

Figure 3.10 Experimental and MoM model apparent resistivity pseudosections of the widest casing having an outer radius of 0.0295 m and inner radius of 0.0264 m with equal length to that of our reference casing. I see a wider secondary response than that observed in the narrow or reference case. Maximum drops in apparent resistivity are only slightly larger but the total area displaying this maximum is greater than in the narrow or references scenario. 46

Figure 3.11 Point-by-point percent difference plot between the MoM model and experimental data gathered over the widest casing. There is a maximum percent difference near 15% within the top center region of the plot which fades into a smaller discrepancy along the remaining secondary response nearer to 10%. 47

Figure 3.12 Schematic diagram of a dipole-dipole resistivity array. A and B represent current electrodes and M and N represent voltage electrodes. 48

Figure 3.13 Schematic diagram illustrating the simple process used for studying the asymmetry pant-leg effect occurring at the lab-scale. A and B again represent our current electrodes, and M and N are our voltage electrodes. There is a secondary response when the current electrodes are placed near the electrically conductive casing and the voltage electrodes are at a further distance, but in the reverse scenario we often observe just the background resistivity. 49

Figure 3.14 Experimental and MoM model apparent resistivity pseudosections of the shortest casing displaying a length of 0.254 m with outer and inner radii near equal to that of the reference casing. Unlike in the presence of the narrow casing we see a secondary response as wide as that of the reference, however the center of the response extends to a shallower data level and drops in apparent resistivity are slightly lower than that observed of the control. 51

Figure 3.15 Point-by-point percent difference plot between our MoM model and experimental data gathered over a 0.254 m casing. There is a good fit between MoM model and experimental data with just below 10% discrepancy near the top center of the plot. 52

Figure 3.16 Experimental and MoM model apparent resistivity pseudosections of the longest casing displaying a length of 0.6096 m with outer and inner radii near equal to that of the reference casing. Along with a slightly deeper center of the secondary response, in the experimental data reaching so deep it connects with the resistive edge effects, we also see a slightly higher drop in apparent resistivity than that seen from our reference casing. A trend we are viewing with the extremes of these dimensional variables. 53

Figure 3.17 Point-by-point percent difference between the MoM model and experimental data gathered over the longest casing. The largest discrepancy of ~15% lies along the left leg of the secondary response due to the asymmetry artifact. 54

Figure 3.18 Experimental apparent resistivity pseudosections comparing responses from solid and hollow 0.6096 m length aluminum casings with equal outer radii. There is little difference between the two pseudosections with this view. 55

Figure 3.19 Experimental apparent resistivity pseudosections comparing secondary responses from a solid and hollow 0.6096 m length aluminum casing with equal outer radii. Here I view apparent resistivity pseudosections with the primary fields backed out showing only the secondary response. It is seen that a larger drop in apparent resistivity is present in the case of the solid casing. 56

Figure 3.20 MoM model comparison between the solid and hollow aluminum casings. There is a similar trend of a stronger response being produced from the solid casing. 57

Figure 3.21 MoM apparent resistivity pseudosections comparing secondary responses from a solid and hollow 0.6096 m length aluminum casing with equal outer radii. Here I view apparent resistivity pseudosections with the primary fields backed out showing only the secondary response. It is seen that a larger drop in apparent resistivity is present in the case of the solid casing. .. 58

Figure 3.22 Percent difference plot displaying discrepancies between MoM models and experimental data. Both display expected high discrepancies on the left-hand side due to the asymmetry artifact. The right-hand side of both plots display a misfit of ~25%. 58

Figure 3.23 Experimental and MoM model apparent resistivity pseudosections of the brass casing displaying a length and outer radius equal to that of the control casing and a slightly thinner wall. I find that the more electrically conductive casing material creates a significantly stronger drop in apparent resistivity within the secondary response. 59

Figure 3.24 Experimental and MoM modelled apparent resistivity pseudosections showing isolated secondary responses from the brass casing studied. It is seen there is a slightly larger drop in apparent resistivity, ~2-3 Ωm more, than observed from the reference casing made of steel. 60

Figure 3.25 A point-by-point percent difference showing discrepancies between the MoM model and experimental data of the brass casing. On the right-hand side of the plot less affected by the asymmetry artifact we see maximums of ~10% misfit. 61

Figure 3.26 Schematic diagram showing orientations of the horizontal and tilted casings. Both cases make use of our control casing of length 0.3048 m, outer radius 0.0164 m and inner radius 0.0131 m. 62

Figure 3.27 Experimental and MoM model apparent resistivity pseudosections of the control casing in a horizontal orientation. This positioning leads to a larger drop in apparent resistivity along the legs of the secondary response and a zone of high apparent resistivity at a slightly lower data level due to the low current density in this zone. 63

Figure 3.28 Point-by-point percent difference showing discrepancies between the MoM model and experimental data of the control casing in a horizontal orientation. In the zones of the plot that contain the drop in apparent resistivity there is a 10-15% drop in apparent resistivity. In the low-current-density zone, there is a slightly higher discrepancy reaching 30% difference. This is due to the sensitivity of the survey to slight variations along the y-axis regarding how in-line the casing is with the above electrodes. 64

Figure 3.29 Experimental and MoM model apparent resistivity pseudosections of the control casing in a tilted orientation. Like the horizontal orientation, a tilted casing positioning leads to a larger drop in apparent resistivity along the leg of the secondary response and a high apparent resistivity zone beneath this leg due to the low current density in this zone. 65

Figure 3.30 A point-by-point percent difference plot showing discrepancies between the MoM model and experimental data of the control casing in a tilted orientation. Again, there are large similarities between the discrepancies in the tilted and horizontal case. With the highest percent differences occurring in the low current density area where we see values approaching 20% difference. The slightly larger misfit in the tilted orientation as compared to strictly vertical casings is again due to the sensitivity of the survey to slight movement of the casing while collecting experimental data..... 66

Figure 3.31 Experimental and MoM model apparent resistivity pseudosections of two vertical reference casings positioned beneath electrodes seven and thirteen. There is a combination of the two secondary responses at data level seven creating a third drop in apparent resistivity comparable to the maximum drop seen near the surface beneath each casing. 67

Figure 3.32 Isolated secondary response of dual vertical reference casings suspended beneath electrode seven and thirteen. 68

Figure 3.33 A point-by-point percent difference plot showing discrepancies between the MoM model and experimental data for our dual vertical casing scenario with the two suspended near one another. We see the largest percent differences (~35-40%) where the two secondary responses constructively interfere. 69

Figure 3.34 Experimental and MoM model apparent resistivity pseudosections of two vertical control casings positioned beneath electrodes four and sixteen. We again see constructive interference between the two secondary responses; however, in this case the interference occurs at a low data level, such that it is obscured by the resistive edge effects of the pool bottom. 70

Figure 3.35 A point-by-point percent difference plot showing discrepancies between the MoM model and experimental data for the dual vertical casing scenario with the two suspended further from one another. 71

Figure 3.36 Schematic diagram of the multi-casing horizontal and vertical orientation survey. 71

Figure 3.37 Experimental and MoM model apparent resistivity pseudosections of one vertical control casing beneath electrode thirteen and a horizontal control casing with its end beneath electrode seven and its length extending towards X = -0.9 m. 72

Figure 3.38 Isolated secondary response produced from adjacent horizontal and vertical reference casings. 73

Figure 3.39	A point-by-point percent difference plot showing discrepancies between the MoM model and experimental data for our vertical and horizontal dual casing survey.	74
Figure 3.40	Schematic diagram showing the positions of the two casings for the vertical and tilted casing survey.	74
Figure 3.41	Experimental and MoM model apparent resistivity pseudosections of one vertical control casing beneath electrode thirteen and a tilted control casing with its end beneath electrode seven and its length extending diagonally in the negative X-direction.	75
Figure 3.42	A point-by-point percent difference plot showing discrepancies between the MoM model and experimental data for the vertical and tilted dual casing survey.	76
Figure 3.43	Plan view map of the Kafadar Commons buried geophysical laboratory on the Colorado School of Mines Campus (Krahenbuhl et al., 2018).	80
Figure 3.44	Plan view map of Kafadar Commons highlighting the location of the steel-cased vertical borehole, and its associated DC resistivity surveys. (Google Maps, 2019).	81
Figure 3.45	Apparent resistivity pseudosection of the control line parallel to and offset by 3 m from the vertical borehole survey. Gathered using AGI USA SuperSting R8 DC resistivity instrument, and 20 stainless-steel electrodes spaced at 1 m.	82
Figure 3.46	Inversion of the control survey. Created using 19 iterations within the DC resistivity software “RES2DINV” to an RMS value of 0.27%. A resistivity-depth profile derived from this section is used as input for the MoM modelling code.	82
Figure 3.47	Apparent resistivity pseudosections produced from the MoM model and associated experimental data gathered over the steel-cased vertical borehole buried in Kafadar Commons.	83
Figure 3.48	Point-by-point percent difference plot produced from the misfit between the MoM model and experimental data of the vertical borehole survey in Kafadar Commons.	84
Figure 3.49	Schematic diagram illustrating the out-of-line offset used in the MoM modelling of the vertical borehole in Kafadar Commons.	85
Figure 3.50	Plan view map showing the location of the buried horizontal aluminum pipe in Kafadar Commons and its associated DC resistivity survey.	86

Figure 3.51	Apparent resistivity pseudosections produced from the MoM model and associated experimental data gathered over the 6 m long horizontal aluminum pipe buried in Kafadar Commons.	87
Figure 3.52	Point-by-point percent difference plot produced from the misfit between the MoM model and experimental data of the horizontal aluminum pipe survey on Kafadar Commons.	88
Figure 3.53	Map showing our large-scale field site in eastern Colorado in relation to the CSM campus. A pop-out map shows the location of three different DC resistivity surveys conducted.	90
Figure 3.54	Apparent resistivity pseudosection of an offset and parallel control survey conducted to better understand the background conductivity structure of the large-scale field site.	91
Figure 3.55	Apparent resistivity pseudosections produced by MoM and experimental data of line 1 from figure 3.53.	92
Figure 3.56	Point-by-point percent difference plot produced between the MoM solution and the experimental field data. Maximum discrepancies of ~50% are observed within the zone of secondary response.	93
Figure 3.57	Apparent resistivity pseudosection section data collected along line 3 in figure 3.53 over our abandoned steel-cased well.	94
Figure 4.1	Lab-scale $E_{tot}(\text{High Frequency})/E_{tot}(\text{DC})$ amplitudes at full range of tested frequencies.	95
Figure 4.2	Lab-scale phase difference between $E_{tot}(\text{High Frequency})$ and $E_{tot}(\text{DC})$ at full range of tested frequencies.	96
Figure 4.3	Lab-scale $\log(10)$ amplitudes of primary field at full range of tested frequencies.	97
Figure 4.4	Lab-scale phase values in radians of primary field at full range of tested frequencies.	98
Figure 4.5	Lab-scale $\log(10)$ amplitudes of secondary field at full range of tested frequencies.	99
Figure 4.6	Lab-scale phase values in radians of secondary field at full range of tested frequencies.	100
Figure 4.7	Lab-scale $\log(10)$ amplitudes of total field at full range of tested frequencies.	101
Figure 4.8	Lab-scale phase values in radians of total field at full range of tested frequencies.	102

Figure 4.9 Mid-scale $E_{tot}(\text{High Frequency})$ to $E_{tot}(\text{Low Frequency})$ amplitude ratios at full range of tested frequencies. 104

Figure 4.10 Mid-scale phase difference values between $E_{tot}(\text{High Frequency})$ and $E_{tot}(\text{Low Frequency})$ at full range of tested frequencies. 105

Figure 4.11 Large-scale $E_{tot}(\text{High Frequency})$ to $E_{tot}(\text{DC})$ amplitude ratios at full range of tested frequencies. 106

Figure 4.12 Large-scale phase difference between $E_{tot}(\text{High Frequency})$ and $E_{tot}(\text{DC})$ for full range of tested frequencies. 107

LIST OF TABLES

Table 2.1	Table showing RMS error fit between numeric MoM approach and analytic expressions derived within this chapter for variations in secondary electric fields from a given change in electrically conductive casing property.	29
Table 3.1	The results from tests to study the asymmetry artifact show vastly different observed apparent resistivities depending on the placement of our current electrodes in relation to the electrically conductive casing being surveyed.	50
Table 3.2	Calculated RMS error values between our MoM models and experimental data for each lab scale survey discussed. Scenarios with “Es” tag are isolated secondary responses.	79
Table 5.1	Table of RMS error values for each experiment at all three scales.	111

ACKNOWLEDGEMENTS

This work is carried out in cooperation between the Electromagnetic resource Exploration Group (EMREX) at the Colorado School of Mines and Shell. I thank Liam Ó Súilleabháin for helpful discussions. This work could not have been completed with many people who have had a hand in either it or in supporting me throughout this process. I would like to thank my wife for keeping my spirits up even when she may have been down from her own graduate studies. For keeping us fed, and for being there to encourage a break when it was most needed. I thank my family for their encouragement to take this adventure on in the first place as I left my home in the Carolinas. Thank you to my academic advisor, Dr. Andrei Swidinsky, for constant encouragement, fresh ideas, and for the opportunity to undertake this project in the first place. Thanks also go out to my committee members Dr. Rita Streich and Dr. Brandon Dugan. Gurban Orujov and the many other graduate students who were always there for a conversation technical or otherwise.

CHAPTER 1

INTRODUCTION

1.1: Background

There are many geophysical methods for determining structure and composition of the subsurface. From the development of 3D seismic reflection surveys being commonly used in the mid-1980s (Dragoset, 2005) it has been the primary method in hydrocarbon exploration due to its efficiency in understanding subsurface structure. Controlled-source electromagnetic (CSEM) surveys provide another addition to the exploration work-flow by giving us an understanding of the fluids in the pore-space of the rocks themselves (Ziolkowski and Wright, 2012). Conducted early in the exploration process CSEM clarifies possible ambiguities present in seismic data through highlighting differences between electrical conductivities of subsurface host material and oil-bearing reservoirs (Ellingsrud et al., 2002, Constable and Srnka, 2007, Ziolkowski and Wright, 2012). Ideally, it could also be used later within a field's production life for appraisal purposes. However, due to the nature of the CSEM method electrically conductive infrastructure associated with production, as seen in figure 1.1, may introduce fatal artifacts to CSEM datasets (Price et al., 2010).

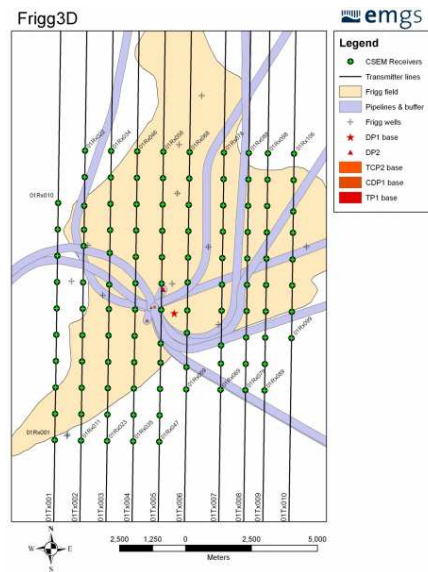


Figure 1.1: 3D CSEM survey geometry over complex seafloor pipeline system (Price et al., 2010).

Due to the cost-efficiency, high strength and high safety nature of steel it serves as the primary building material used for most well casings and pipelines (Boskovic, 2014). After the drilling of a petroleum well it is cased in multiple stages to prevent cave in of a well, permit steady flow of hydrocarbons and protect ground water (Rahman, 1995).

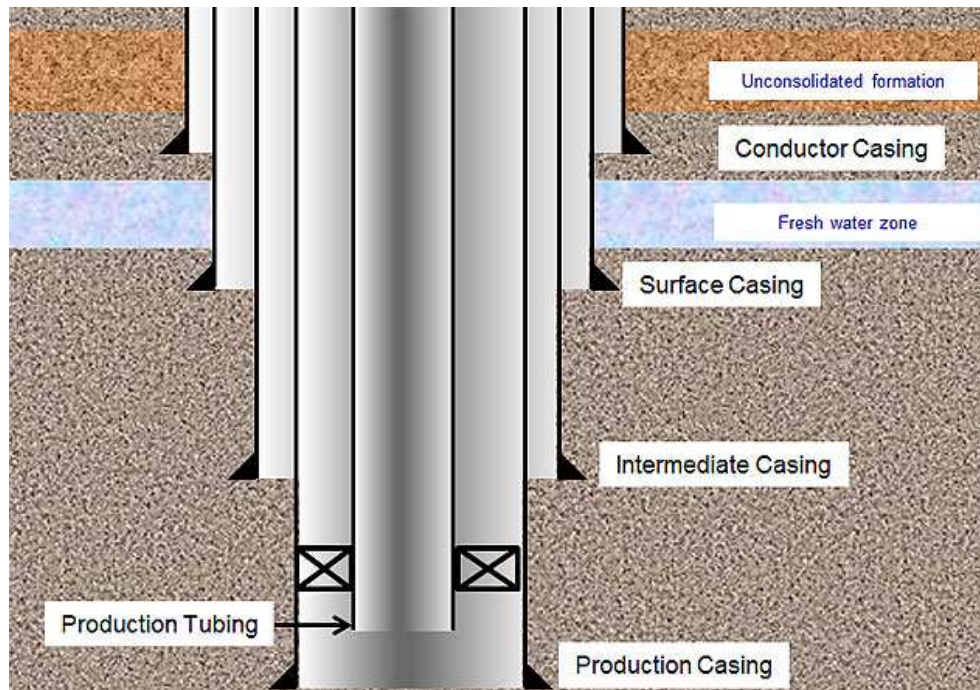


Figure 1.2: Diagram of casing stages extending through the Earth (<http://www.drillingformulas.com/basic-understanding-of-oil-well-casing-and-tubing/> accessed 4/25/19).

Although it has many benefits from a structural point of view, the electrical conductivity of steel is about six orders of magnitude larger than that of the seafloor. Non-conductive materials, such as polyvinyl chloride (PVC) or fiberglass are chosen as the material for a water well casing in conditions such as very alkaline or acidic waters, or high salinities, which would prove corrosive to steel infrastructure (AWGT, 2003). Although these materials mitigate corrosive effects, they pose many issues of their own; for example, the lower strength of PVC relative to steel necessitates careful installation and insulation to avoid cracking or even well blowouts caused by the high pressures and temperatures experienced at depth in the case of oil and gas exploration

(Harden, 2013). These extra precautions lead to high costs causing most industry companies to default to traditional steel casings as shown in figure 1.3.



Figure 1.3: Traditional steel production casings used in the petroleum industry. Image used from (<https://www.collidrill.it/our-production/> accessed 4/25/19)

1.2: Marine CSEM Background

Marine CSEM surveys have developed from the marine MT method which is CSEM's passive counterpart (Ziolkowski and Wright, 2012). Both measure electric and magnetic fields using standalone receivers; however, the CSEM method makes use of a man-made source most commonly transmitting a square wave of a given frequency. CSEM surveys rely on Faraday's law of EM induction to induce eddy currents in the seafloor through a time varying EM field. Measurements taken with either nodal or towed receivers in the sea water of both magnetic and electric fields hold information regarding the conductivity structure of the seafloor (Edwards et al., 2010). CSEM can detect variations between pore space saturated with electrically conductive salt water or much more resistive hydrocarbons providing input for volumetric and risk analysis (Baltar and Roth, 2012, Ziolkowski and Wright, 2012). CSEM surveys as they are known today were developed and conducted by the Scripps Institution of Oceanography in the 1970s, using MT receivers (Cox, 1981, Filloux et al., 1973, Ziolkowski and Wright, 2012). The

current practice of a towed transmitter ~50 m from the seafloor, as seen in figure 1.4, was developed by Sinha et al. (1990) and transmits electric currents produced by a mostly horizontal bipole between two current electrodes.

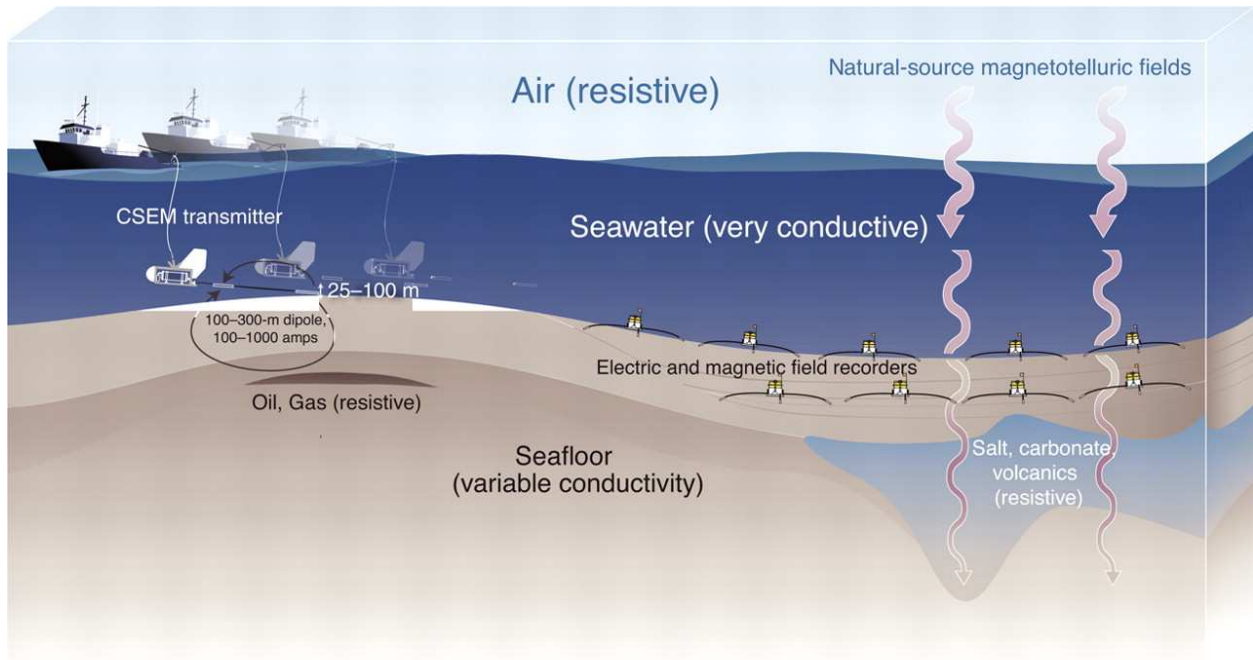


Figure 1.4: Diagram of typical marine CSEM survey utilizing towed dipole transmitter and nodal dipole receivers. (Constable, 2010).

Typical CSEM frequencies range from less than 0.1 to 10 Hz and with latest-generation equipment, penetration depths of up to 4000 m may be reached, depending on subsurface conductivity and water depth (Mittet and Morten, 2012, Ziolkowski and Wright, 2012, Guo 2016). With the advent of deep-water exploration, the petroleum industry took notice of the CSEM method in the 1990s (Srka, 1987, Constable and Srka, 2007). Deepwater exploration allowed for the suppression of the air-wave which limited marine EM experiments for petroleum industry purposes through most of the 20th century (Constable and Weiss, 2006, Constable and Srka, 2007). In the late 1990s, Statoil conducted research using an interesting experimental setup making use of a water bed. They found that in conditions of significant water depth and target burial depth, a resistive oil reservoir showed “controlled source amplitudes that are a factor of 2 to 10 times different than models without the oil layer” (Constable and Srka, 2007).

Modern case studies making use of significant CSEM anomalies in addition to other datasets to derisk prospects see an average of 70% success rate as opposed to the ~35% success rate in those without resistive CSEM anomalies (Hesthammer, 2010).

1.3: Marine CSEM in the Presence of Conductive Infrastructure

Within the last decade attempts have been made to use marine CSEM as an appraisal tool for late-life oil fields (Orange et al., 2009, Lien and Mannseth, 2008). Potential has been found in the method itself for identifying a depleting reservoir; however, electrically conductive infrastructure can produce significant artifacts in the data obscuring interpretations (Orange et al., 2009, Price et al., 2010). These artifacts, often observed as conductive anomalies depend on casing and survey orientation, as will be observed in this thesis. In some cases, data affected by the presence of well casings and pipelines has had to be ignored entirely (Price et al., 2010, Park et al., 2013, Morten et al., 2012). In combination with time-lapse seismic (Landro et al., 2003, Vasco et al., 2008), CSEM has shown promising results for the monitoring of lateral extents of hydrocarbon reservoirs as they deplete (Orange et al., 2009). To best utilize CSEM for this application, however, a precise understanding of the impacts of electrically conductive infrastructure on measured CSEM data and a method of processing affected are required.

1.4: Thesis Outline

The project began with the development of a numeric modelling code based on Method of Moments (MoM) theory (Kohnke, 2017, Kohnke et al., 2018). This code calculates the secondary electric fields produced by electrically conductive well casings indirectly energized by electromagnetic surveys. This is achieved by discretizing a given casing into many finite elements. First, the interaction matrix is found, following this the current on each casing element is evaluated, and finally these currents are used to obtain the secondary electric field at the receiver location. This MoM approach is still being developed (Orujov et al., 2019) and will be used for modelling purposes throughout this thesis.

Although characterizing the effects of steel infrastructure on CSEM data is of ultimate interest to industry, much can be learned by studying the zero-frequency direct-current (DC) resistivity counterpart of the finite-frequency alternating-current (AC) problem. I will focus on the zero frequency, or DC, electrical resistivity method used to conduct experiments at the

laboratory-scale, mid-scale, and large-scale. DC experiments will be interpreted in terms of understanding the effect on DC resistivity data introduced by electrically conductive casings. I will discuss a theoretical study carried out in chapter 2 to aid in the design of lab-scale experiments, and better understand observed secondary responses at all experimental scales. I will derive analytic expressions for electric fields which will provide a method of quickly calculating variations in secondary response due to changes in casing properties. This analytic approach will be compared against a fully converged MoM solution to cross-check my derived expressions for legitimacy.

Chapter 3 will focus on the introduction and analysis of experimental DC data gathered at all three scales. I begin with the lab-scale experiment I have developed on the CSM campus. The lab's versatile setup and homogeneous background has allowed me to analyze many different casings of a wide variety of lengths, widths, materials and orientations surveyed within the experiment. I have established how these properties affect both magnitude and spatial distribution of the secondary response. Throughout this process I will also analyze each survey's associated MoM model, assess its fit to the real data and discuss possible sources of misfit. I will also discuss mid-scale experiments conducted on the CSM Campus. During the recent construction of the CoorsTek Center for Applied Science and Engineering an adjacent grassy field known as Kafadar Commons was transformed into an underground laboratory with many buried objects making excellent targets for AC and DC surveys. I will discuss two surveys conducted over a 15 m vertical steel-cased borehole, and an inline survey over a 6 m horizontal aluminum pipe. The mid-scale surveys present some level of uncertainty with the dimensional properties of the targets that will be discussed through study of the MoM models for this case and their respective discrepancies from the field data. Finally, I will analyze a large-scale field dataset acquired in November 2017 over an abandoned steel-cased oil and gas well of 130 m vertical length. The well and its dimensions were found using the Colorado Oil and Gas Commission's (COGCC) database. A DC resistivity survey was conducted directly over the casing, and a second survey was conducted along an offset parallel line to act as a controlled background for the field site. As in the lab and mid-scale scenarios, I will model these field datasets using the MoM approach and discuss possible sources of misfit.

Finally, I will focus our efforts towards the future in chapter 4. Here I will re-examine all three scales discussed in chapter 3, yet now I will use our MoM modelling code to prepare for future AC field work. This will be accomplished by testing a wide range of possible transmitting frequencies to pinpoint the frequency range at which we start seeing AC behavior. I will attempt to observe a change from the typical DC response which is seen at lower frequencies to a host of amplitude fluctuations and large phase changes at higher frequencies.

CHAPTER 2

THEORY AND FINITE-ELEMENT MODELLING FOR EXPERIMENTAL STUDIES

2.1: An Analytic Expression for Electric Fields in a Wholespace

To better understand the effect of scaling on my experiment in both nature and magnitude; an analytic expression may be derived for both the interaction matrix as well as the primary and secondary electric fields based on the theory of Ward and Hohmann (1988). Though the expressions discussed in this section for electric fields of my experiment do not agree perfectly with fully converged values from the numerical Method of Moments (MoM) solution it acts still as a simple and fast method for understanding the magnitude of the variations in casing response, further referred to as the secondary response, produced from changes in the experimental environment of the pool. Below I will discuss the derivation of these expressions as well as some mathematical observations regarding the implications of changing variables in electrically conductive casing properties.

2.1.1: Derivation of Analytic Expression for our Interaction Matrix

An analytic expression for the interaction matrix, or A matrix, must first be developed within this chapter so that further derivations for electric fields may be completed. The A matrix describes the interactions between individual discretized elements of the casing while excited from the perspective of one energized element acting as a source interacting with another element acting as a test point. A simple analytic expression for the A matrix in the presence of a vertical electrically conductive casing in a whole space can be derived by starting from equation (8) in Tang et al. (2015). For this derivation, beginning with equation (2.1), I have removed the second exponential term from Tang et al. (2015) representative of the reflective component from the air-Earth interface. For the following wholespace expressions this term was unnecessary. I have also divided both terms by area (dA) as was done in equation (7) from Kohnke et al. (2018) as I am working with current itself rather than the current density used in Tang et al. (2015).

$$A_{ii} = \frac{\rho_2}{dA} - \frac{\rho_1}{4\pi dA} \int_{z_c-d_z/2}^{z_c+d_z/2} \int_0^{2\pi} \int_b^a \int_0^\infty e^{-s|z-z'|} \frac{\lambda^3}{s} J_0(\lambda r) r d\lambda dr d\varphi dz. \quad (2.1)$$

Figure 2.1 shows a visual representation of the physical variables with equation (2.1) and later derivations.

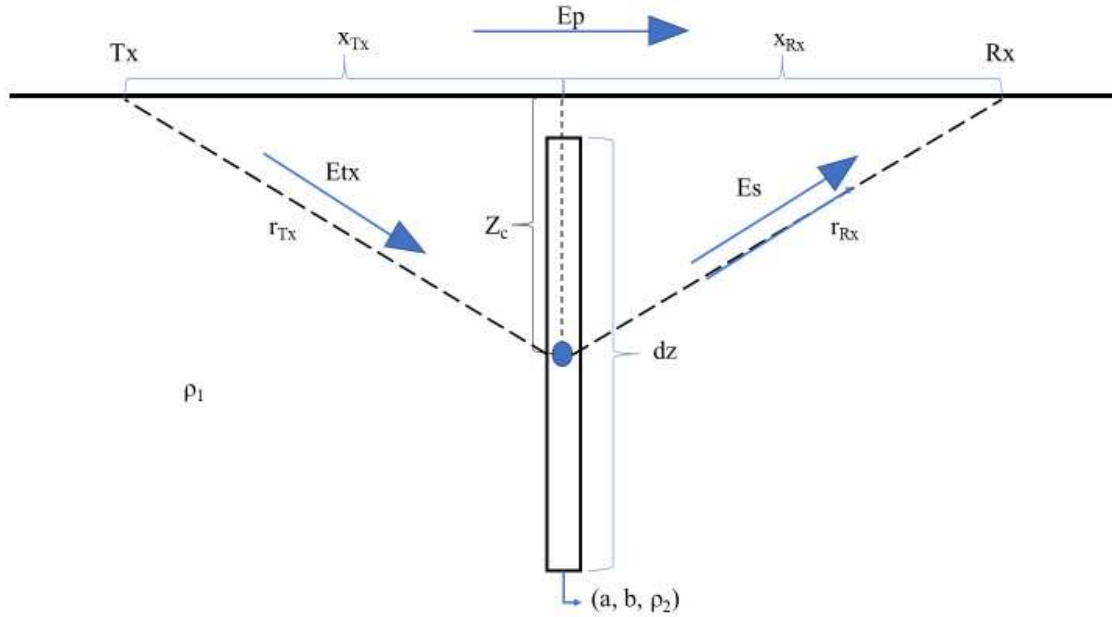


Figure 2.1: Schematic diagram showing the geometry of the theoretical survey being using to derive the analytic expressions for primary and secondary electric fields as well as the interaction matrix within this chapter. Tx and Rx correspond to our transmitter and receiver locations respectively, x_{Tx} and x_{Rx} are the lateral distances from the transmitter or receiver to the center of the survey line, r_{Tx} and r_{Rx} are the distances from the transmitter or receiver to the center of the casing segment being tested, Z_c is the vertical distance from the surface to the center of the subject casing segment, σ_H represents the electrical conductivity of the host body, a is the outer casing radius, b is the casing's inner radius and σ_C is the electrical conductivity of the casing itself. E_{Tx} is the electric field observed at the casing center, E_p is the direct electric field observed at Rx from Tx, and E_s is the electric field produced from the energized casing observed at Rx.

Here $s = \sqrt{\lambda^2 + \frac{i\omega\mu}{\rho_H}}$ leading to $s = \lambda$ within the DC regime with an angular frequency, ω , equal to zero. Now integrating with respect to z and φ I come to:

$$A_{ii} = \frac{\rho_2}{dA} - \frac{\rho_1}{4\pi dA} 2\pi \int_b^a \int_0^\infty \left(-\frac{1}{s}\right) \left(2e^{-\frac{sdz}{2}} - 2\right) \frac{\lambda^3}{s} J_0(\lambda r) r d\lambda dr, \quad (2.2)$$

And then substituting λ for s gives:

$$A_{ii} = \frac{\rho_2}{dA} + \frac{\rho_1}{dA} \int_b^a \int_0^\infty \lambda (e^{-\frac{\lambda dz}{2}} - 1) J_0(\lambda r) r d\lambda dr, \quad (2.3)$$

Which after distributing simplifies to:

$$A_{ii} = \frac{\rho_2}{dA} + \frac{\rho_1}{dA} \int_b^a \int_0^\infty \lambda r e^{-\frac{\lambda dz}{2}} J_0(\lambda r) d\lambda dr - \frac{\rho_1}{dA} \int_b^a \int_0^\infty \lambda r J_0(\lambda r) d\lambda dr. \quad (2.4)$$

Now I integrate the first term which I will call C with respect to λ :

$$C = \int_b^a \int_0^\infty \lambda r e^{-\frac{\lambda dz}{2}} J_0(\lambda r) d\lambda dr \quad (2.5)$$

$$C = \int_b^a \frac{r \frac{dz}{2}}{\left(\frac{dz^2}{4} + r^2\right)^{3/2}} dr. \quad (2.6)$$

Then through using equation (7) in table 8.2 from *Tables of Integral Transforms Vol. II* (Bateman, 1954) and integrating with respect to r :

$$C = \frac{dz}{\sqrt{dz^2 + 4b^2}} - \frac{dz}{\sqrt{dz^2 + 4a^2}}. \quad (2.7)$$

I then move on to the second term from the above A matrix expression which I will name D. I will switch the integration order here and begin with integrating with respect to r :

$$D = \int_0^\infty \int_b^a \lambda r J_0(\lambda r) d\lambda dr. \quad (2.8)$$

Then, from equation (9) in Tang et al 2015:

$$D = \int_0^\infty -\lambda \left[\frac{1}{\lambda} a J_1(\lambda a) - \frac{1}{\lambda} b J_1(\lambda b) \right] d\lambda \quad (2.9)$$

$$D = -\left[\int_0^\infty a J_1(\lambda a) d\lambda - \int_0^\infty b J_1(\lambda b) d\lambda \right]. \quad (2.10)$$

Now with respect to λ given a Bessel function integrated from 0 to ∞ :

$$D = - \left[a \left(\frac{1}{a} \right) - b \left(\frac{1}{b} \right) \right] = -[1 - 1] = 0 \quad (2.11)$$

Putting the A_{ii} term back together now after integration leads us to the final expression:

$$A_{ii} = \frac{\rho_2}{dA} + \frac{\rho_1}{dA} \left(\frac{dz}{\sqrt{dz^2+4b^2}} - \frac{dz}{\sqrt{dz^2+4a^2}} \right). \quad (2.12)$$

From this expression it is seen that the interaction matrix is most heavily affected by physical parameters of the casing I am studying such as its length and its cross-sectional area.

2.1.2: Derivation of Analytic Expression for Both Primary and Secondary Electric Fields

For the derivation of an analytic expression for the total electric fields within a wholespace produced from a horizontal dipole with moment of $M = \mathbf{I}dl = 1$. I begin with equation 2.40 of Ward and Hohmann (1988).

$$\mathbf{E} = \frac{\mathbf{I}dl\rho_H}{4\pi r^3} e^{-ikr} \left[\left(\frac{x^2}{r^2} \mathbf{u}_x + \frac{xy}{r^2} \mathbf{u}_y + \frac{xz}{r^2} \mathbf{u}_z \right) \right. \quad (2.13)$$

$$\left. (-k^2 r^2 + 3ikr + 3) + (k^2 r^2 - ikr - 1) \mathbf{u}_x \right].$$

Where \mathbf{I} is the current of the system, dl is the length of the current source, ρ_H is the host resistivity, r is the distance from either Tx or Rx to the receiver location, x is the full distance from Tx to Rx, and z is the vertical distance from the receiver to the transmitter. In equation (2.13) \mathbf{u}_x , \mathbf{u}_y , and \mathbf{u}_z represent the X, Y and Z components of the total electric field within the wholespace. At the DC level k ($k = \frac{i\omega\mu}{\rho_H}$), the wave number, goes to zero eliminating all terms containing k . Within this section I will first derive an analytic expression describing the electric field traveling from the transmitter to the receiver directly, or E_p . I will then derive an expression describing the field travelling from the transmitter and observed by the single segment casing to be explored. Finally, I will derive an expression to calculate the field seen at the receiver location, Rx, in figure 2.1 produced from the excited casing itself. To describe the primary electric field (\mathbf{E}_p), or the field produced from our transmitter dipole, from the above expression I take only those components relying upon \mathbf{u}_x . This leads to:

$$\mathbf{E}_p = \frac{\mathbf{I}dl\rho_H}{4\pi r^3} \left(\frac{3x^2}{r^2} - 1 \right). \quad (2.14)$$

In this case our source and receiver are at the same Z location meaning $x = r$ and therefore \mathbf{E}_p becomes:

$$\mathbf{E}_p = 2 \frac{\mathbf{I}dl\rho_H}{4\pi x^3}, \quad (2.15)$$

From which I obtain,

$$\mathbf{E}_p = \frac{\mathbf{I}dl\rho_H}{2\pi x^3}. \quad (2.16)$$

However, in this case where I am assuming a unit dipole $\mathbf{I}dl = 1$ leading to the final expression of:

$$\mathbf{E}_p = \frac{\rho_H}{2\pi x^3}. \quad (2.17)$$

From this very simple expression it is seen that the solitary factors controlling the magnitude of the electric field being produced by our horizontal transmitter dipole are the conductivity of the host body, and the distance from the transmitter location to the receiver location. If either of these are increased, then there will be a decrease in the strength of \mathbf{E}_p .

Next, I derive a similar expression describing the electric field produced from the excited well casing as it is seen by the receiver. I will call this our secondary electric field (\mathbf{E}_s). Given that the secondary field is produced from the vertical well casing acting as a vertical dipole, I will make use of only the components (2.13) relying upon \mathbf{U}_z . This will allow us to produce an expression called \mathbf{E}_{Tx} , or the electric field observed at the center of the casing produced from the transmitter at Tx, which will lead to \mathbf{E}_s . Concerning ourselves with only \mathbf{U}_z dependent components leads to:

$$\mathbf{E}_{Tx} = \frac{\mathbf{I}dl\rho_H}{4\pi r_{Tx}^3} \left(\frac{3x_{tx}z}{r_{Tx}^2} \right), \quad (2.18)$$

which becomes:

$$\mathbf{E}_{Tx} = \frac{3\mathbf{I}dl\rho_H x_{tx}z}{4\pi r_{Tx}^5}, \quad (2.19)$$

and then:

$$\mathbf{E}_{Tx} = \frac{3\mathbf{I}dl\rho_H x_{tx}z}{4\pi(x_{Tx}^2 + z^2)^{5/2}}. \quad (2.20)$$

From here I give an analogous expression for (2.20) describing the field from a source at Rx observed at the casing center. Through reciprocity this is equal to a source at the casing center

observed by a receiver at location Rx. Now, however, I have a different source current and length which I call \mathbf{I}_s and dz , respectively. develop an expression for \mathbf{E}_s by instead finding \mathbf{E}_{Tx} at the receiver location or distance x_{Rx} :

$$\mathbf{E}_s = \frac{3\mathbf{I}_s dz \rho_H x_{Rx} z}{4\pi(x_{Rx}^2 + z^2)^{5/2}}. \quad (2.21)$$

By then using $\mathbf{I}_s = Et_x/A_{11}$ from Tang et al. (2015) where A_{11} is the interaction matrix reduced to a single element. I can manipulate \mathbf{E}_s into a form that can be used analytically without prior knowledge of \mathbf{I}_s . This brings us to:

$$\mathbf{E}_s = \frac{3x_{Rx} dz \rho_H z E_{Tx}}{4\pi A_{11} (x_{Rx}^2 + z^2)^{5/2}}. \quad (2.22)$$

By then substituting the above equation for \mathbf{E}_{Tx} and simplifying I find:

$$\mathbf{E}_s = \frac{9\rho_H^2 z^2 x_{Rx} x_{Tx} dz}{16\pi^2 r_{Rx}^5 r_{Tx}^5 A_{11}}. \quad (2.23)$$

From this equation it is seen that the secondary electric field produced from the excited well casing is largely dependent upon the distance to the casing from both the transmitter position and the receiver position.

2.1.3: Analytic VS MoM Accuracy Check

With the derivation of these simple analytic equations I may now quickly calculate expected differences in both primary and secondary electric fields as they relate to changes in the conductivity of the host, the casing itself or the geometry of the casing. To check legitimacy of these expressions I take the ratio of \mathbf{E}_s to \mathbf{E}_p expressed as:

$$\frac{E_s}{E_p} = \frac{9z^2 x_{Rx} x_{Tx} x^3 dz}{8\pi \sigma_H r_{Rx}^5 r_{Tx}^5 A_{11}}, \quad (2.24)$$

and compare it to the same ratio computed from the MoM numerical method. Figure 2.2 shows percent differences between the ratio of E_s/E_p for the analytic to numeric calculations.

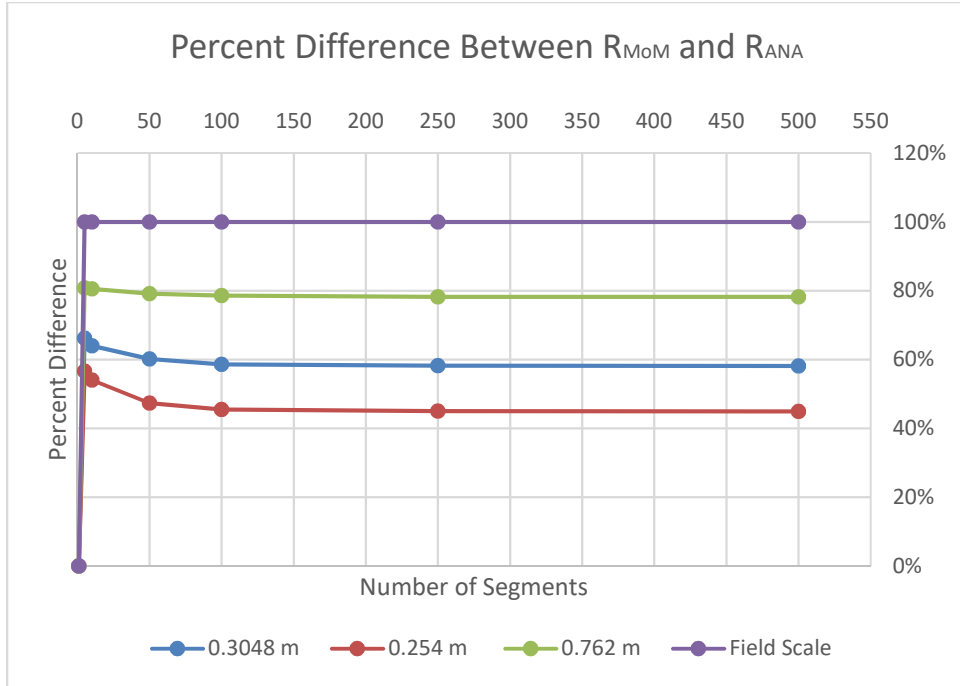


Figure 2.2: Percent difference plots between the ratio of secondary to primary electric fields calculated using the derived analytic expressions and a fully converged MoM approach at multiple different scales.

The percent differences displayed in Figure 2.2 are found by $ABS(1 - \frac{R_{ANA}}{R_{MoM}})$ at three different casing lengths to be observed at the lab scale and a fourth corresponding to the dimensions of the large-scale field data collection. I study first an electrically conductive casing with an outer radius of 0.0381 m and inner radius of 0.03429 m at a length of 0.254 m (10 in), 0.3048 m (1 ft), 0.762 m (2.5 ft) and the field scale with an outer radius of 0.105 m, an inner radius of 0.095 m and a length of 130 m. Given the difference between the analytic expressions and the numeric calculation lies in the numeric method discretizing the casing along its length into multiple segments for a more accurate calculation of currents, and consequently electric fields it follows that I would see smaller percent differences between the two methods in casings with shorter lengths. The number of segments required for convergence in each case can be seen in figure 2.3. In each case there is a spike in E_s/E_p as we move away from a single segment (equivalent to the analytic approach) and increase to a maximum of 500 segments along the X-axis. The field scale casing takes the most segments to see a fully converged solution at ~250. Due to its size more segments are required to discretize it and accurately calculate secondary field values.

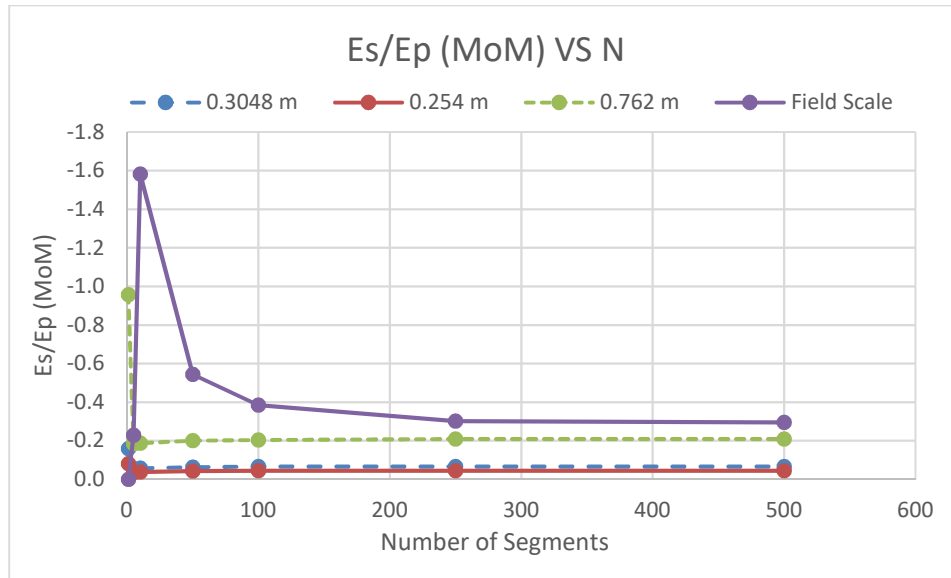


Figure 2.3: Method of Moments calculated E_s/E_p values plotted against number of segments (N) point to where secondary field calculations converge.

With fully converged numeric values I see percent differences of ~45% for the 0.254 m long casing, ~60% for the 0.3048 m long casing, ~80% for the 0.762 m long casing and about 100% difference when studying the field scale in figure 2.2. This shows that when it comes to making fast and accurate predictions of exact secondary electric field values my approximation may not be the best tool, however, as will be seen in the following sections the analytic expressions can be used to estimate the magnitude of secondary electric field variations from a given change in casing material or property. The difference observed at the field scale, however, means that the derived analytic expressions will not be useful in this largest case.

2.2: Field Variations with Changing Casing Properties: Analytic Solution

Using the analytic expressions I derived in section 2.1, I will now explore how the properties of the electrically conductive casing, such as material composition, width and length affect calculated secondary electric fields. For the purposes of conducting these tests, I choose a transmitter-receiver pair at which I study the secondary field variations. For this theoretical study I will make use of the survey geometry used within the pool in which laboratory-scale experiments were carried out (see Chapter 3). The electrode array installed in this pool consists of nineteen electrodes spaced at 0.1 m. The electrically conductive casing is centered beneath

the central electrode ($x = 0.0$ m). There are many possible pairs of electrodes which could be used for tests. To determine which of these pairs will be used, I have produced the E_s/E_p pseudosection shown in figure 2.4. This section highlights areas of interest within the simulated survey where the effects of the secondary fields are most strongly seen. The spatial distribution of the casing effects will differ depending on casing properties. To best represent the variety of casings that will be surveyed in Chapter 3 this test was conducted using our reference casing of the most intermediate properties explored.

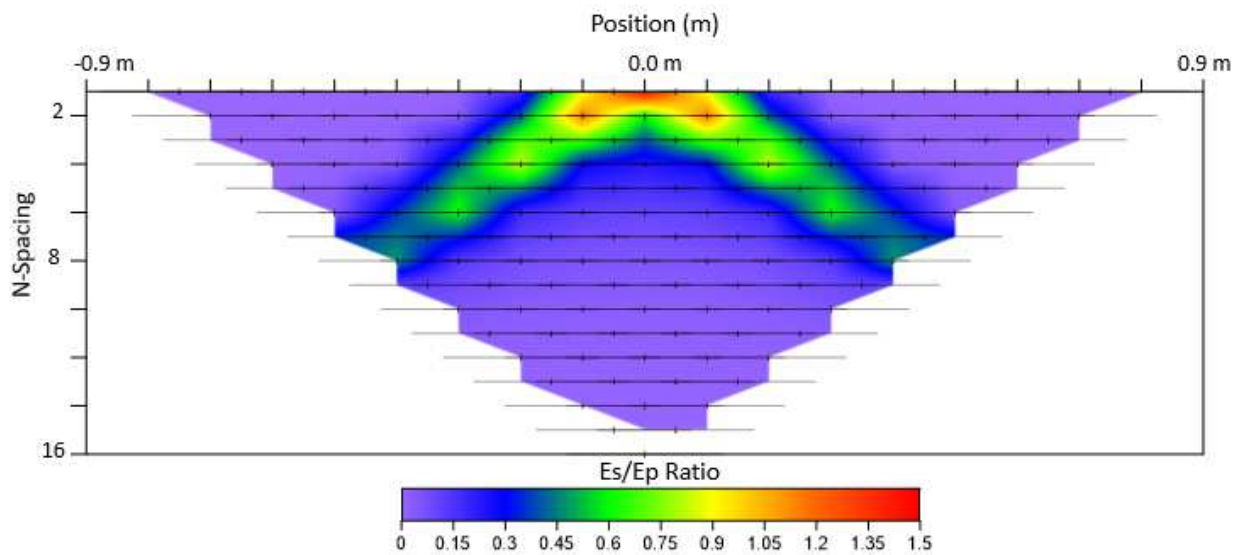


Figure 2.4: Secondary to primary electric field ratio plot in the presence of a 0.0164 m outer radius, 0.0131 inner radius, 0.3048 m long steel casing which allows me to observe where I see the strongest secondary field response. This leads to choosing transmitter and receiver locations for the following studies which best represent a true secondary response.

Electrode positions are presented as the major tick marks along the upper X-axis of the plots spaced at intervals of 0.1 m. N-Spacing along the Y-axis is representative of a scalar multiplier applied to an individual dipole length that describes the distance between the transmitter and the receiver dipole. E_s/E_p ratios are studied to gain understanding of where the secondary response produced by the casing most outweighs the primary field. Based on this method I have chosen to conduct these tests with the transmitter position as $x = -0.4$ m and the receiver at $x = 0.4$ m.

2.2.1: Analysis of Analytic Expressions for Cross-Sectional Area of the Casing

I will first study the effects of the cross-sectional area of the casing on the secondary fields. This is a question of great importance to the project as there are a wide variety of casing conductivities as well as widths and wall thicknesses in developed oil and gas fields. In this section, in the fully converged numerical analysis of section 2.3 and in the presentation of lab scale experimental data of chapter 3 I will attempt to quantify these effects. In figure 2.5 I keep a constant length and outer radius of 0.3048 m and 0.0381 m, respectively. I then decrease the inner radius from 0.0343 m to 0.0019 m by intervals of 0.0057 m.

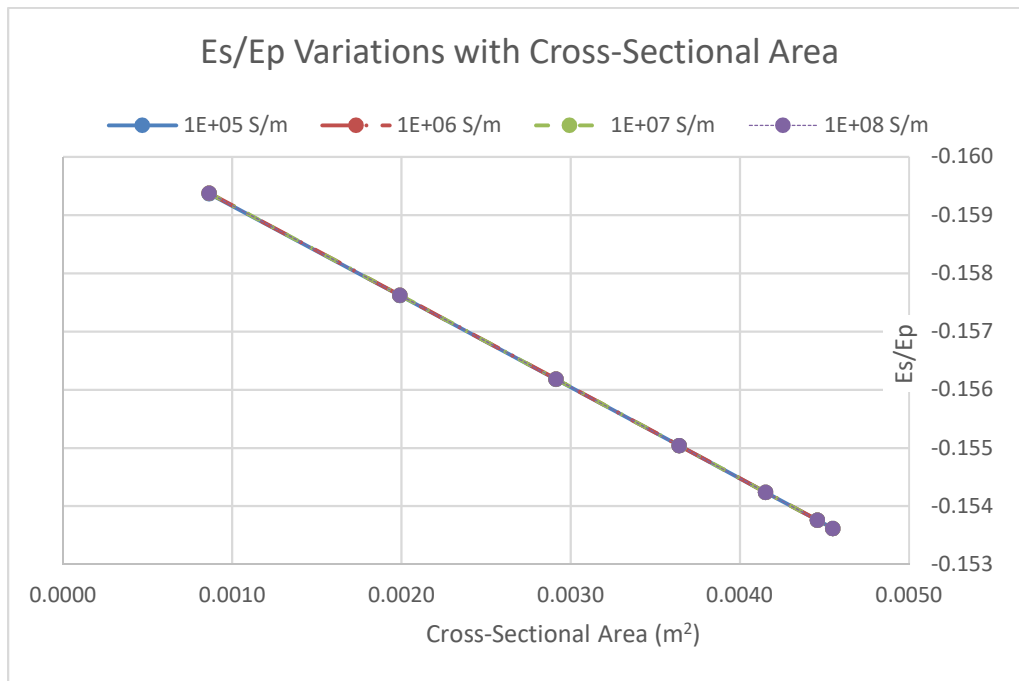


Figure 2.5: One segment analytic secondary to primary electric field ratio variations with increasing total volume of metal produced by an increasing wall thickness at four different given casing conductivities.

One of the most interesting aspects seen in figure 2.5 in the case of our analytic solutions is that the plots for each varying casing conductivity overly one another perfectly. This speaks towards the saturation of casing conductivity values in the derived expressions. Casing conductivity within the analytic expressions comes into account only within the A_{ii} calculations, and when differentiating between values which are all so large there is little effect overall regarding

secondary fields. A more obvious observation is the decrease in secondary electric fields with increasing metal volume. However, the decrease in E_s is very small meaning that, at least within the confines of length that I can work with within the pool experiments, the analytic expressions suggest inner radius may not be the largest defining factor in observed secondary responses.

2.2.2: Analysis of Analytic Expressions for Varying Length

I will now study the effects of varying length on the secondary electric fields. These effects will be observed from a constant outer radius of 0.0381 m, inner radius of 0.03429 m and lengths varying from 0.1524 m to 0.7759 m. This will allow me to explore the full range of lengths I can work with in the experimental pool environment given its maximum depth of ~1 m. Figure 2.6 highlights the growth in secondary fields with increasing casing length.

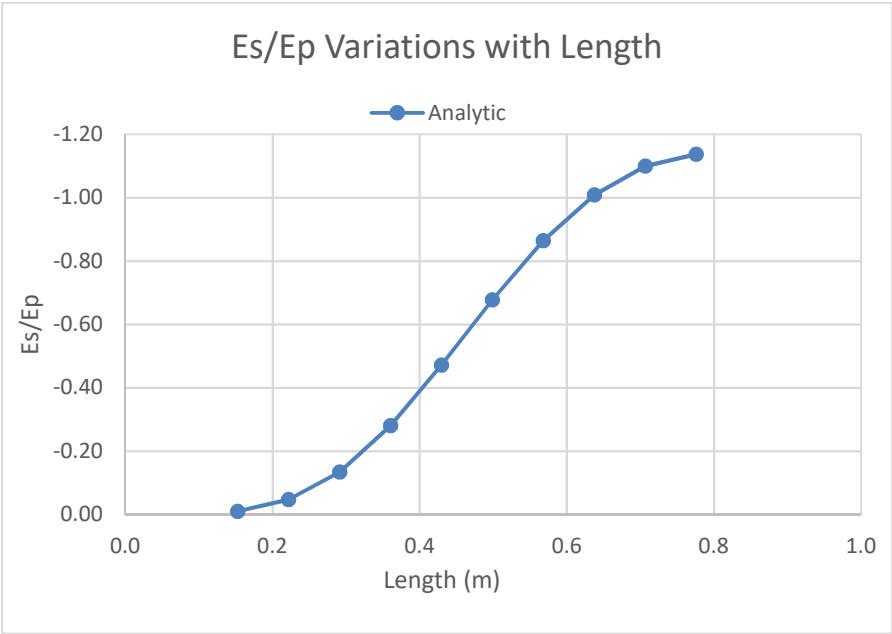


Figure 2.6: One segment analytic secondary to primary electric field ratio variations produced by a steadily increasing casing length. The outer and inner radius are kept constant at 0.0381 m and 0.03429 m respectively.

As would be expected from the heavy dependency of casing length in expressions (2.12) and (2.23), I see significant growth of the secondary fields with increasing length. At a length of 0.1524 m (6 in) the E_s/E_p ratio is nearly zero meaning the data would be completely dominated

by the primary fields, whereas at the maximum length tested of 0.7759 m (~30.5 in), the observed secondary field is nearly 20% higher than the primary field. This holds large implications regarding the planning of lab scale experiments as I may not expect much of a response to be visible in the data when conducting surveys over casings of shorter lengths.

2.2.3: Analysis of Analytic Expressions for Varying Casing Width

I will now analyze the effects of increasing outer radius on produced secondary electric fields. Following suit from the study of increasing casing wall thickness I will study these effects as produced by the same three different lengths, 0.3048 m, 0.4572 m, and 0.762 m. I will keep a constant wall thickness throughout these studies of 0.00381 m, and will increase the outer radius from 0.0164 m to 0.1905 m.

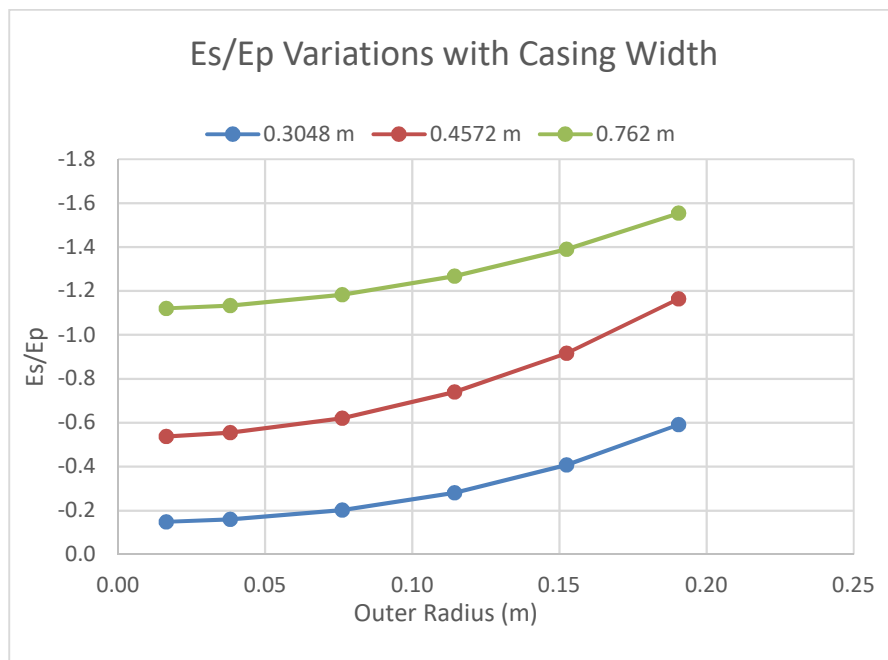


Figure 2.7: Variations in ratios of one segment analytic secondary to primary electric fields produced from a steadily increasing total casing width. Both length and wall thickness are held constant. Outer and inner radius are increased together from 0.0164 m outer radius to 0.1905 m.

Figure 2.7 shows the largest contributor to variations in our E_s/E_p ratio within the plot comes from the three different lengths being studied, however given that we are now seeing much larger radii I begin to observe larger increases in secondary fields due to casing width as well as I pass

the 0.10 m outer radius line. Although it may be difficult to work with a casing of outer radius 0.10 m in the lab scale pool environment this result can prove useful when evaluating possible secondary response magnitudes at the mid to large scale levels also studied throughout this thesis. Beyond 0.10 m outer radius we begin to exceed that which would be realistic in the field as well, however, it is theoretically useful to understand the casings continued response at its most extreme dimensions.

2.2.4: Analysis of Analytic Expressions for Host Conductivity

I will now study how material properties of the electrically conductive casing itself as well as the background conductivity of the experimental environment affect secondary fields. Within this sub-section I will plot again E_s/E_p but as a function of ρ_H/ρ_C . This means that lower values along the x-axis correspond to a more electrically conductive background.

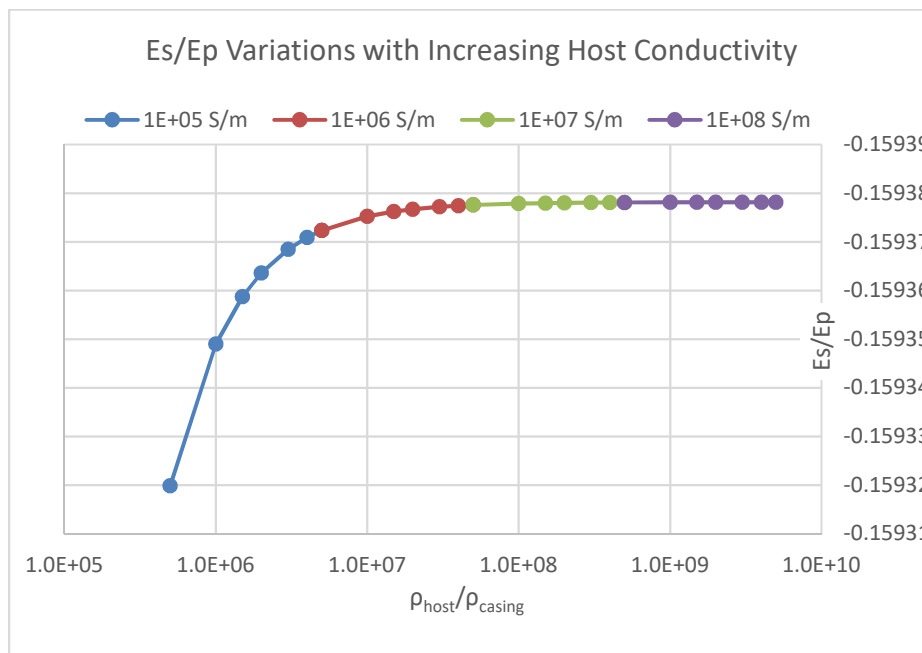


Figure 2.8: One segment analytic secondary to primary electric field variations with an increasing host conductivity at 4 different casing conductivities. Here the X-axis is ρ_H/ρ_C meaning a decrease in host conductivity is an increase along the axis. Spatial casing properties are held constant at a length of 0.3048 m and outer and inner radius of 0.0381 m and 0.03429 m respectively. Background conductivities of 0.02, 0.025, 0.0333, 0.05, 0.0666, 0.1, and 0.2 S/m were analyzed.

Variations in Es/Ep ratios produced from an increasing host conductivity are very small, however, the strongest of these variations occur at the lowest values of ρ_H/ρ_C as in this area we have a lower conductivity within the casing, and a higher conductivity in the background leading more current to exist outside the casing. This observation is of limited use in the mid to large scale experimental environment, where the electrical conductivity of the casing and the background conductivities are fixed. It is valuable though at the lab scale where both variables can potentially be manipulated if necessary to produce a secondary field response representative of what would be expected at full scale experiments.

2.3: Field Variations with Changing Casing Properties: MoM Solution

I will now study the same casing properties, yet with fully converged numeric values calculated using the MoM code. For the following calculations each casing example has been discretized vertically into 100 individual segments. I know from section 2.1.3 values calculated from the analytic expressions will not match exactly with those found in this section, however through using a root-mean-square (RMS) method ($RMS_{error} = \frac{1}{n} \sqrt{\sum_{i=1}^n (MoM_2/MoM_1 - ANA_2/ANA_1)^2}$) where n is the number of data points being tested, MoM is the Method of Moments calculated values and ANA is the solution found from the derived expressions of section 2.1 and the subscripts represent two consecutive values of each, will see which parameters can be best estimated using the derived analytic expressions when summarized in section 2.4. I compare the slopes between consecutive values as this gives insight into the magnitude of the variation in Es/Ep produced through each approach through the same change in casing parameter. I will find that the magnitude of variations produced in the secondary fields by equal changes in casing properties using the two different methods are very similar in some cases.

2.3.1: Analysis of Fully Converged MoM Solution for Cross-Sectional Area

Again, for the analysis of the MoM method I will begin by studying the numerically calculated variations in secondary response from an increasing cross-sectional area within the electrically conductive casing. I use the same parameters as in section 2.2.1, testing casings of conductivities 1E+05 S/m, 1E+06 S/m, 1E+07 S/m and 1E+08 S/m. I use a modelled casing of

length 0.3048 m, an outer radius of 0.0381 m and a steadily decreasing inner radius beginning with 0.03429 m and ending with a nearly solid casing of inner radius 0.0019 m.

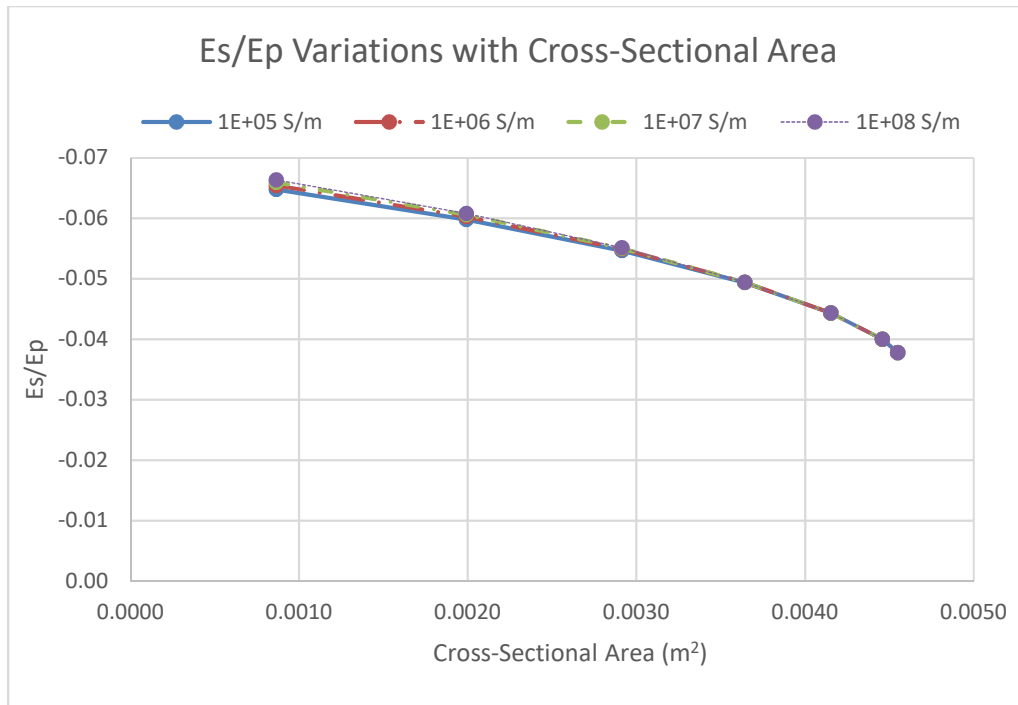


Figure 2.9: Fully converged MoM secondary to primary electric field ratio variations with increasing cross-sectional area produced by an increasing wall thickness at four different given casing conductivities.

I see the same general decreasing trends in E_s/E_p I have witnessed in section 2.2.1. With our numeric evaluation of variations with cross-sectional area I can see differences, though very small, between plots with different casing conductivities before they converge at a cross-sectional area around 0.0025 m^2 . Again, this is likely due to the conductivities of casing material being so high that there is saturation even within the numeric calculations given a sufficient volume of metal. RMS error values for each of our different studied casing conductivities were very low suggesting that the analytic expression may be able to predict the effect of a changing inner radius on secondary responses. At the lowest conductivity value of $1\text{E}+05 \text{ S/m}$ there is a calculated RMS error of 0.0811, at $1\text{E}+06 \text{ S/m}$ I have 0.0826, $1\text{E}+07 \text{ S/m}$ gives us 0.08377, and at $1\text{E}+08 \text{ S/m}$ I find 0.0847.

2.3.2: Analysis of Fully Converged MoM Solution for Varying Length

I will now view secondary fields produced from a steadily increasing casing length calculated by the numeric approach. I use the same parameters as in section 2.2.2 holding a constant outer and inner radius of 0.0381 m and 0.03429 m respectively and increasing casing length from 0.1524 m to 0.7759 m to explore the full range of lengths that can be surveyed within the lab-scale pool environment.

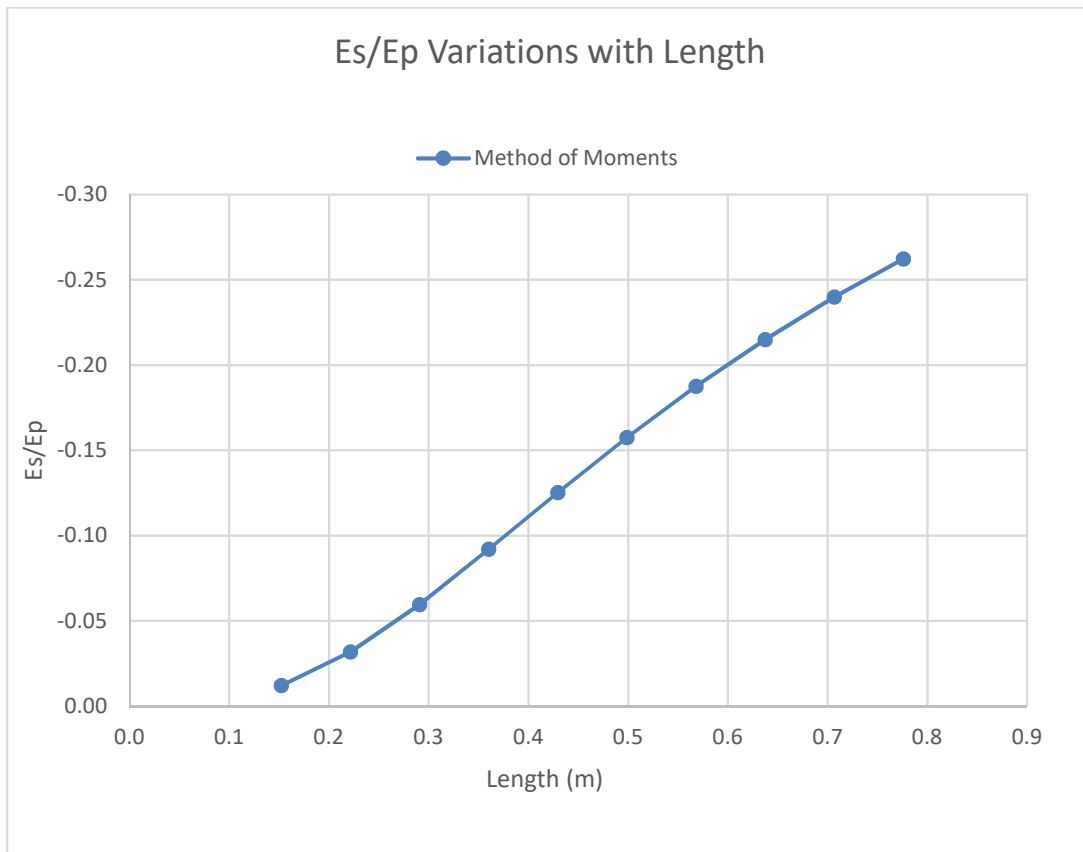


Figure 2.10: Fully converged MoM secondary to primary electric field ratio variations produced from a steadily increasing casing length. Both outer and inner radius are held constant at 0.0381 m and 0.03429 m respectively.

Figure 2.10 shows a common increasing trend to that seen in section 2.1.2 but the tails of the line that begin to taper at the extremes of the plotted lengths are weaker than in the analytic case. I have again included a plot in figure 2.11 comparing the analytic and fully converged MoM

solutions together, now with a $\log(10)$ y-axis due to the wide variations in secondary fields between the two methods.

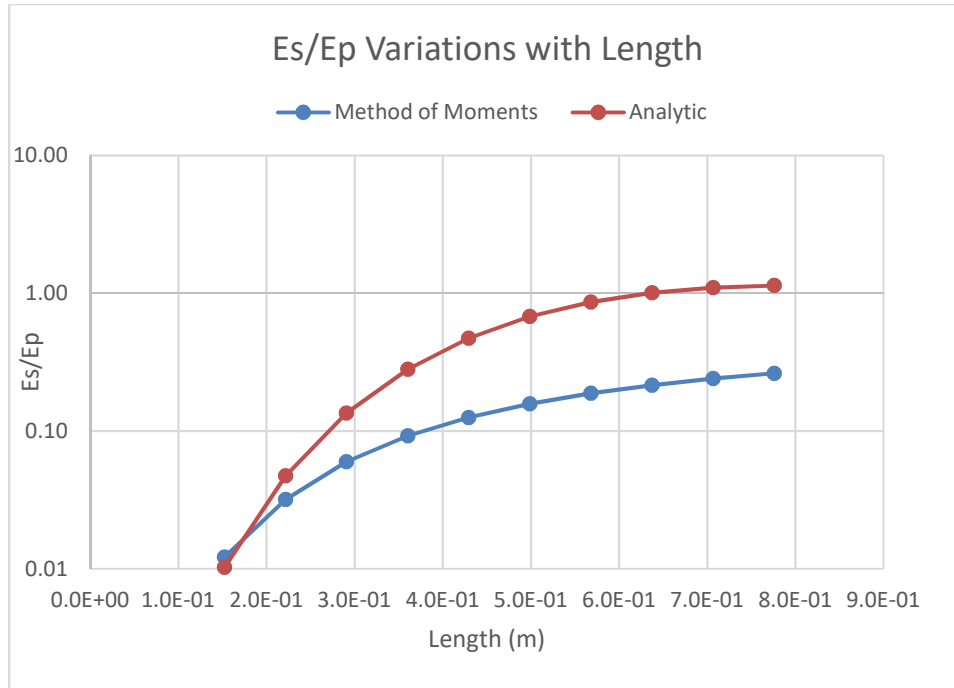


Figure 2.11: Secondary to primary electric field ratio variations produced from a steadily increasing casing length at both analytic and fully converged MoM levels. Both outer and inner radius are held constant at 0.0381 m and 0.03429 m respectively. Length increases from 0.1524 m to 0.7759 m by increments of 0.0692 m.

RMS error values in the case of varying length are also considerably different showing a value of 0.768686 between the analytic and numeric methods. This higher value is due to the much more accurate calculation of the secondary fields in the numeric approach when studying a casing of a very short length. Figure 2.11 shows that our two solutions are nearest one another at the shortest casing lengths. This makes sense as the analytic solution takes the casing as one single segment with a constant current, whereas the MoM approach finely discretized the casing capturing any variations in current along the casing's length giving more accurate secondary field calculations.

2.3.3: Analysis of Fully Converged MoM Solution for Varying Casing Width

I now examine the secondary field variations produced from an increasing total width of the casing with a constant wall thickness of 0.00381 m in figure 2.12. The same outer radius values from figure 2.7 are examined in this MoM case.

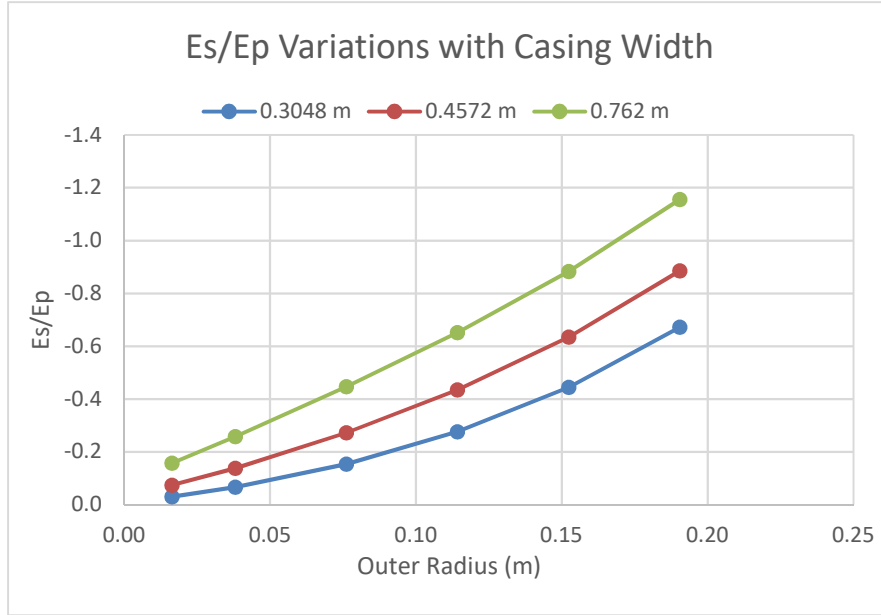


Figure 2.12: Variations in ratios of fully converged MoM secondary to primary electric fields produced from increasing total casing width. The casing length and wall thickness are kept constant.

There is a steeper growth of E_s from increasing casing width than observed in figure 2.7, particularly for the 0.762 m long casing. There is also a noticeable increase in the slope of the curves at outer radii larger than ~ 0.1 m for the two shorter casing lengths, a trend also noticed analytically. I have again plotted both analytic and fully converged MoM solutions together for the 0.3048 m length case for easier visual comparison in figure 2.13.

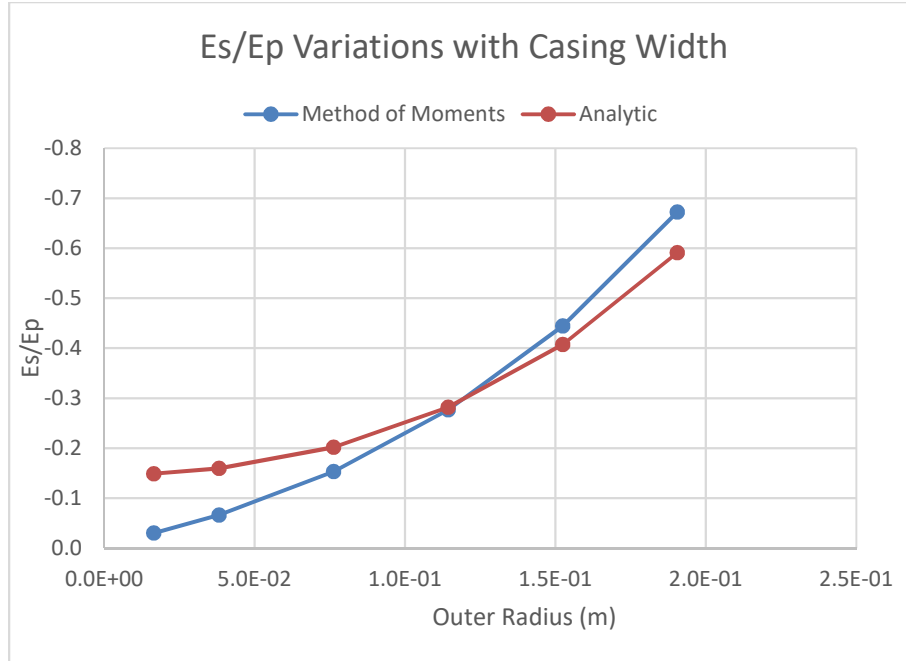


Figure 2.13: Shows variations in ratios of fully converged MoM and derived analytic secondary to primary electric fields produced from a steadily increasing total casing width. Both length and wall thickness are held constant.

There is a calculated RMS error of E_s of 0.7193 for the 0.3048 m casing, 0.57 for the 0.4572 m case, and 0.4739 for that of the 0.762 m casing. Again, this shows that the analytic electric field values themselves are not accurate, but when moving away from the extremes of whichever casing dimension is manipulated (such as a near solid or very short casing) the trends between a variation in secondary fields and an equal change in that dimension between the two methods are close enough to one another that the derived expressions may be used to estimate this variation.

2.3.4: Analysis of Fully Converged MoM Solution for Varying Host Conductivity

I now study the MoM results calculated from changes in both casing and background conductivity. I will study the same four casing conductivities seen in section 2.2.4. Along the x-axis I plot the ratio of host to casing resistivity.

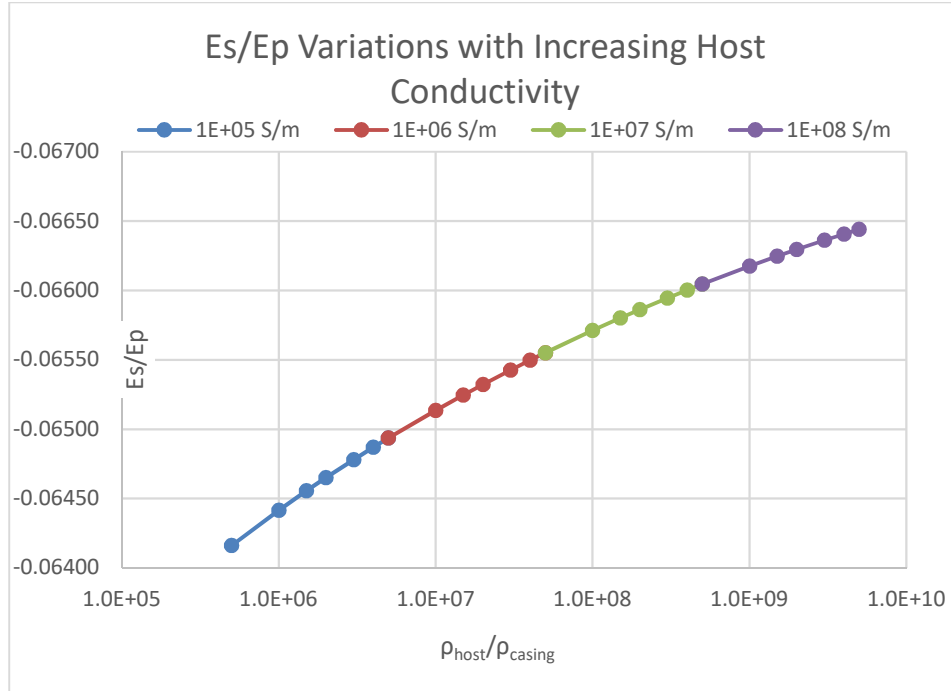


Figure 2.14: Fully converged MoM secondary to primary electric field variations with an increasing host conductivity at four different casing conductivities. Here the X-axis is ρ_H/ρ_C meaning a decrease in host conductivity is an increase along the axis. Casing dimensions are kept constant at a length of 0.3048 m and outer and inner radius of 0.0381 m and 0.03429 m respectively. Background conductivities of 0.02, 0.025, 0.0333, 0.05, 0.0666, 0.1, and 0.2 S/m were analyzed.

Figure 2.14 again shows lower E_s/E_p values than the analytic solution (Fig. 2.8). From analyzing figures 2.8 and 2.14 it can be seen that both solutions show little dependency on casing and host conductivity for the conductivity range tested, however a slightly stronger variation in E_s/E_p is produced in the MoM case. The analytic expressions correctly predict this lack of dependency and show values very similar to those calculated using MoM. Here I find RMS values in a casing of conductivity 1E+05 S/m of 0.0013, in 1E+06 S/m of 0.001, in 1E+07 S/m of 0.0008 and in the most conductive case of 1E+08 S/m of 0.0007.

2.4: Theory Conclusions

This study holds large implications for every scale of experimental work discussed in this thesis. Arguably the most useful of which applies to its application towards the lab scale pool experiments. I have a limited amount of space to work with in the pool meaning I must make the most of every variable dimension of the electrically conductive casings surveyed to ensure a

proper, clean secondary response is produced that may then be modelled with our MoM numeric modelling code. These secondary responses at the pool-scale may then be used to better understand responses from similar casings at the large-scale. Several issues displayed themselves early on with pool data acquisition related to weak or even imperceptible secondary responses. This was due to the belief that a simple geometric scale-down of the large-scale field data acquisition would be the most efficient way to begin data collection within the pool. At the large-scale level the diameter of the vertical borehole being surveyed was roughly 0.0016 times the length of the casing. When scaled down to the pool, this would require a very thin diameter, or very long casing to stay true geometrically. Given the depth limitations of the pool, I decided to survey a very thin casing. In early attempts to gather data within the pool I did just that and suspended a casing with a 1 cm diameter beneath the central electrode and found that the secondary response was undetectable entirely. This observation led to the commencement of this theoretical study which has aided in building a multitude of successful lab-scale experiments as well as giving a preliminary look into what types of secondary responses I may expect from casings of varying material and spatial properties.

The theory developed and explored in this chapter has also proved instrumental when analyzing mid-scale experiments held on the Colorado School of Mines campus particularly towards the case of an inline DC survey over a horizontal aluminum pipe. Though the length and material of the pipe were known, steps were not taken during the burying of the pipe to record its inner and outer diameter. Due to this, the numeric modelling of the survey was at first an exercise in high-level, educated guess work. However, after an initial model was calculated and the level of error from the real field data was determined I was able to implement what has been learned from this chapter regarding variations in secondary electric fields with casing wall thickness and total diameter to hone in on an inner and outer radius that produce secondary field values within an acceptable margin of error from the field.

The theory discussed within this chapter has already proven a useful in assessing important aspects of electrically conductive casings and how they will affect secondary electric fields. They provide information that allows a better fit of MoM models to real data at the large and mid-scale and aid in planning more effective lab-scale experiments.

Table 2.1: Table showing RMS error fit between numeric MoM approach and analytic expressions derived within this chapter for variations in secondary electric fields from a given change in electrically conductive casing property.

Length		Wall Thickness	Width
0.3048 m	RMS Error	0.0837878	0.7193
0.4572 m	RMS Error	0.0639293	0.57
0.762 m	RMS Error	0.0487449	0.4739
Conductivity		Host Conductivity	Metal Volume
1E+05 S/m	RMS Error	0.0013	0.0811
1E+06 S/m	RMS Error	0.001	0.0826
1E+07 S/m	RMS Error	0.0008	0.08377
1E+08 S/m	RMS Error	0.0007	0.0847
Length	RMS Error	0.768686	

Through RMS error analysis shown in table 2.1 and discussed in sections 2.2 and 2.3 I have shown that the analytic expressions derived in section 2.1 may not always provide accurate secondary field values, however in cases with lower RMS values they may be used to estimate variations in the secondary response produced from a given change in casing properties.

2.5: Finite-Element Modelling

To conduct a proper lab scale experiment, it is necessary to first understand what environment is necessary to produce a well-controlled and reproducible result. When conducting electrical experiments within a tank this is an incredibly important undertaking as the boundaries of your tank will very likely be electrically resistive and introduce boundary effects in the data. Due to this, prior to beginning such an experiment it is useful to utilize a modelling software to understand what can be expected to see as a result of the experimental environment.

2.5.1: Model Parameters

I have used of Thomas Günther’s Boundless Electrical Resistivity Tomography (BERT) finite element modelling code (Günther et al 2017). BERT makes use of a tetrahedral meshing process and calculates electrical potentials, which can be converted into apparent resistivities, from given ground conductivity distributions and source current densities. The code assumes a

point electrode source and a Neumann boundary at the surface to avoid current flow thus simulating the air-Earth contact. For my own purposes I also introduced Neumann boundaries on the remaining five boundaries of the modelling environment that act as the resistive edges of my experimental tank. Given the variety of casing sizes and orientations to be surveyed for my experiment a rather large environment is necessary to both contain the elements of my experiment as well as avoid extreme edge effects from resistive boundaries. To fit this criterion, I found a 6 m X 3.5 m X 1.2 m inflatable pool capable of holding ~19,000 liters of water with PVC laminated sidewalls. Due to the inflatable ring at the top of the pool being considered in its depth, and the nearly trapezoidal shape of the pool its volume is roughly 19 m³



Figure 2.15: Image of the lab-scale pool environment with dimensions.

To best understand the expected edge effects produced within the experimental environment of the pool I decided to use the BERT finite element modelling software to simulate DC data at two levels of scale while holding constant elements such as survey geometry, background conductivity, and the dimensions and material of a simulated electrically conductive casing. The two experimental scales to be modelled are that of a rectangular prism the dimensions of the

inflatable pool, and a larger prism of 25 m X 25 m X 20 m representative of a pseudo-half space environment that will be free of any edge effects produced from model boundaries. By comparing the results of these two models, I was able to understand the magnitude and spatial positioning of the edge-effects produced at the pool scale. For the survey geometry itself I make use of a dipole-dipole array made of twenty point-source electrodes with a spacing of 0.10 m for a total array length of 1.9 m. Within each of the two scales being modelled two different scenarios have been simulated. The first scenario is a homogeneous model with no variations in conductivity throughout its entirety, and the second containing a 0.1 m diameter, 0.8 m long casing with an electrical conductivity of $1E-5$ S/m and the top located 0.015 m from the air-Earth interface. Both exhibit a background resistivity of $1 \Omega\text{m}$. Figures 2.16, 2.17 and 2.18 show the pool scale and pseudo-half space models containing the electrically conductive casing. The pool environment has been modelled to depth of 1.2 m which is slightly deeper than possible in the experiment due to the inflatable ring around the top of the pool being considered in the total 1.2 m.

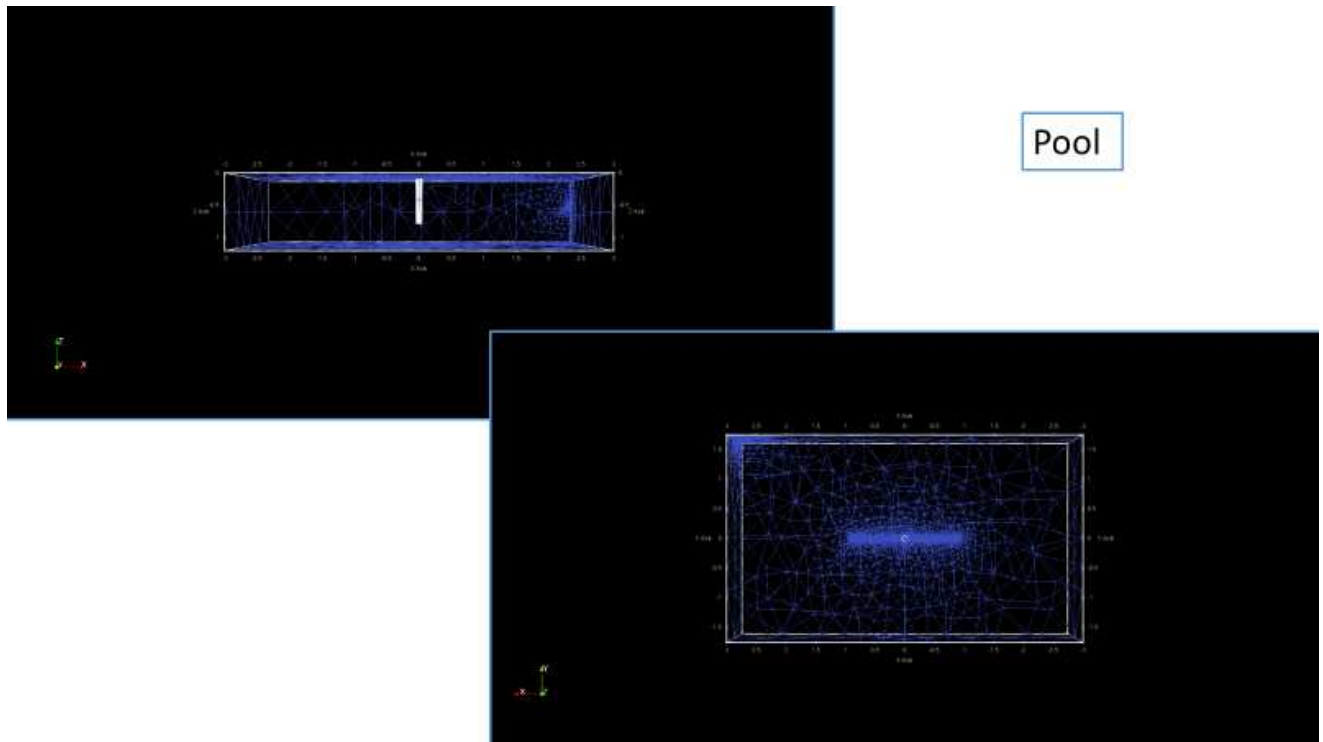


Figure 2.16: Finite-element modelling domain with dimensions of pool (6 m X 3.5 m X 1.2 m).

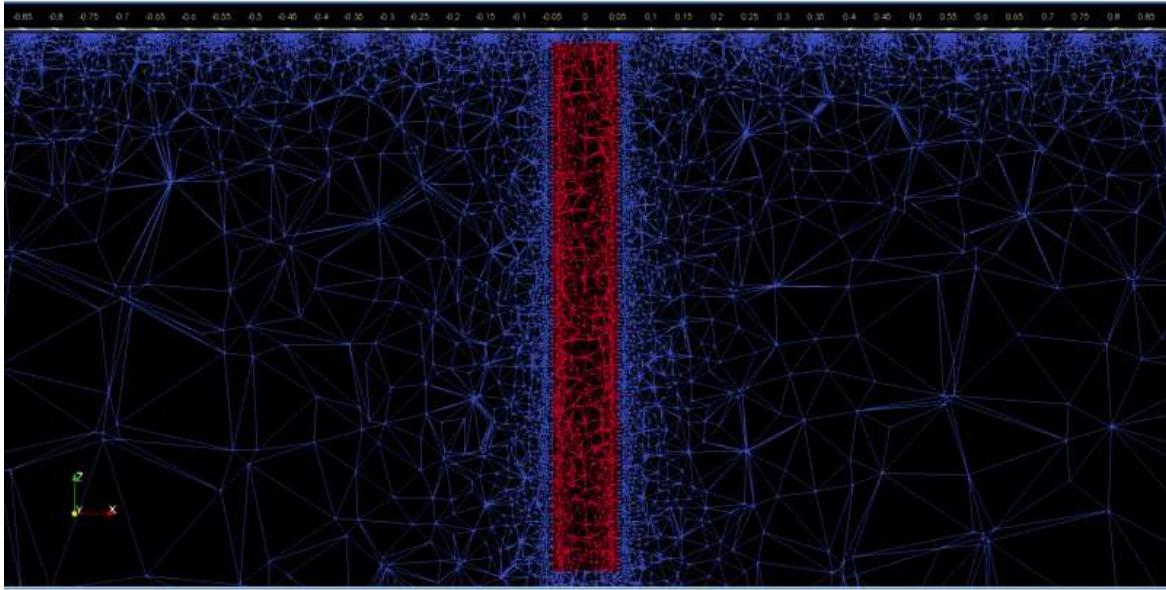


Figure 2.17: Cross-section through the pool modelling domain showing mesh discretization in area surrounding electrically conductive casing and surface electrodes.

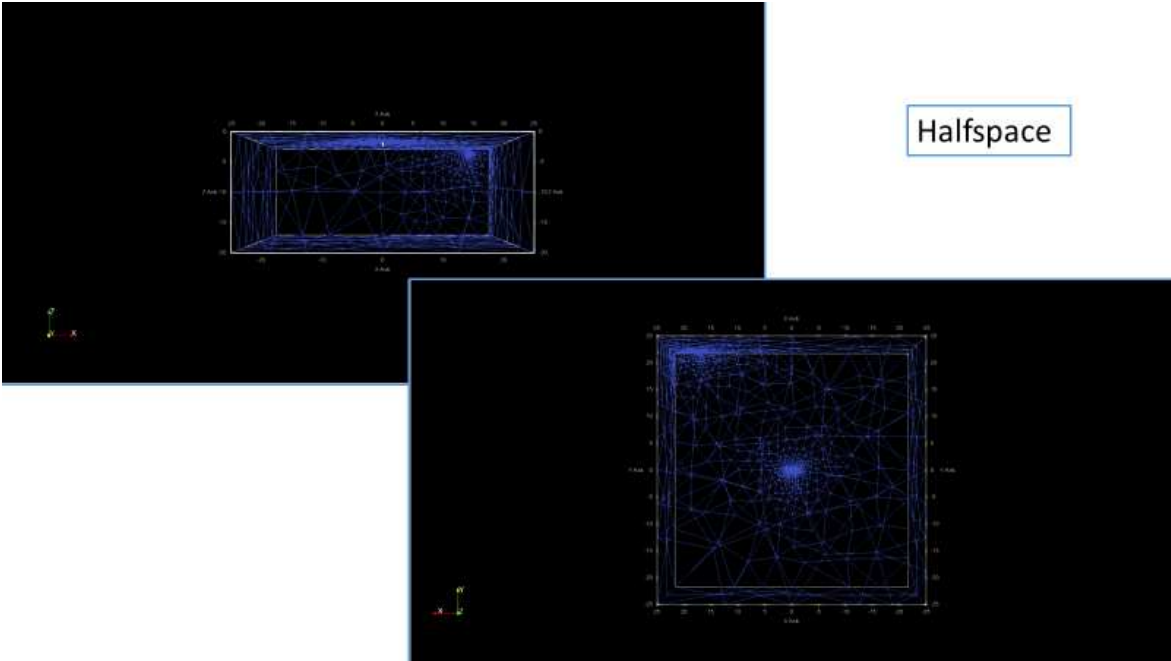


Figure 2.18: Finite-element modelling domain with dimensions of pseudo-half space (25 m X 25 m X 20 m).

These figures show the structure of the irregular tetrahedral mesh used within the electrical potential calculations carried out by BERT. There is a finer discretization near both the electrodes and the included casing. There is also a more finely meshed zone in the upper-left area of the modelling environment when viewed in plan view that corresponds to an imaginary reference electrode being used to test the efficiency of the designated Neumann boundaries.

2.5.2: Model Results and Conclusions

I first investigate the simulated data found from both modelling scales in the absence of an electrically conductive cylindrical casing. The first two pseudosections shown in figure 2.19 show data simulated in the pseudo-half space and within the pool model space.

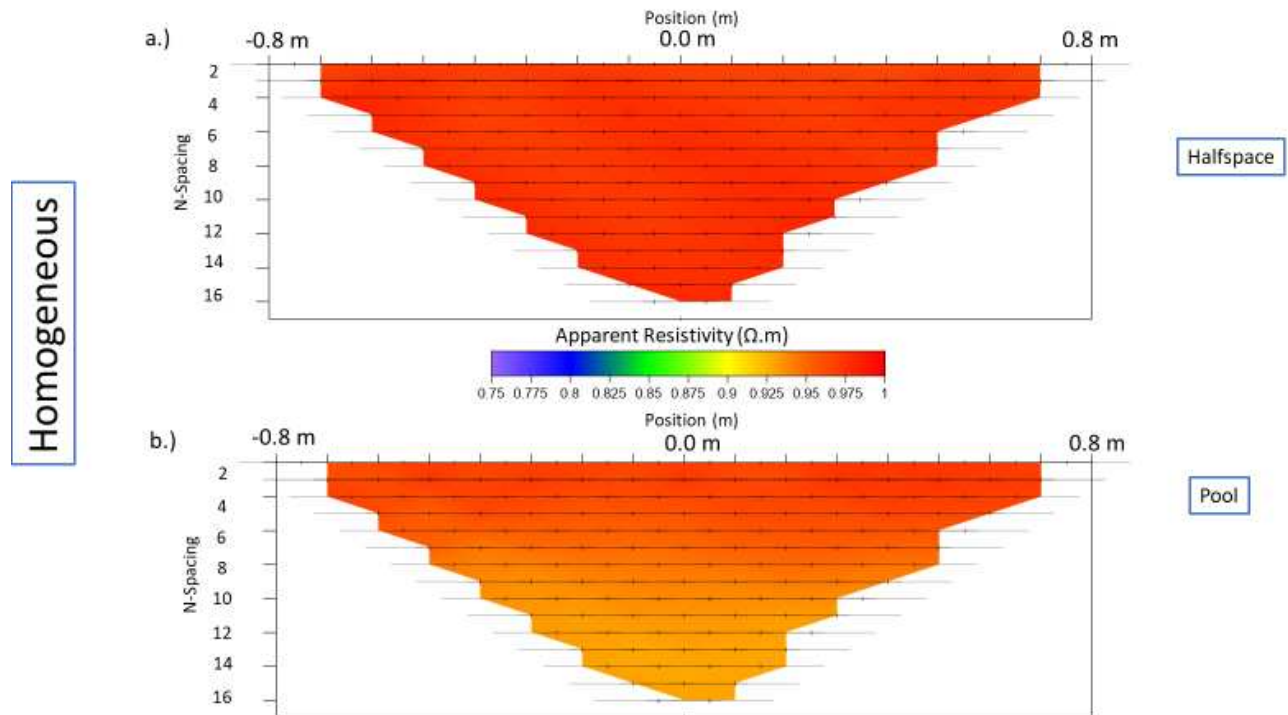


Figure 2.19: Finite-element modelled data with a background resistivity of 1 Ωm shown with a homogeneous medium (a) in our pseudo-halfspace scale and (b) at the pool-scale.

It is immediately evident that there is an effect from the resistive boundaries when viewing the data modelled from the pool scale. There is a drop in apparent resistivity from the background of

1 Ωm to that of $\sim 0.925 \Omega\text{m}$ at depth. To best describe the difference between the two scales in a more quantitative sense I study the percent difference in figure 2.20.

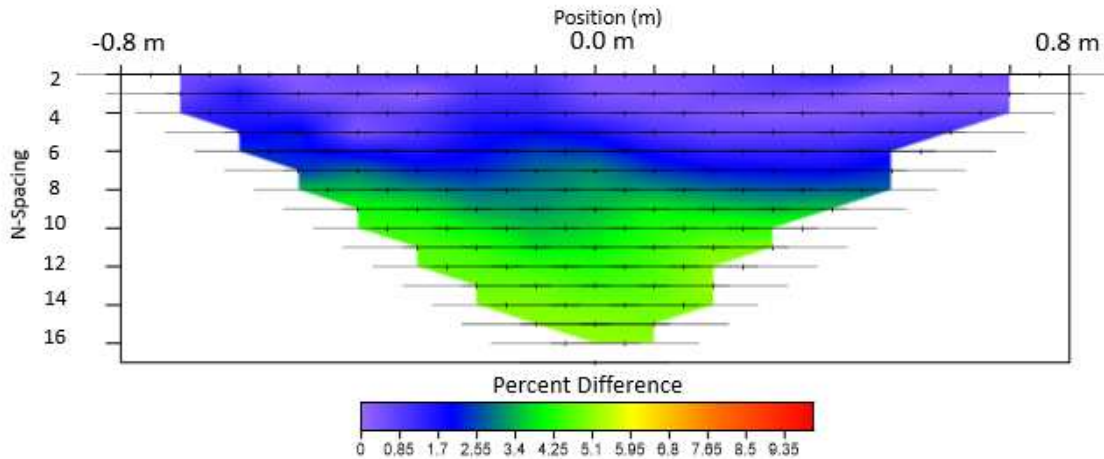


Figure 2.20: Point-by-point percent difference between the two different modelling scales with a homogeneous model space.

The percent difference plot shows that there is a maximum difference in apparent resistivity between the pool environment and pseudo-halfspace of around 5% in an entirely homogeneous model space. Figure 2.19, however, shows that at depth the pool model environment drops $\sim 8\%$. This means that the pseudo-halfspace is also being affected by resistive edge effects. The much-reduced edge effects seen in the pseudo-halfspace, however, give confidence in being able to interpret the extent of these edge effects. The rectangular prism assumption used in the finite-element modelling will lead to slightly stronger resistive edge effects in the true pool environment given its nature. Given the modelled edge effects are relatively mild at a $\sim 8\%$ difference in a homogeneous pool environment I will now model the pool with the added complication of a vertical, cylindrical steel rod to our model space. Within this model I will be aiming to see if the secondary response produced by the rod itself is hindered by the observed edge effects of the pool. Again, I will show models produced within both experimental scales to highlight the edge effects from the electrically resistive walls of the pool. Figure 2.21 shows apparent resistivity pseudosections for both scales given a background resistivity of 1 Ωm and a solid steel rod 0.8 m long, 0.1 m diameter and with a conductivity of $1\text{E}-05 \text{ S/m}$.

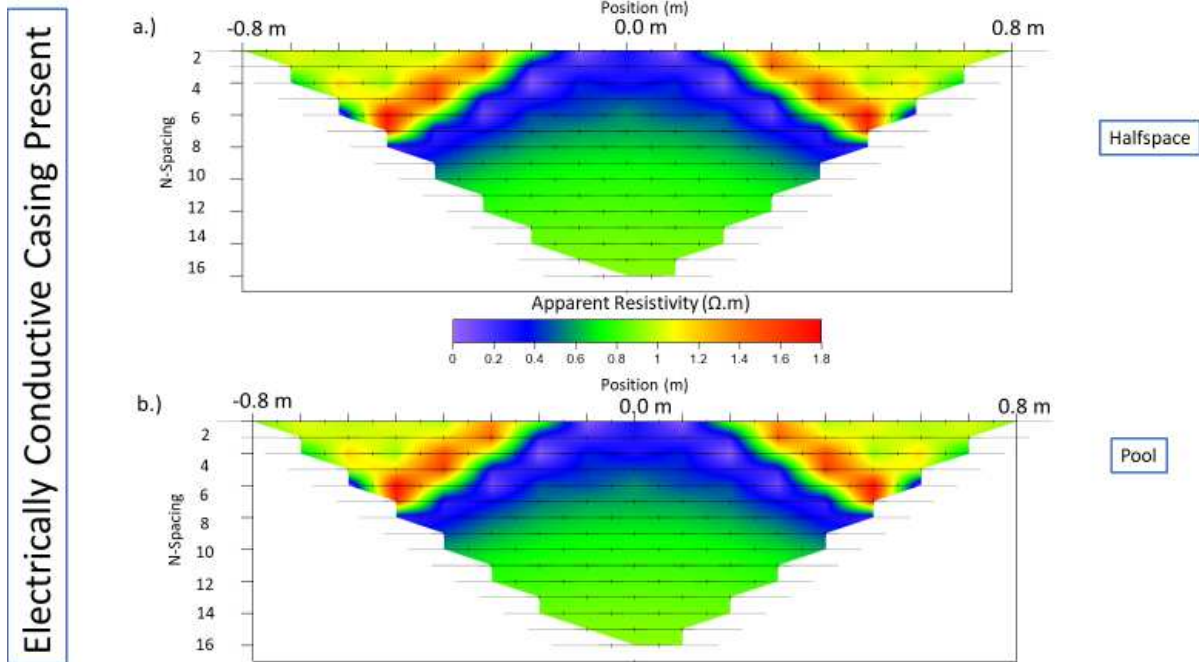


Figure 2.21: Finite-element modelled data with a background resistivity of $1 \Omega\text{m}$ shown in the presence of an electrically conductive rod (a) in our pseudo-halfspace scale and (b) at the pool-scale.

In the presence of the electrically conductive rod the secondary response of the conductive body begins to drown out the edge-effects from the bottom of the pool, and there is very little difference between the two model scales. Figure 2.22 shows the point-by-point percent difference between the responses of the pseudo-half space case and the pool environment. As was observed from the response pseudosections themselves there is very little difference between the two modelling scales when observed in the presence of an electrically conductive casing. The finite element modelling shows a maximum of just $\sim 2\%$ difference between the two scenarios. This is a result that leads to the conclusion that the pool case with the dimensions we have modelled will provide an excellent environment, with minimal resistive edge effects, to conduct our lab scale experiments.

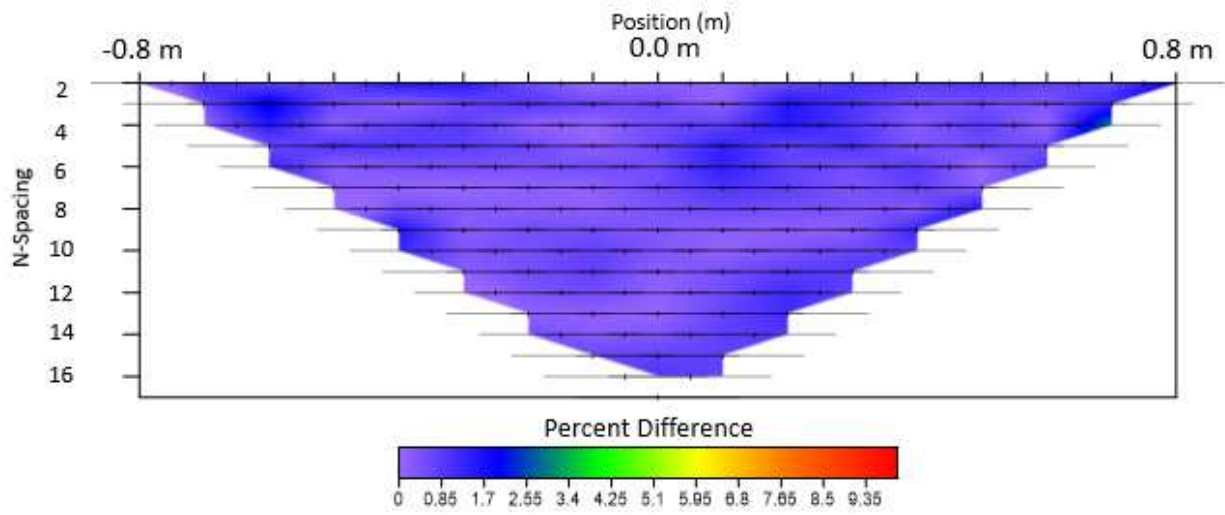


Figure 2.22: Point-by-point percent difference plot between the two different modelling scales in the presence of an electrically conductive rod.

CHAPTER 3

DC RESISTIVITY EXPERIMENTS AND COMPARISONS WITH METHOD OF MOMENTS MODELLING

3.1: Introduction of Lab-Scale Experimental and Method of Moments Data

For lab scale experiments I chose to make use of a 6 m X 3.6 m X 1.2 m PVC laminated inflatable pool. It was determined from the finite element modeling of chapter 2.5 that an experimental environment of this size would be large enough to hold lab scale equipment and minimize effects produced by the boundaries of the pool itself – resulting in a contained experiment where edge effects can be ignored. In this environment it is possible to test responses not only from casing geometries encountered in the field, but also more unique scenarios such as complex infrastructure geometries and variations in casing composition – situations difficult to fully examine in field-scale experiments. The theoretical study covered in chapter 2 allowed optimization of experimental design parameters such as casing length, diameter, wall thickness and geometry. A frame was constructed to suspend the experimental array above the pool so that its geometry is adjustable.



Figure 3.1: Photograph of the lab-scale pool experiment. A 2-inch-thick PVC pipe is suspended between two large pieces of lumber by rope allowing the PVC pipe to be lowered down to the water. Nineteen galvanized steel electrodes are driven through the pipe at 0.10 m intervals for a total array length of 1.8 m. The electrodes are attached to insulated 12 AWG wire running out of the pool and connected via banana plugs to the AGI USA SuperSting R8 DC resistivity instrument.

The galvanized steel electrodes are driven through a PVC pipe to prevent current from travelling through the frame itself and direct all of the injected current entirely into the pool. Cables connected to the electrodes lead out of the pool where they are connected to the AGI USA SuperSting R8 DC resistivity instrument. There is a total of 19 electrodes spaced 0.10 m apart creating a full array length of 1.8 m. Casings surveyed throughout the following experiments were bought from a local Home Depot. Due to this, there are some limitations put on the physical properties of several experiment. For example, two casings made of different materials are surveyed to determine the effect of the metal's conductivity, however there is also a variation in the thickness of one of the casing's walls which must be considered.

3.1.1: Homogeneous Lab-Scale Data

The pool environment provides a unique opportunity to study casing properties and geometries that would be difficult to replicate in the field but are of great import to the greater project. Within this section I will show a wide variety of casings in length, radius, thickness, material and geometry and display how these variations effect experimental results.

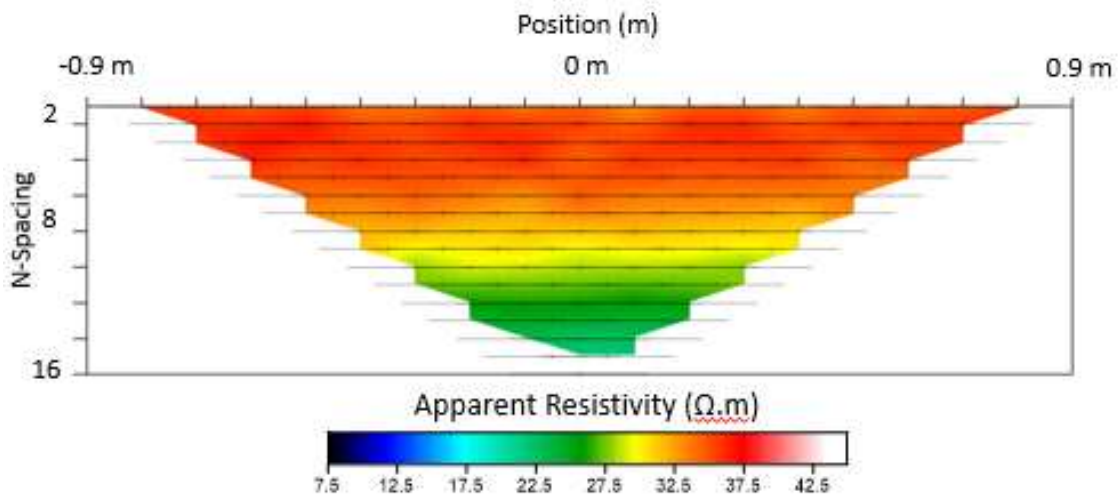


Figure 3.2: Apparent resistivity pseudosection taken within the lab-scale pool environment in a perfect homogeneous case.

Before beginning to study experimental data with electrically conductive inclusions it is useful to understand the media itself. Figure 3.2 shows an apparent resistivity pseudosection free of any

casings in the water. A dipole-dipole electrode array was used in this survey as well as all that follow. The entire pseudosection shows nearly equal apparent resistivities until data level ~10 where I begin to see the drop in apparent resistivity with depth due to resistive edge effects discussed in section 2.5.2. The upper zones of the pseudosection show values of ~34 Ωm with a drop in apparent resistivity due to the resistive edge effects to ~23 Ωm . I observe a slightly larger drop in apparent resistivity with depth in the experimental data than the 8% from background seen within the finite-element modelling. This is likely due to the imperfect nature of the experimental setup that was required to be outside. Due to this, the pool is not perfectly level and therefore the center where the array hangs is closer to 1 m in depth than the 1.2 m possible in a perfect environment. This results in higher current density with depth than would have been seen with the full 1.2 m and a stronger associated drop in apparent resistivity.

Reproducibility of lab-scale experiments such as this is of great importance. Particularly when the experiment is constructed outdoors where it is subjected to a wide variety of weather conditions. Depending upon the water temperature within the pool electrical resistivity measurements ranged from 30 to 35 Ωm . Over a three-month period, with background readings being taken every day that experiments were carried out, maximum RMS misfits between background readings saw a maximum of 0.29 where most were near 0.10. Outside of these small variations in background resistivity which could be accounted for in the modelling, other elements of experimental setup stayed constant. The electrode array was lifted far from the water surface between experiments minimizing corrosive effects on the steel electrodes. This led to very reproduceable experimental results throughout the life of the project.

3.1.2: Reference Casing Lab-Scale and Method of Moments Data

I begin with a hollow cylindrical casing of outer radius 0.0164 m, inner radius 0.0131 m, and length 0.3048 m made of galvanized steel with a conductivity of $8 * 10^6$ S/m. For the sake of later comparisons, I will refer to this initial casing as our reference. The casing is suspended vertically beneath the center of the array at electrode 10.

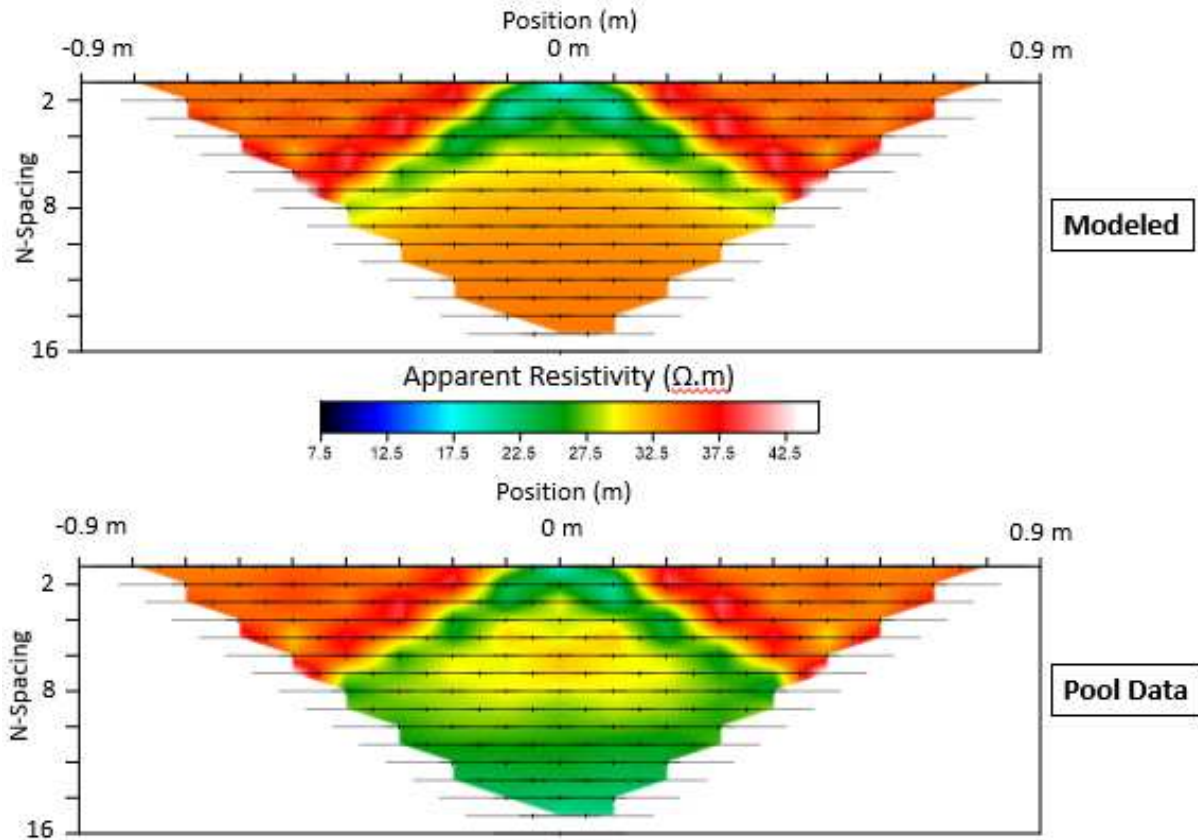


Figure 3.3: Apparent resistivity pseudosection showing experimental data versus MoM model over the reference casing composed of galvanized steel and of length 0.3048 m, outer radius 0.0164 m and inner radius 0.0131 m. This casing, of intermediate dimensional properties, will be used in many of the following sections of chapter three to compare variations in properties such as length, width, wall thickness and material composition that are either more or less extreme than our reference.

The similarities between the true pool data and the MoM numerically modelled data are immediately evident. There is a drop in apparent resistivity within the largest area of secondary response to around 20 Ωm from the background of 34 Ωm . The pool data shows the obvious decrease in apparent resistivity with depth that was expected from the finite-element modelling of section 2.5. From a qualitative perspective there is a good match between the two pseudosections. To allow for more quantitative comparison figure 3.4 below shows a point-by-point percent difference plot between the pool data, and the MoM modelled data in the presence of the reference casing. Percent differences were calculated using $Diff = 100 * ABS(1 - \rho_{MoM} / \rho_{Pool})$.

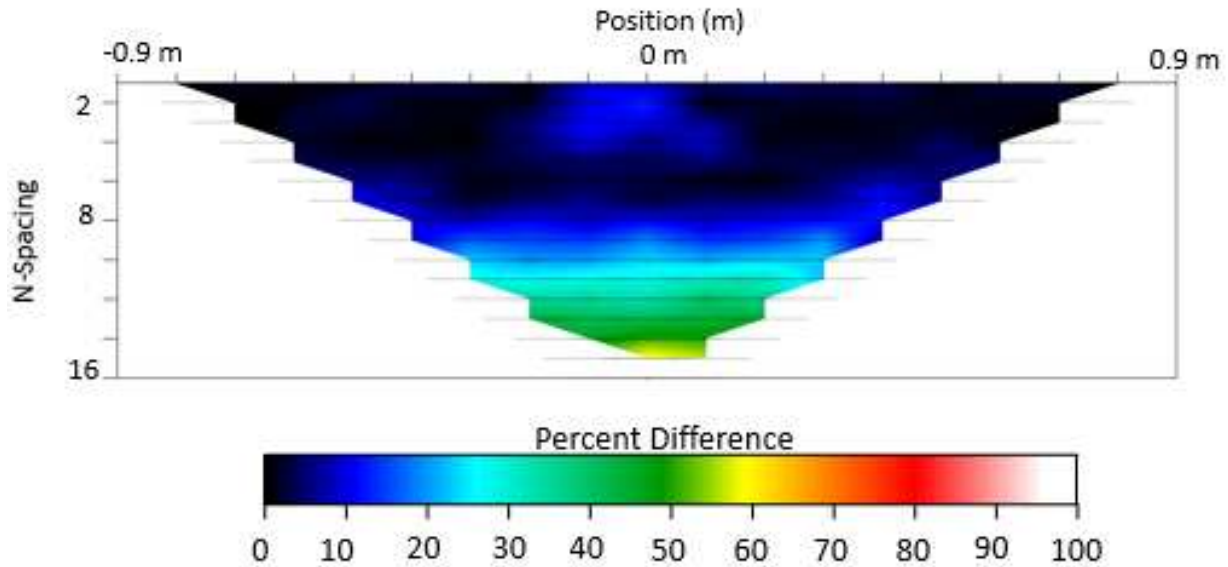


Figure 3.4: Point-by-point percent difference between the MoM model and the experimental data. There is a maximum of ~10% difference near the top center of the pseudosection. The larger misfit with depth correlates to the resistive edge effects produced from the bottom of the pool.

The immediately obvious mismatch is from the drop in apparent resistivity with depth seen within the pool. This is because for the MoM modelling I have assumed the host medium to be a boundless half space of homogeneous background resistivity. This effect produces a maximum percent difference of ~50% at data level 16. Given this was expected and well understood from finite element modelling I ignore this disagreement. Outside of this predicted error there is a smaller difference near the surface around $x = 0.0$ m of nearly 20% at maximum. This is due to a small level of immeasurable uncertainty regarding the exact depth at which the casing is suspended beneath the surface of the water in the pool data.

To further analyze the misfit between experimental data and the MoM model I have subtracted the background data from both cases to display only the secondary field seen in figure 3.5. This will allow us to view the secondary response nearly free of resistive edge effects from the bottom of the pool.

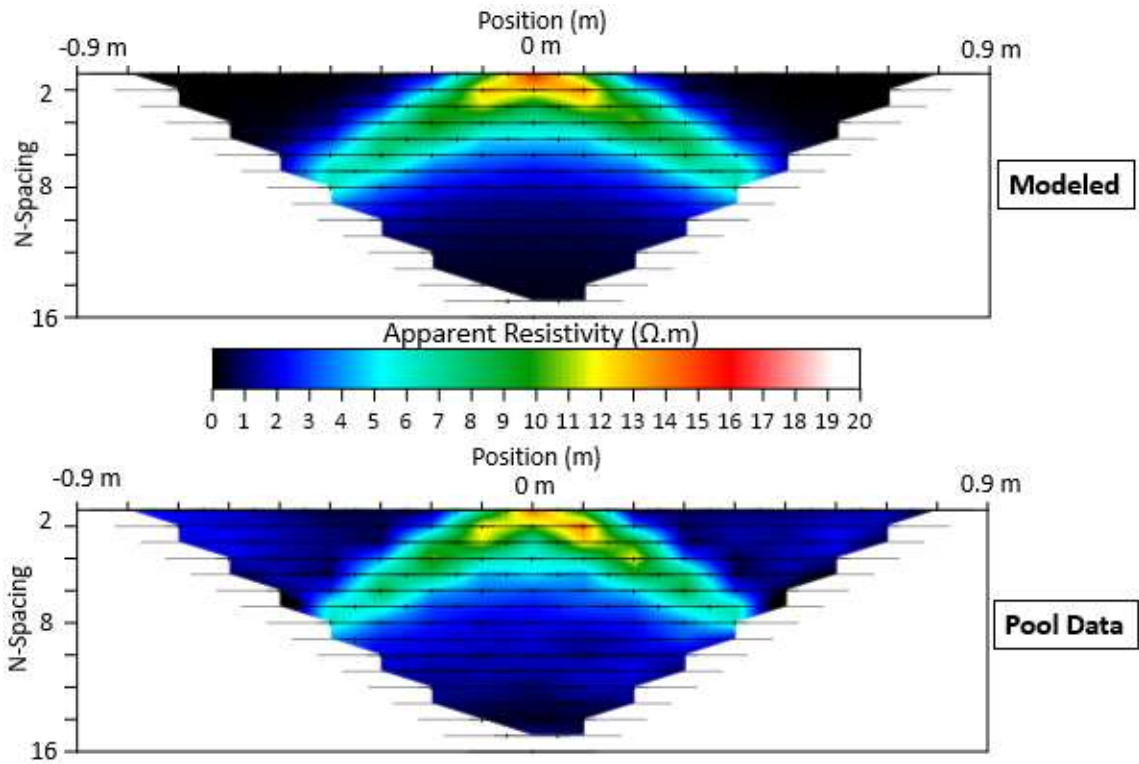


Figure 3.5: Isolated secondary response of the reference casing with both experimental and MoM background removed.

Using,

$$RMS = \frac{1}{n} \sqrt{\sum_{i=1}^n (M - R)^2}, \quad (3.1)$$

where “n” is the number of data points, “M” is the MoM modelled apparent resistivity and “R” is the experimental apparent resistivity, I have calculated a root-mean-square (RMS) misfit between the two secondary responses of 0.091 compared to an RMS misfit including the resistive edge effects of 0.377. Given the similarities in the secondary responses, a significant portion of the 0.091 misfit may be attributed to small differences in the experimental background between the homogeneous pool surveys and the survey including the reference casing.

As a final step to mitigate the resistive boundary effects seen in apparent resistivity pseudo sections using Etot I have modelled the reference casing example with a resistive layer placed at 0.8 m depth to represent the pool bottom.

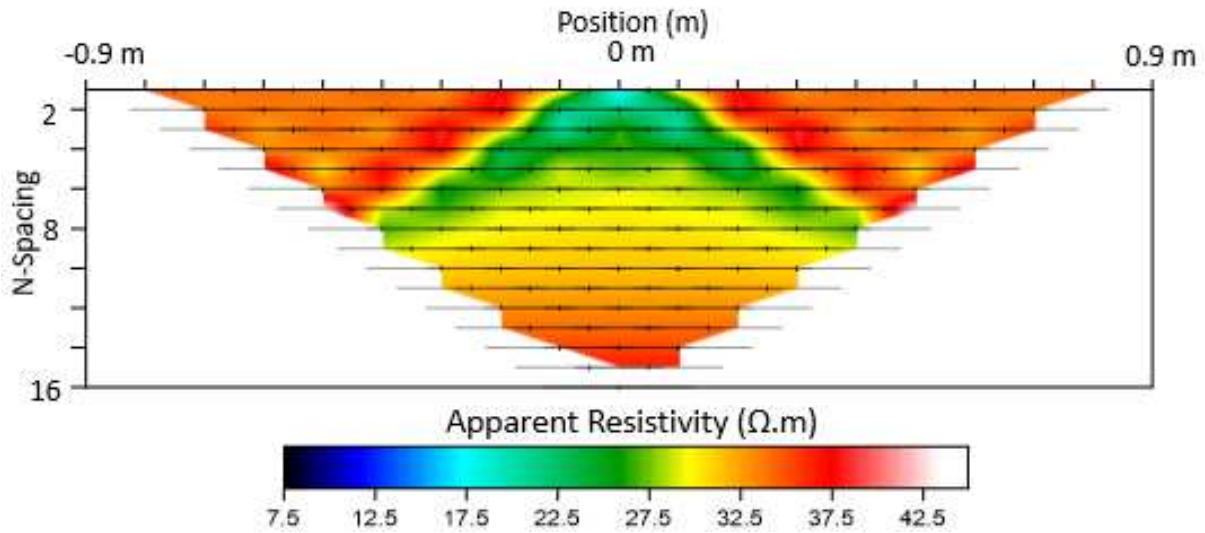


Figure 3.6: MoM modelled reference casing with a horizontal resistive boundary placed at 0.8 m depth.

Interestingly, figure 3.6 shows an increase in apparent resistivity with depth as opposed to the drop in apparent resistivity observed in experimental data and finite-element modelling. The only difference between this scenario and that of the experimental data is the lack of electrically resistive walls. The increase in apparent resistivity with depth can be described through figure 3.7.

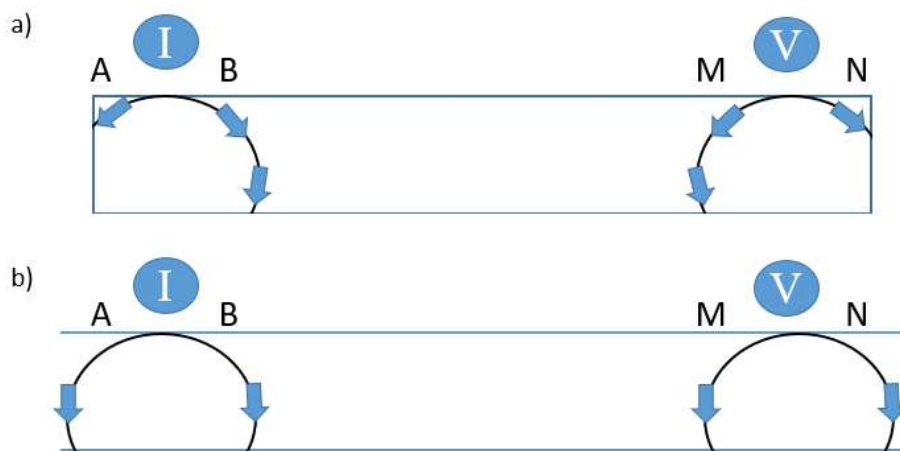


Figure 3.7: Schematic diagram of current flow in the pool environment (a) and in MoM model with lower resistive layer (b).

Within the pool environment (Figure 3.7 (a)) as current is injected near the edges of the pool it is trapped by the resistive walls as well as the resistive pool bottom leading to high current density, and therefore lower apparent resistivities, near the central-bottom zones of the pool. In case (b) of figure 3.7 however current is allowed to flow laterally within the modelling environment leading the resistive lower boundary to be viewed as a simple resistive inclusion in the pseudosection.

3.1.3: An Experimental Study on the Secondary Field with Changing Casing Width

Moving on from this reference casing of intermediate physical dimensions I will now study the effects of a changing casing radius. I begin with a casing of length 0.3048 m, outer radius of 0.01305 m and inner radius of 0.00785 m. This gives a length dimension equal to the first casing study and an outer and inner radius nearly half as large. There is a difference in wall thickness between the reference casing, and this most narrow casing of 1.9 mm. Figure 3.8 shows both modelled and lab-scale data for this smaller diameter casing.

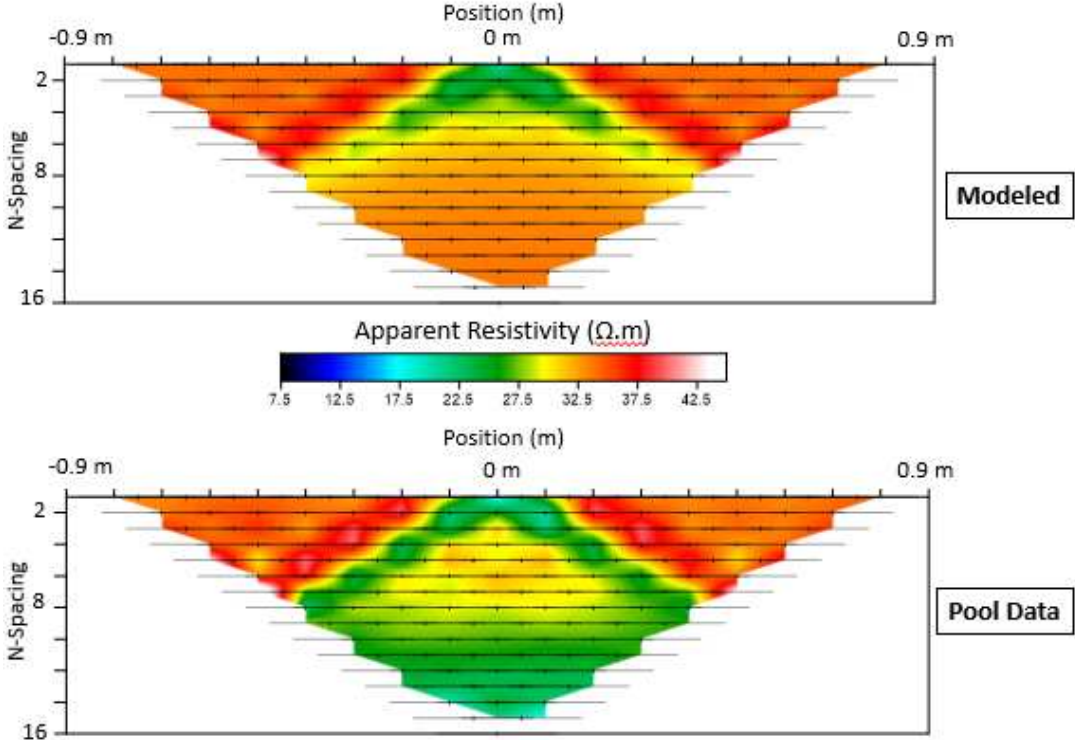


Figure 3.8: Experimental and MoM model apparent resistivity pseudosections of the narrowest casing having an outer radius of 0.01305 m and inner radius of 0.00785 m with equal length to that of our reference casing.

The most immediately obvious trend, which we will witness in all the lab-scale data, is again the drop in apparent resistivity with depth. In the narrowest case it is seen that the largest drops in apparent resistivity extend slightly further than what was observed in the reference case. The MoM model shows the largest drops in apparent resistivity pinch out near data level six. This discrepancy between the experimental data and MoM model is likely due to small differences in depth of suspension between model parameters and experimental setup. The extension of the secondary response to the edges of the pseudosection in the lab-scale data could also be a connection of the zones of highest response from the casing and the drop in apparent resistivity with depth observed from the lower resistive edge of the pool. The magnitude of the drop in apparent resistivity within the secondary response between the lab-scale data and the numerically modelled data shows a higher discrepancy than that observed in the reference case as can be seen in figure 3.9.

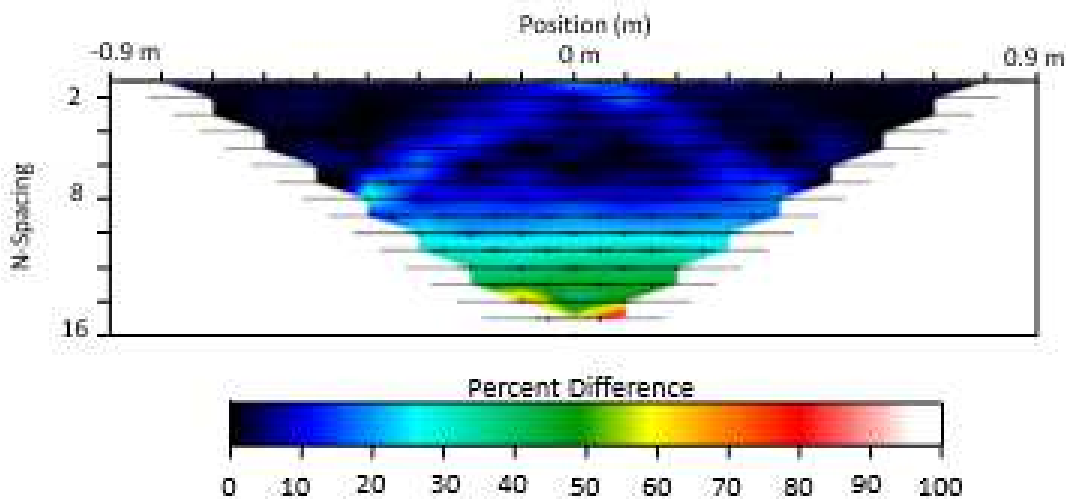


Figure 3.9: Percent difference between the MoM model and experimental data gathered over the narrow casing. There is a slightly higher discrepancy between experimental and MoM model data in this case than observed in figure 3.4.

The largest mismatch occurs from the drop in apparent resistivity with depth beginning at data level 10 at ~30% error and increasing to ~80% at a maximum. There are maximum discrepancies within the zone of secondary response in this case of ~25% occurring along the left-hand side of the pseudosection.

I will now analyze a casing of the same length, 0.3048 m, but an outer and inner radius of 0.0295 m and 0.0264 m respectively making it almost twice the width of the control casing. There is a difference in wall thickness between the widest casing and the reference casing of 0.2 mm.

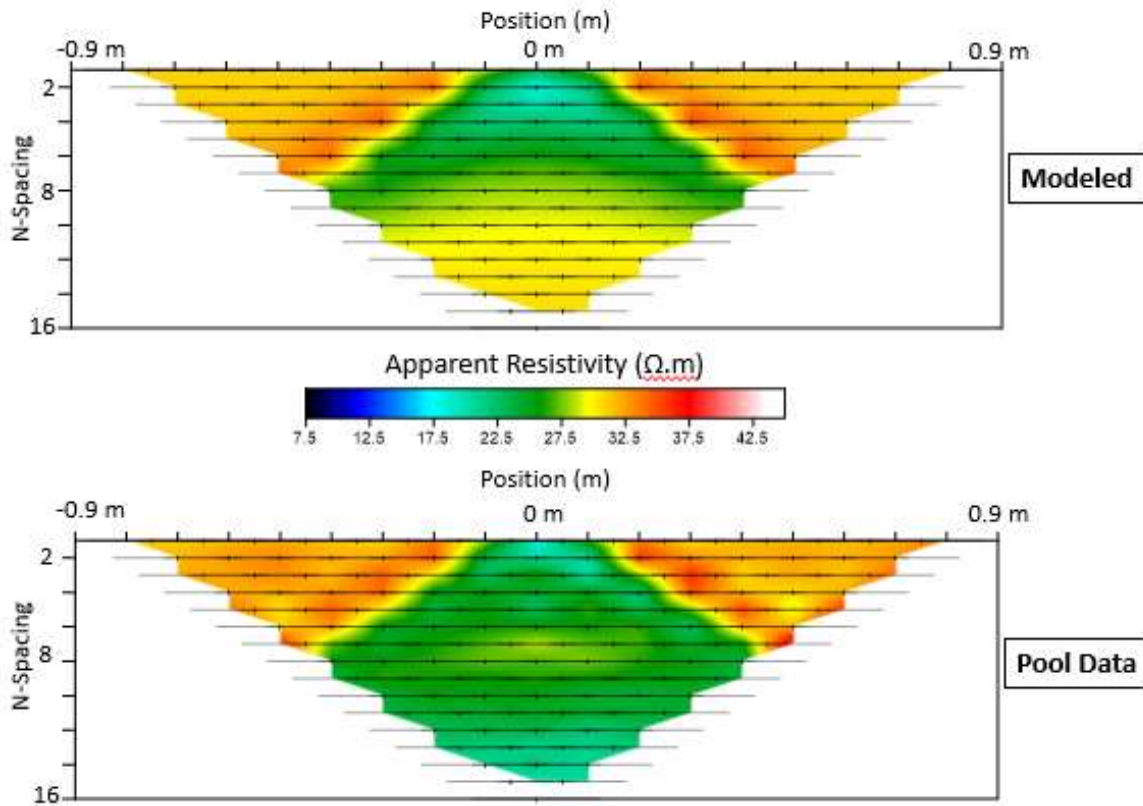


Figure 3.10: Experimental and MoM model apparent resistivity pseudosections of the widest casing having an outer radius of 0.0295 m and inner radius of 0.0264 m with equal length to that of our reference casing. I see a wider secondary response than that observed in the narrow or reference case. Maximum drops in apparent resistivity are only slightly larger but the total area displaying this maximum is greater than in the narrow or references scenario.

There are several things to state qualitatively about both the experimental and numerical model in figure 3.10. The wider casing exhibits no signs of a pinch out along the zone of strongest secondary response in neither the MoM model or experimental data as we saw for the MoM model of the narrow casing. Given the most prominent change in casing properties between these two (as we keep length constant, and wall thickness similar) is the growth of the overall

width of the pipe, we conclude that the lateral thickness of the secondary response seen in the apparent resistivity pseudosections is largely controlled by the width of the casing itself. In the case of a much longer survey array, and a perfect half space without the factor of resistive edge effects the wide casing response for both model and experimental data would likely pinch out eventually as well, however it would be observed only with wider spacing of current injection and potential electrodes. The second important observation from the increase in casing width, is an increased drop in apparent resistivity from the background. In the presence of the narrow casing there is a maximum drop from the background resistivity of 27% whereas we reach nearly 33% from the wide casing. The larger spatial distribution of the widest casing also leads to us not observing a full return to the background apparent resistivity at depth.

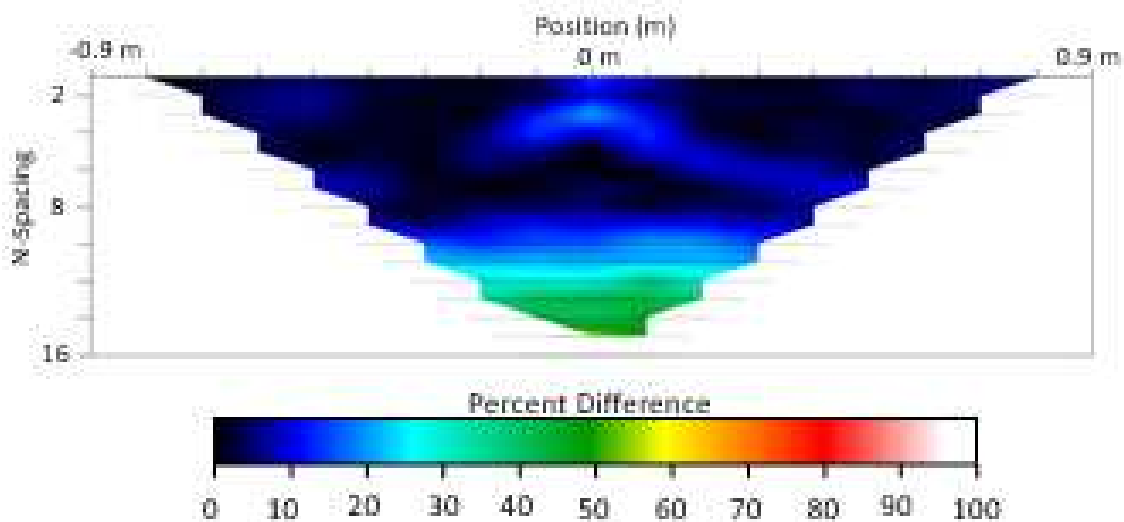


Figure 3.11: Point-by-point percent difference plot between the MoM model and experimental data gathered over the widest casing. There is a maximum percent difference near 15% within the top center region of the plot which fades into a smaller discrepancy along the remaining secondary response nearer to 10%.

Figure 3.11 shows maximum percent differences in the presence of the widest casing of ~15% in the top center of the pseudosection which fade into an average of 10% or less discrepancy throughout the remaining secondary response. Of the three casings discussed so far there is a good match between the MoM model and experimental data. The match deteriorates as I present

further cases, which could likely be an effect of the asymmetry artifact discussed in section 3.1.4 that affects casings of longer and shorter lengths or thin walls more strongly.

3.1.4: The Mystery of an Asymmetric Pant Leg

Before any further analysis of data from the lab scale pool experiment, a phenomenon must be addressed that has strongly affected some datasets, and nearly all others to a lesser extent. Though it is noticeable with a keen eye in nearly every dataset, this rather large artifact was observed while surveying casings exhibiting very thin walls or small total widths. For these cases I would see secondary responses from the casing exclusively on the far side of apparent resistivity pseudosections between electrodes ten and nineteen. In contrast, on the near side, between electrodes one and ten, the section would look as though we were imaging the pool environment free of any electrically conductive casing. After ruling out the possibility of a single electrode having a bad connection to the resistivity instrument, or a short circuit between electrodes taking place (which may both cause a similar effect) it was necessary to explore the details of the experiment in greater detail. All experiments are carried out using a dipole-dipole which itself is asymmetric in nature having both current electrodes A and B next to one another and voltage electrodes M and N adjacent at a given spacing, shown in figure 3.12.

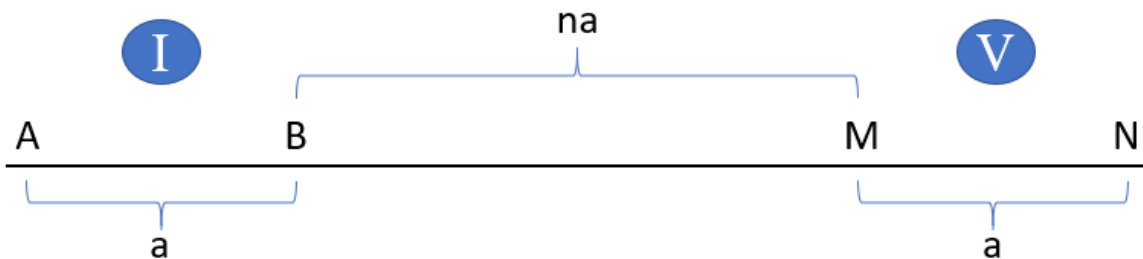


Figure 3.12: Schematic diagram of a dipole-dipole resistivity array. A and B represent current electrodes and M and N represent voltage electrodes.

Given the unique geometry of the dipole-dipole array regardless of which position the current or voltage electrodes are in, the voltage electrodes always lead the current as we step through the different positions and spacings of the survey. Because of this there is stronger secondary response from the casing when your current electrodes, A and B, are near the casing as they are

on the far side of the survey for electrodes ten through nineteen. This means that the same data point in a pseudosection when surveyed in two different ways, one with current electrodes near the casing and the voltage electrodes further away and the second vice versa (figure 3.13), will produce greatly varying apparent resistivity values.

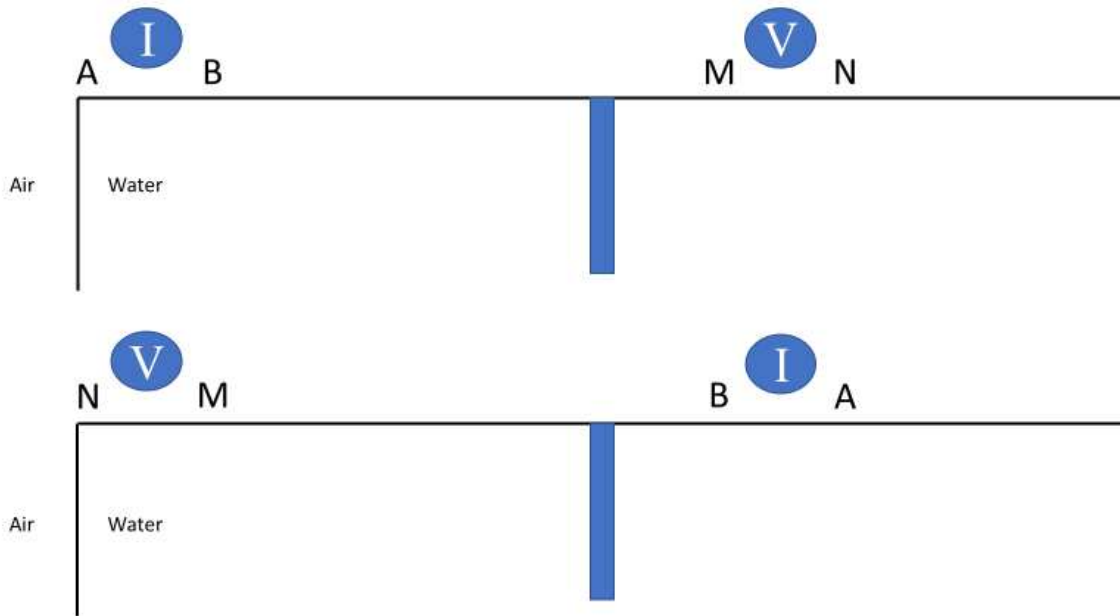


Figure 3.13: Schematic diagram illustrating the simple process used for studying the asymmetry pant-leg effect occurring at the lab-scale. A and B again represent our current electrodes, and M and N are our voltage electrodes. There is a secondary response when the current electrodes are placed near the electrically conductive casing and the voltage electrodes are at a further distance, but in the reverse scenario we often observe just the background resistivity.

So much so, in fact, that many tests show a strong secondary response in one position, but a reading near the background resistivity at the other. Table 3.1 shows the results from swapping current and voltage positions. It is immediately obvious that when current electrodes are near the electrically conductive casing that I will see much lower observed apparent resistivity.

Table 3.1: The results from tests to study the asymmetry artifact show vastly different observed apparent resistivities depending on the placement of our current electrodes in relation to the electrically conductive casing being surveyed.

A	B	M	N	ρ_a
8	9	10	11	29 $\Omega.m$
11	10	9	8	22 $\Omega.m$
9	10	13	14	14 $\Omega.m$
14	13	10	9	32 $\Omega.m$
9	10	14	15	9 $\Omega.m$
15	14	10	9	36 $\Omega.m$

This general effect will lead to the observed artifact of asymmetry potentially to the point of a perfectly one-sided secondary response at times. The MoM calculations depend on the incident E_{tx} field at each segment to calculate its current which is then used to find the secondary field, E_s . The high precision of this method allows casing responses to be predicted even if the currents on the casings are small. In the pool experiment the DC resistivity instrument has a maximum current that it can output which leads to lower current within the casing at far AB electrode pair distances than are observed when AB are nearer. It could also be due to the DC resistivity instrument not being sensitive enough to smaller variations in potential that occur when current electrodes are far from the casing as it was found that MoM calculations at the electrode pairs listed in table 3.1 found drops in apparent resistivity indicative of a secondary response. It was also found that by reversing the electrode positions, so that electrode one is in the position that electrode nineteen was formerly in and so forth for all other electrodes, that the secondary response produced again showed only on the right-hand side of the pseudosection.

3.1.5: A Study on the Secondary Field with Changing Casing Length

I will now discuss the effects of length on secondary response as observed in both experimental and MoM data. First, I will study the shortest casing surveyed of length 0.254 m, outer radius 0.0162 m, and inner radius 0.01333 m with a background resistivity now of 31 $\Omega.m$. This means a difference between wall thickness of the references casing and this shortest casing

of 0.43 mm. The variation in background resistivity is due to environmental changes in the outdoor area where the experiment is located between times of survey completion.

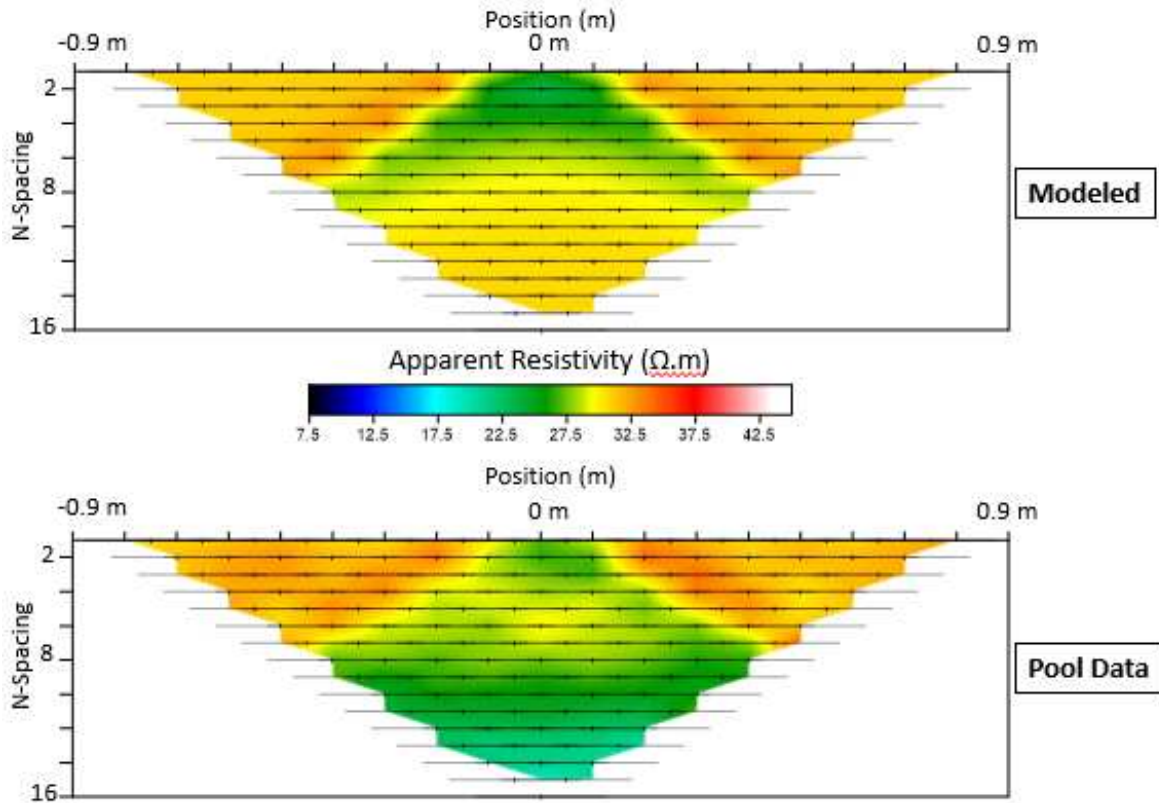


Figure 3.14: Experimental and MoM model apparent resistivity pseudosections of the shortest casing displaying a length of 0.254 m with outer and inner radii near equal to that of the reference casing. Unlike in the presence of the narrow casing we see a secondary response as wide as that of the reference, however the center of the response extends to a shallower data level and drops in apparent resistivity are slightly lower than that observed of the control.

As could be inferred from the theory of chapter two there is a relatively weak drop in apparent resistivity produced from this casing. It can be seen in figure 3.14 that the secondary response is rather weak throughout the entire affected area which can be attributed to the large effect of length on secondary fields observed in chapter 2. Drops in apparent resistivity along the zone of strongest response are nearly equal between experimental data and MoM model. Figure 3.15 shows a point-by-point percent difference plot between the two.

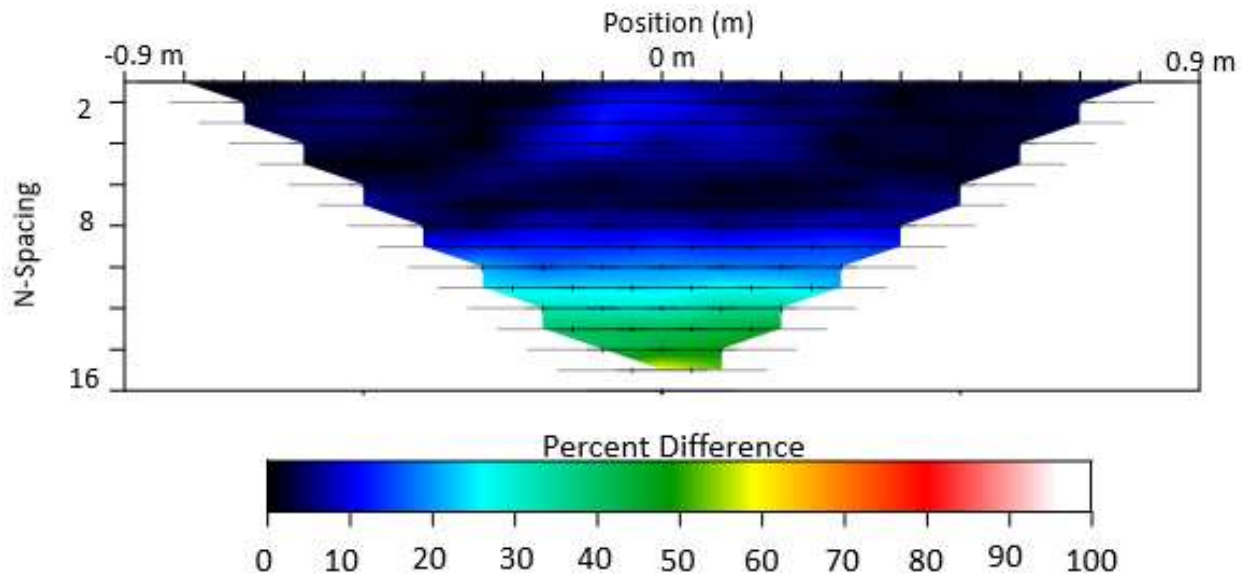


Figure 3.15: Point-by-point percent difference plot between our MoM model and experimental data gathered over a 0.254 m casing. There is a good fit between MoM model and experimental data with just below 10% discrepancy near the top center of the plot.

Percent difference plots show again roughly 50% difference at depth from the resistive edge effects, but differences barely reach 10% within the secondary response zones.

I will now discuss data gathered using a longer casing of length 0.6096 m, with outer and inner radii nearly the same as the control casing and the above discussed short casing at 0.016075 m and 0.0135 m respectively. There is again a slight difference in wall thickness between this and our reference casing of 0.73 mm due to manufacturing differences in casings available at Home Depot. The long casing (Figure 3.16) shows an even stronger asymmetric response than does the short example, with a maximum drop in the secondary response zone to $\sim 18 \Omega\text{m}$. The long casing gives a much more pronounced and deeper response than that of the shorter casing, filling the entire triangular zone beneath the top of the casing with a drop in apparent resistivity from the background.

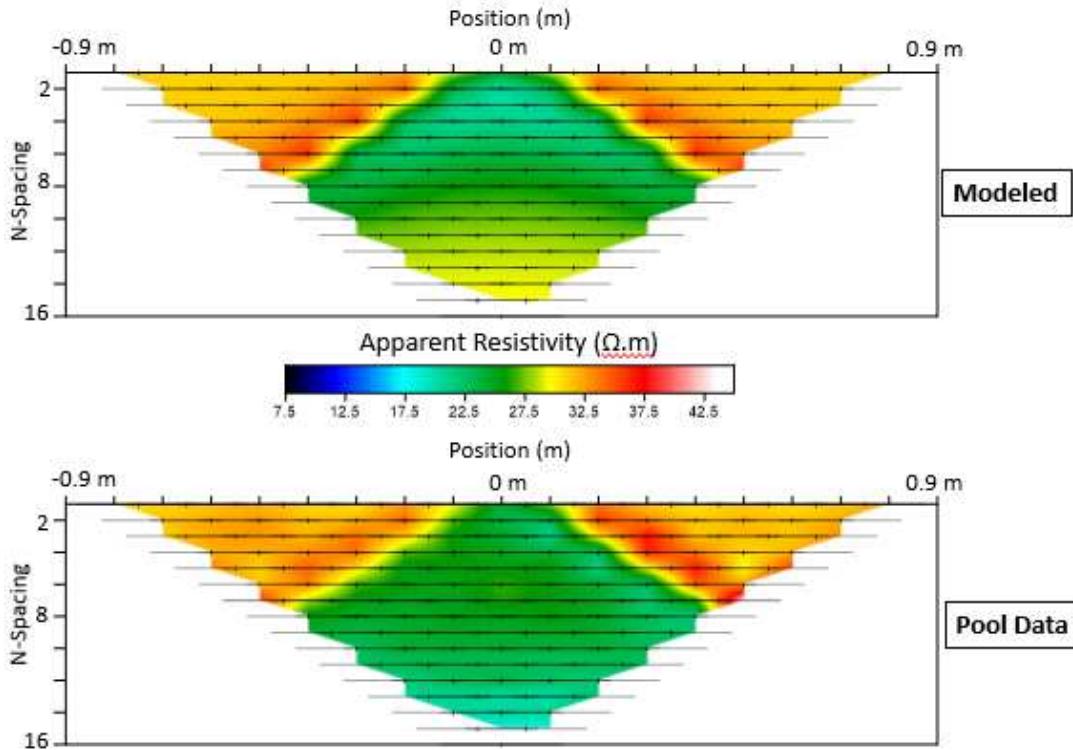


Figure 3.16: Experimental and MoM model apparent resistivity pseudosections of the longest casing displaying a length of 0.6096 m with outer and inner radii near equal to that of the reference casing. Along with a slightly deeper center of the secondary response, in the experimental data reaching so deep it connects with the resistive edge effects, we also see a slightly higher drop in apparent resistivity than that seen from our reference casing. A trend we are viewing with the extremes of these dimensional variables.

Percent difference plotted in figure 3.17 for the long casing looks very similar to that observed for the short casing. Except for the left-hand side of the difference plot where there is a ~20-25% difference due to the asymmetry artifact there is ~10% difference or less in the remaining zones of secondary response. Again, differences exceed ~50% due to our resistive lower boundary of the pool. To view things in a more quantitative sense it is seen that there is difference in length between the short and long casings of 0.3556 m which has produced a drop from the background of 36% and 20% from the background resistivities in the long case and short case respectively. This is accompanied by the added effects of the much centrally deeper secondary response that we see from the longer casing.

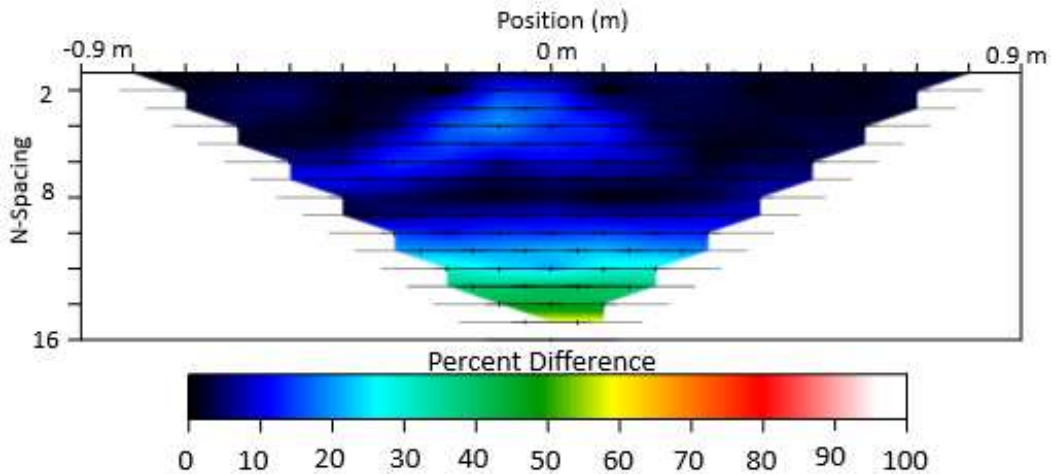


Figure 3.17: Point-by-point percent difference between the MoM model and experimental data gathered over the longest casing. The largest discrepancy of ~15% lies along the left leg of the secondary response due to the asymmetry artifact.

Having now seen examples of casings both small and large in diameter, and short and long in length, there is a direct correlation between those physical properties in the casings and the same properties of the secondary response viewed in an apparent resistivity pseudosection. Casings with very small diameters produce secondary responses in pseudosections that pinch out with depth at shorter distances from the casing, whereas casings of large diameter have thick secondary responses that extend throughout all our experimental data levels. Similar relationships can be observed for variable casing length. The lower apparent resistivity area directly beneath the center of the secondary response ($x = 0.0$ m) extends to a much greater depth in the case of the longer casing than it does with casings of a shorter length. These effects on the shapes of the secondary response also extend to the magnitude of the drop in apparent resistivity as we showed above. Longer and wider casings correlate to slightly larger drops in apparent resistivity than thinner or shorter ones.

3.1.6: A Study on the Secondary Field with Changing Wall Thickness

As was expressed in the corresponding sections of chapter 2 regarding wall thickness and metal volume the question of how secondary responses change with a given increase in electrically conductive volume of the casing is very important to address. The lab-scale pool experiment gave an excellent opportunity to test this. Within this section I will show data from

two aluminum casings, both with lengths of 0.6096 m and outer radii of 0.0065 m. One casing is solid and the other is hollow with an inner radius of 0.0045 m.

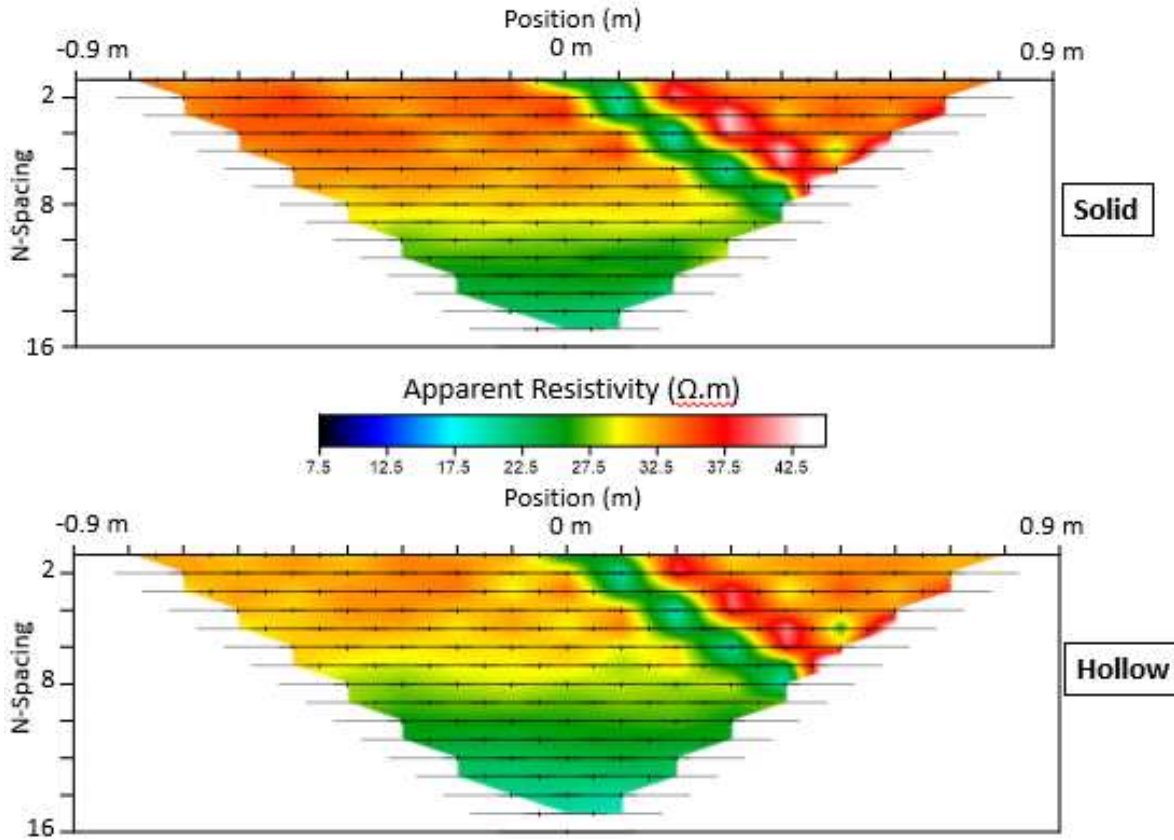


Figure 3.18: Experimental apparent resistivity pseudosections comparing responses from solid and hollow 0.6096 m length aluminum casings with equal outer radii. There is little difference between the two pseudosections with this view.

These aluminum casings had an electrical conductivity of 3.5×10^7 . The small outer radii of the casings led to another example of “perfect asymmetry” from the effect described in section 3.1.3. Qualitatively, there is little difference between the hollow and solid casings. To gain a better quantitative perspective it is useful to subtract the apparent resistivities of the pool in the case of a perfect homogeneous background (data from figure 3.2) from the hollow and solid casing data to view strictly the responses created from the casings free of any primary background.

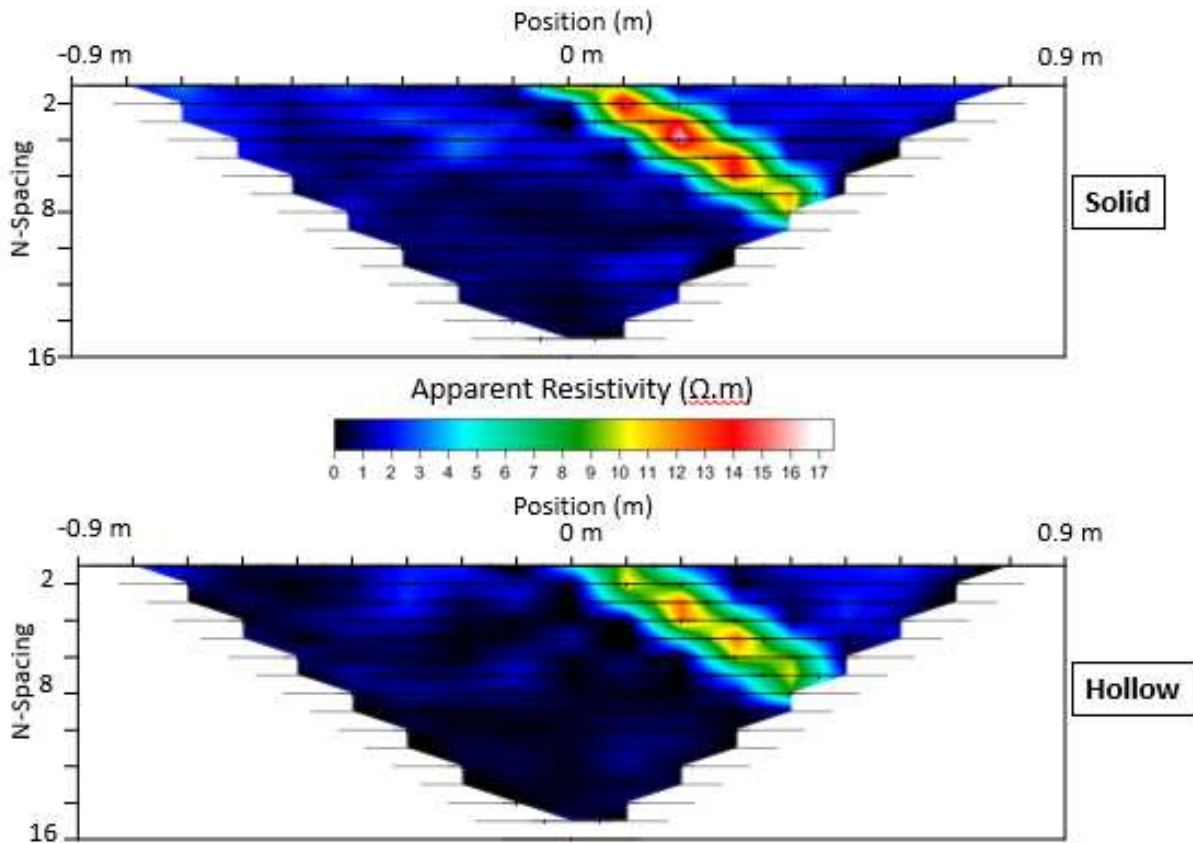


Figure 3.19: Experimental apparent resistivity pseudosections comparing secondary responses from a solid and hollow 0.6096 m length aluminum casing with equal outer radii. Here I view apparent resistivity pseudosections with the primary fields backed out showing only the secondary response. It is seen that a larger drop in apparent resistivity is present in the case of the solid casing.

Figure 3.19 allows a view of strictly the secondary response of the casing free of the primary background. With this new view on the data, I am not only seeing a wider response within the solid data, but also a more significant drop in apparent resistivity. The solid data displays drops from the background of more than 15 Ωm or 45% through most of its response. There are on average differences from the background of closer to 10 Ωm or 29% for the hollow case.

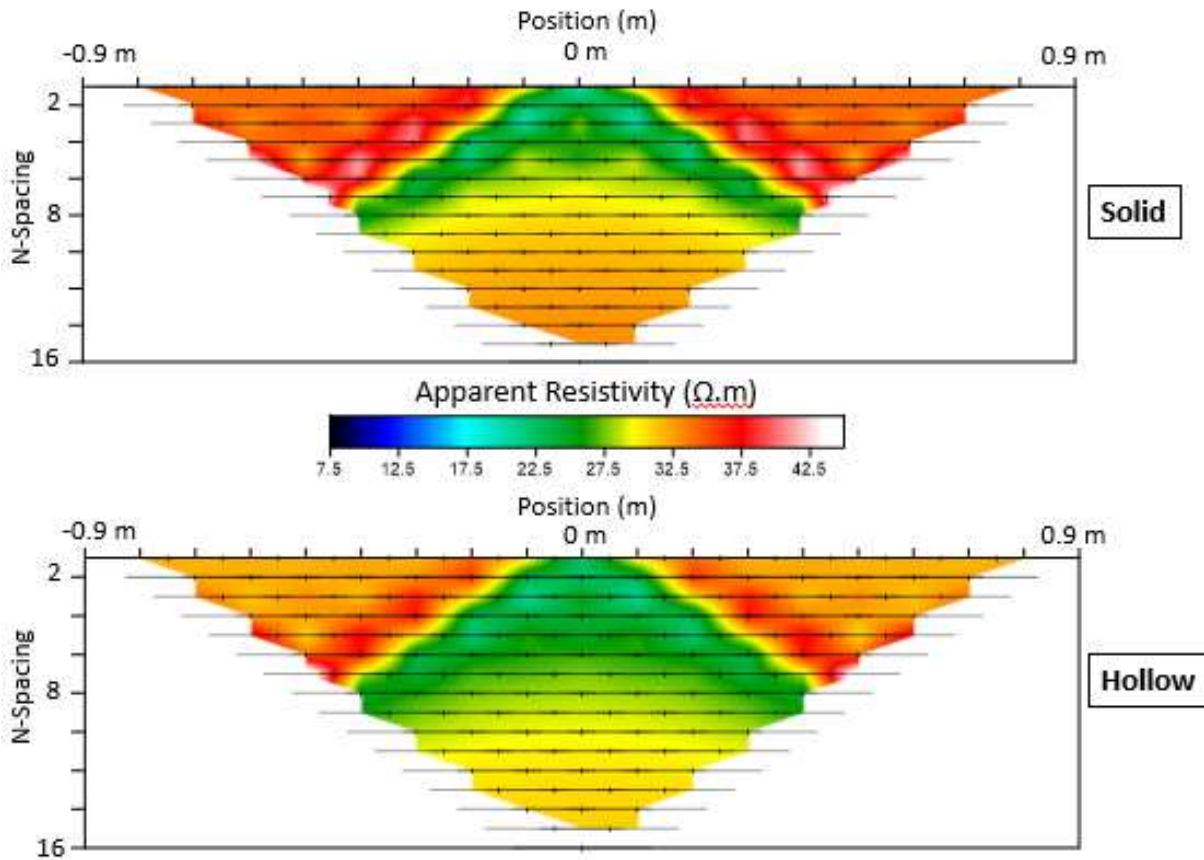


Figure 3.20: MoM model comparison between the solid and hollow aluminum casings. There is a similar trend of a stronger response being produced from the solid casing

Similar trends are observed in the MoM secondary field plots, although weaker drops in apparent resistivity are seen in both sections. Figure 3.19, 3.20 and 3.21 lead to the conclusion that though width and length of the casing affect almost exclusively the shape of our secondary response, changing the wall thickness of a casing and increasing total volume of metal produces an increase in magnitude of our response. MoM models and their associated percent difference plots show a good match on the right-hand side of both models where the asymmetry artifact is not present. Discrepancies are slightly better in the solid case, but both models fit within a 30% margin of error.

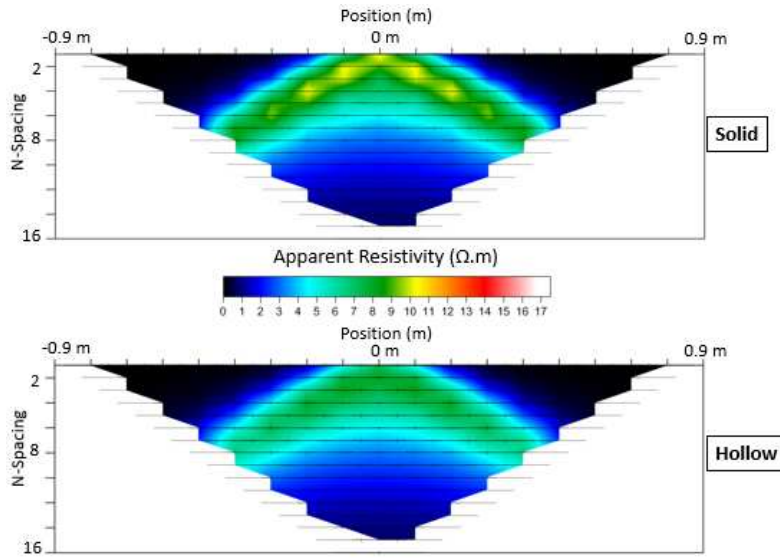


Figure 3.21: MoM apparent resistivity pseudosections comparing secondary responses from a solid and hollow 0.6096 m length aluminum casing with equal outer radii. Here I view apparent resistivity pseudosections with the primary fields backed out showing only the secondary response. It is seen that a larger drop in apparent resistivity is present in the case of the solid casing.

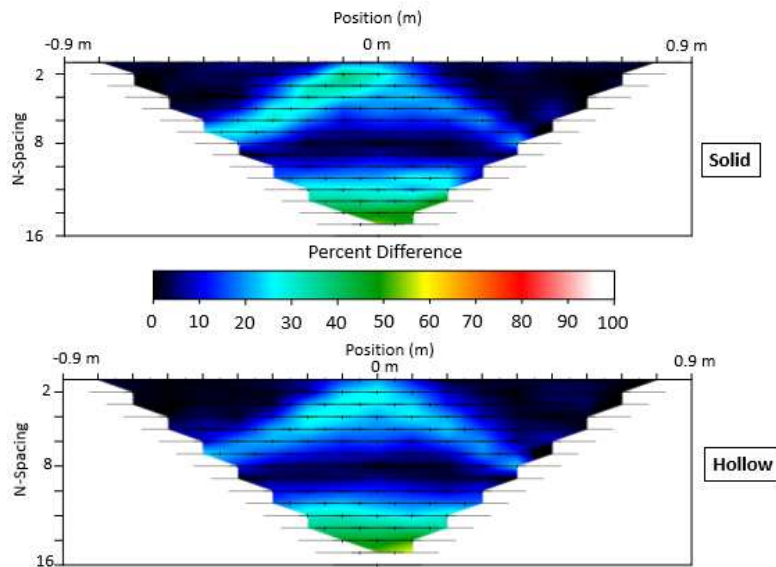


Figure 3.22: Percent difference plot displaying discrepancies between MoM models and experimental data. Both display expected high discrepancies on the left-hand side due to the asymmetry artifact. The right-hand side of both plots display a misfit of ~25%.

3.1.7: A Study on the Secondary Field with Changing Casing Material

After having explored the effects of changing spatial properties of the casing on apparent resistivity pseudosections I will now observe a casing with dimensions near equal to that of the control casing but now made of brass, a material roughly half an order of magnitude more electrically conductive than the reference casing's steel. The brass casing exhibits a length of 0.3048 m, an outer radius of 0.0156, and an inner radius of 0.01505 m with an electrical conductivity of $2 * 10^7$ S/m. This is slightly less conductive than the aluminum used for the cross-sectional area studies, but still significantly more conductive than the steel of the reference casing. There is a difference in wall thickness between the brass and the reference casing of 2.75 mm.

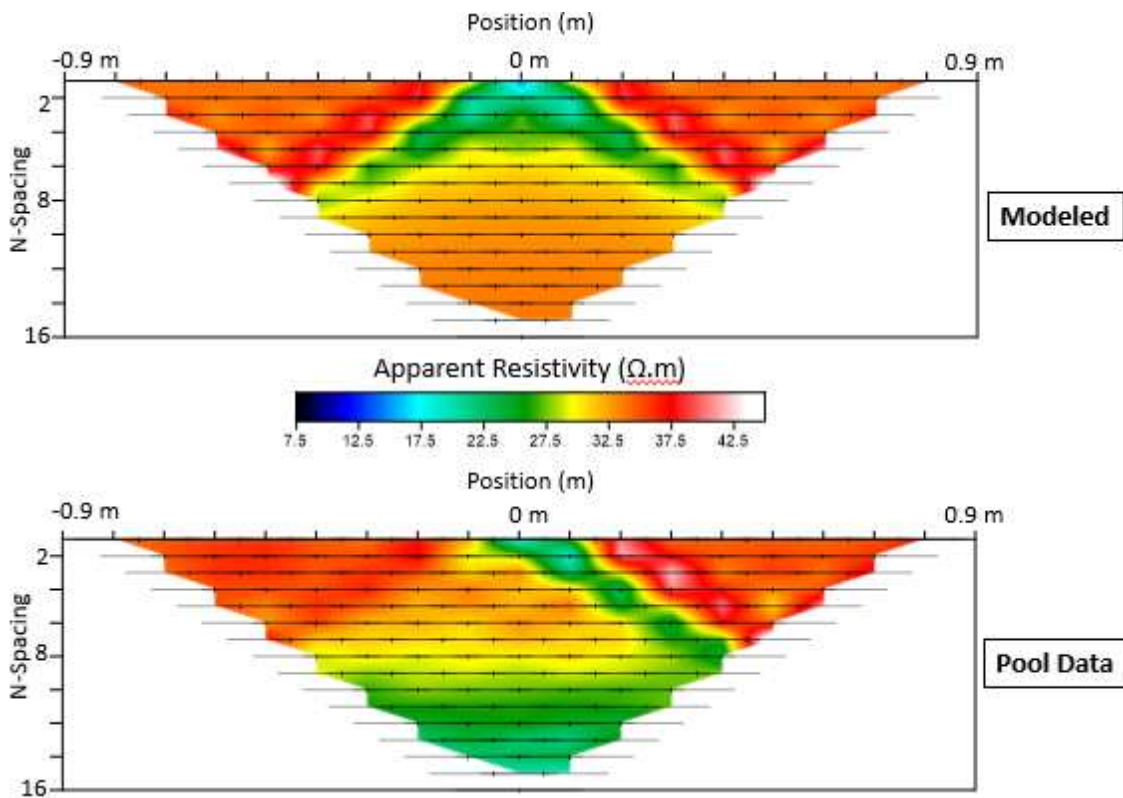


Figure 3.23: Experimental and MoM model apparent resistivity pseudosections of the brass casing displaying a length and outer radius equal to that of the control casing and a slightly thinner wall. I find that the more electrically conductive casing material creates a significantly stronger drop in apparent resistivity within the secondary response.

The largest drops in apparent resistivity produced from our casing are completely absent on the left-hand side of figure 3.23. Comparing the brass casing to the reference, the difference made by the increase of casing conductivity is clear. In the control casing there is a drop in apparent resistivity along the zone of secondary response of ~20% from the background resistivity, in the scenario of the brass casing however there is a drop from a background of 34 Ωm to as low as 18 Ωm in some locations for a total decrease in apparent resistivity of ~47%.

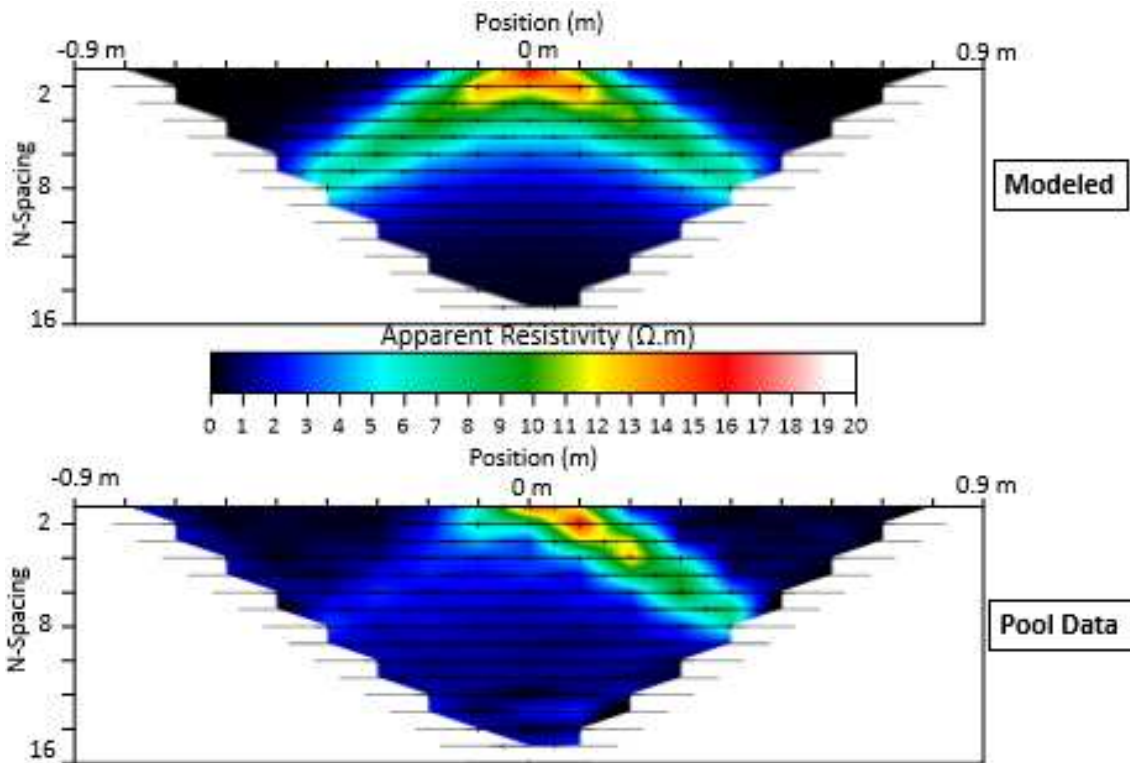


Figure 3.24: Experimental and MoM modelled apparent resistivity pseudosections showing isolated secondary responses from the brass casing studied. It is seen there is a slightly larger drop in apparent resistivity, ~2-3 Ωm more, than observed from the reference casing made of steel.

The isolated secondary field response shown in figure 3.24 confirms this observation showing a maximum drop in apparent resistivity from the background ~2-3 Ωm stronger than that observed in the reference case. This indicates that though length and width of our casing may control the shape of our response, the electrical conductivity of the material composing the casing, as the

total metal volume, controls the magnitude of response. An RMS misfit between the secondary responses of the MoM and experimental data was calculated to be 0.191. Similar to that observed in the reference case some of this misfit is due to discrepancies between the background and the brass casing surveys, but the strongest contribution to the misfit probably comes from the asymmetry artifact affecting the entire left-hand side of the pool data.

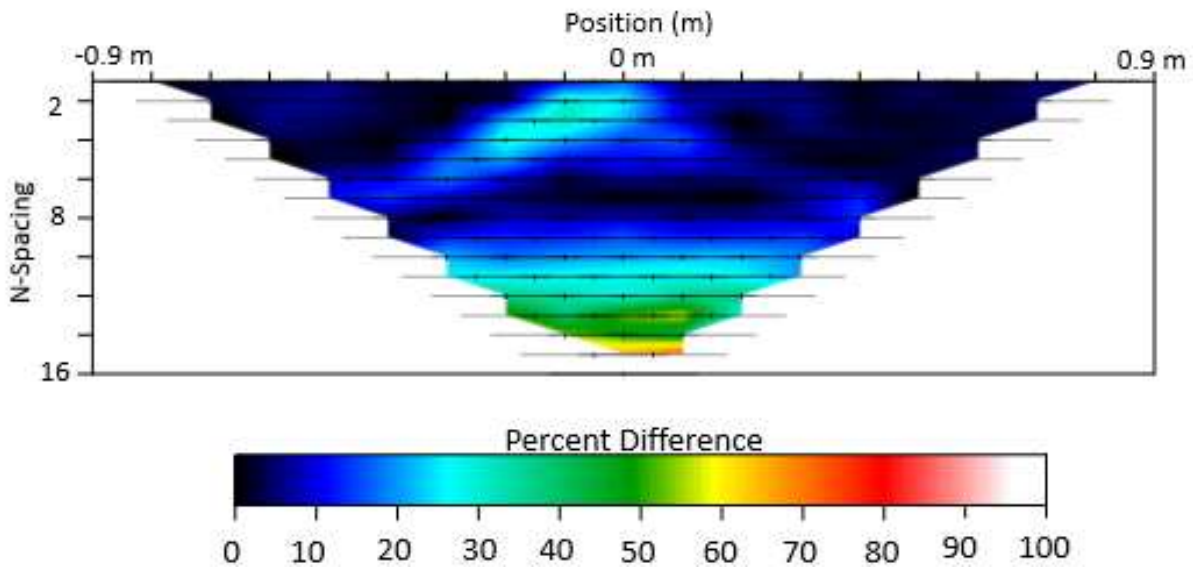


Figure 3.25: A point-by-point percent difference showing discrepancies between the MoM model and experimental data of the brass casing. On the right-hand side of the plot less affected by the asymmetry artifact we see maximums of ~10% misfit.

As would be expected after a simple visual inspection of the experimental data and the numerical model, the largest percent difference between the two datasets occurs within the left-hand side (Figure 3.25) where the secondary response is absent in the experimental data of figure 3.24. On the right-hand side there is a maximum discrepancy of ~10%.

3.1.8: On the Effects of Varying Casing Positioning

In the case of marine CSEM surveys we will rarely observe a perfectly vertical casing. It is not only necessary to survey casings with a variety of dimensional and material properties but also those varying in their orientation.

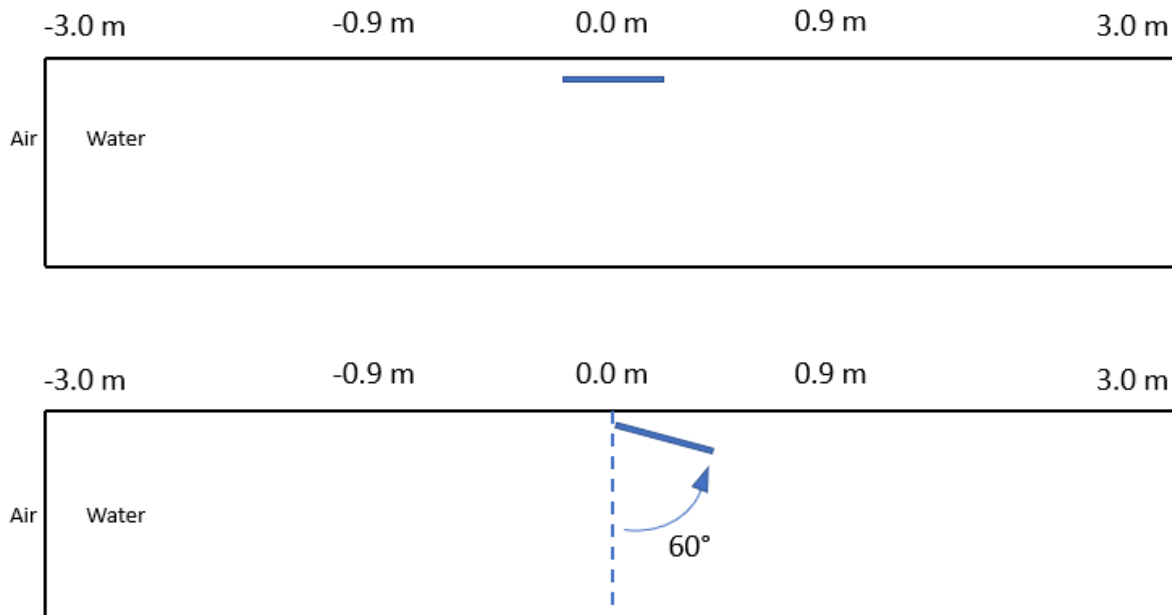


Figure 3.26: Schematic diagram showing orientations of the horizontal and tilted casings. Both cases make use of our control casing of length 0.3048 m, outer radius 0.0164 m and inner radius 0.0131 m.

Within this section I will study our reference casing with a length of 0.3048 m, outer radius of 0.0164 m and inner radius 0.0131 m in a horizontal position with the electrode array inline above it, and in a position at a 60° angle from the vertical (Figure 3.26).

I begin with the casing suspended horizontally inline beneath the nineteen electrodes. Its total length of 0.3048 m is centered beneath electrode ten and it extends by 0.1524 m in either direction from the center. Figure 3.27 shows apparent resistivity data both gathered experimentally and modelled through the MoM approach. The horizontal casing (Figure 3.27) exhibit characteristically larger areas of maximum drops in apparent resistivity from other casings surveyed so far. There are maximum drops in apparent resistivity of $\sim 42\%$ extending throughout the entire range of the horizontal response.

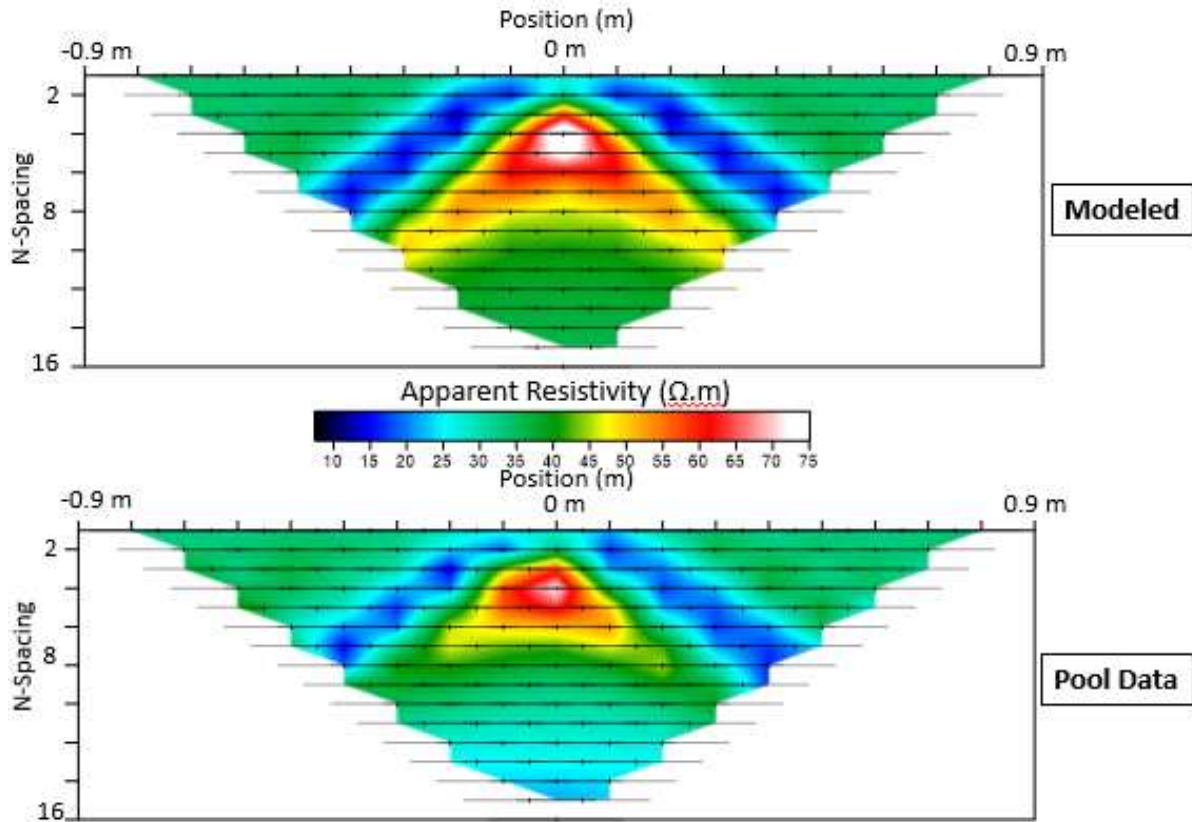


Figure 3.27: Experimental and MoM model apparent resistivity pseudosections of the control casing in a horizontal orientation. This positioning leads to a larger drop in apparent resistivity along the legs of the secondary response and a zone of high apparent resistivity at a slightly lower data level due to the low current density in this zone.

There also is a zone in which resistivity is strongly increased above the background level beneath this large drop. This is due to the nature of the inline survey over the horizontal casing. Much of the injected current is channeled directly into the casing and then laterally towards the lower data levels leaving this central zone with a very low current density and therefore very high apparent resistivity. The point by point difference plot (Figure 3.28) shows slightly higher values than have been seen in the vertical cases due to the intricacies of the horizontal orientation.

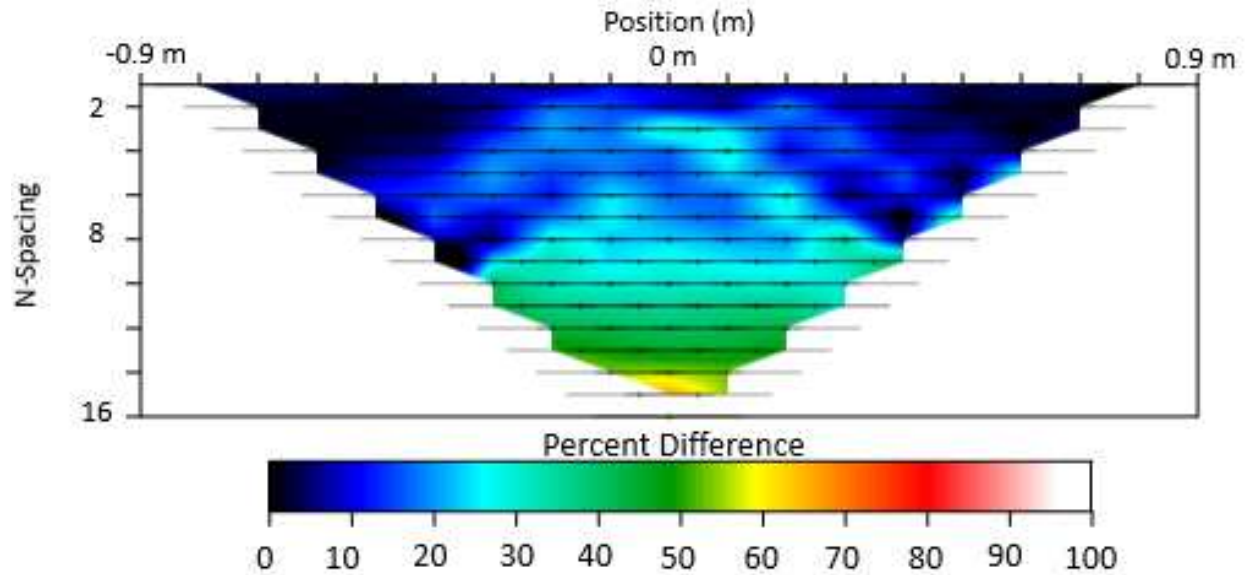


Figure 3.28: Point-by-point percent difference showing discrepancies between the MoM model and experimental data of the control casing in a horizontal orientation. In the zones of the plot that contain the drop in apparent resistivity there is a 10-15% drop in apparent resistivity. In the low-current-density zone, there is a slightly higher discrepancy reaching 30% difference. This is due to the sensitivity of the survey to slight variations along the y-axis regarding how in-line the casing is with the above electrodes.

The inner zone of very high apparent resistivities extends to the deepest data levels of the numeric model, meaning it exists in an area corresponding to the drop in apparent resistivity with data level we see from the resistive edge effects of the pool. This leads to a diagonal stripe upwards on the right-hand side of our pseudosection where we have a mismatch of ~25%. Small variations in the Y-plane regarding the orientation of the casing which are also hard to constrain can also produce larger than expected effects.

I will now discuss the tilted orientation. The casing has its uppermost end centered beneath electrode ten and then extends in the positive X direction diagonally at a 30° angle from the electrode array (see Figure 3.26). The tilted geometry displays itself as an interesting mixture between those of the strictly vertical and strictly horizontal casing (Figure 3.29).

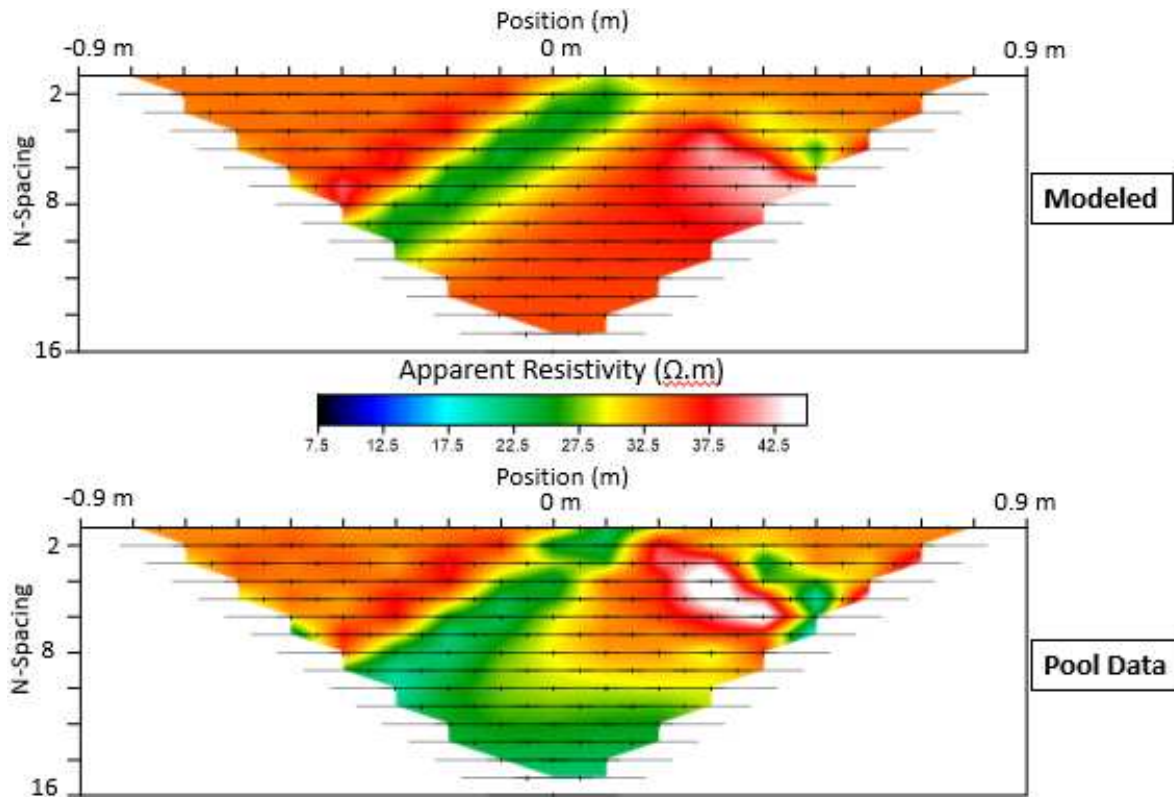


Figure 3.29: Experimental and MoM model apparent resistivity pseudosections of the control casing in a tilted orientation. Like the horizontal orientation, a tilted casing positioning leads to a larger drop in apparent resistivity along the leg of the secondary response and a high apparent resistivity zone beneath this leg due to the low current density in this zone.

For the first time we see a stronger drop in apparent resistivity in the pool data than that modelled by MoM. This is likely due to spatial positioning of the casing not matching perfectly with MoM parameters as dimensional complexities in the tilted case are hard to constrain and small variations in depth of suspension of the casing can strongly affect secondary response. There are drops in apparent resistivity at a maximum of 42%. We also observe a similar current channeling effect to what we witness in a strictly horizontal casing. As current is channeled diagonally along the casing length a low current density pocket is left beneath the casing leading to high apparent resistivities similar to those seen in the horizontal scenario, but offset laterally towards the bottom end of the casing.

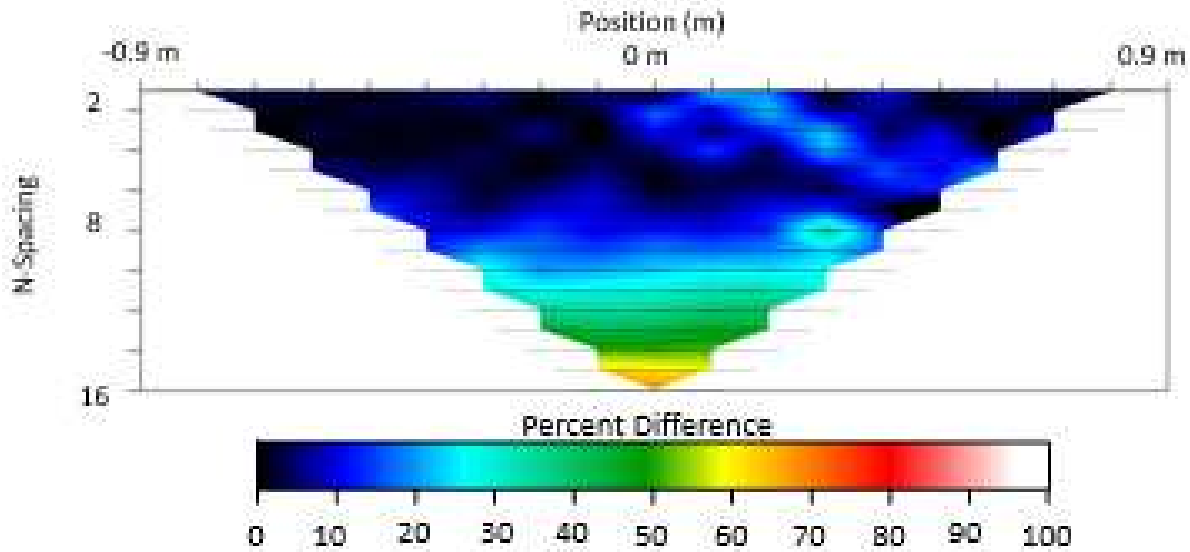


Figure 3.30: A point-by-point percent difference plot showing discrepancies between the MoM model and experimental data of the control casing in a tilted orientation. Again, there are large similarities between the discrepancies in the tilted and horizontal case. With the highest percent differences occurring in the low current density area where we see values approaching 20% difference. The slightly larger misfit in the tilted orientation as compared to strictly vertical casings is again due to the sensitivity of the survey to slight movement of the casing while collecting experimental data.

Though the pool provides a controlled environment regarding allowing certainty with dimensions of the casings, and electrical conductivity measurements of the materials they are made of, these complex orientations present complexities that are difficult to setup up perfectly in an experiment. The larger drop in apparent resistivity observed within the numeric model is also an effect to some extent of the asymmetry artifact witnessed in many of the vertical casings. Showing a maximum percent difference in this zone of ~50%.

3.1.9: On Multiple Adjacent Casings

In a similar vein as the previous section it is also very rare that we would see a single casing by itself within a CSEM survey. To better understand the effects of multiple casings near one another I have conducted several experiments in the pool environment to observe if the effects from adjacent casings interact constructively, destructively or ignore one another entirely and simply overlap. I will again make use of the control casing with a length of 0.3048 m, and outer and inner radius of 0.0164 m and 0.0131 m respectively. I will show data of two control

casings placed vertically first near one another, then further apart, and observe the effects of a vertical casing suspended adjacent to both a horizontal and tilted casing.

I begin with two vertical reference casings suspended inline beneath electrodes seven and thirteen. Both casings are equal in dimensional and material properties. This dataset (Figure 3.31) presents an interesting case study, as the two vertical casings are near enough to one another to generate significant interaction between the two. This helps answer the questions of how adjacent casings will interfere with one another's secondary response.

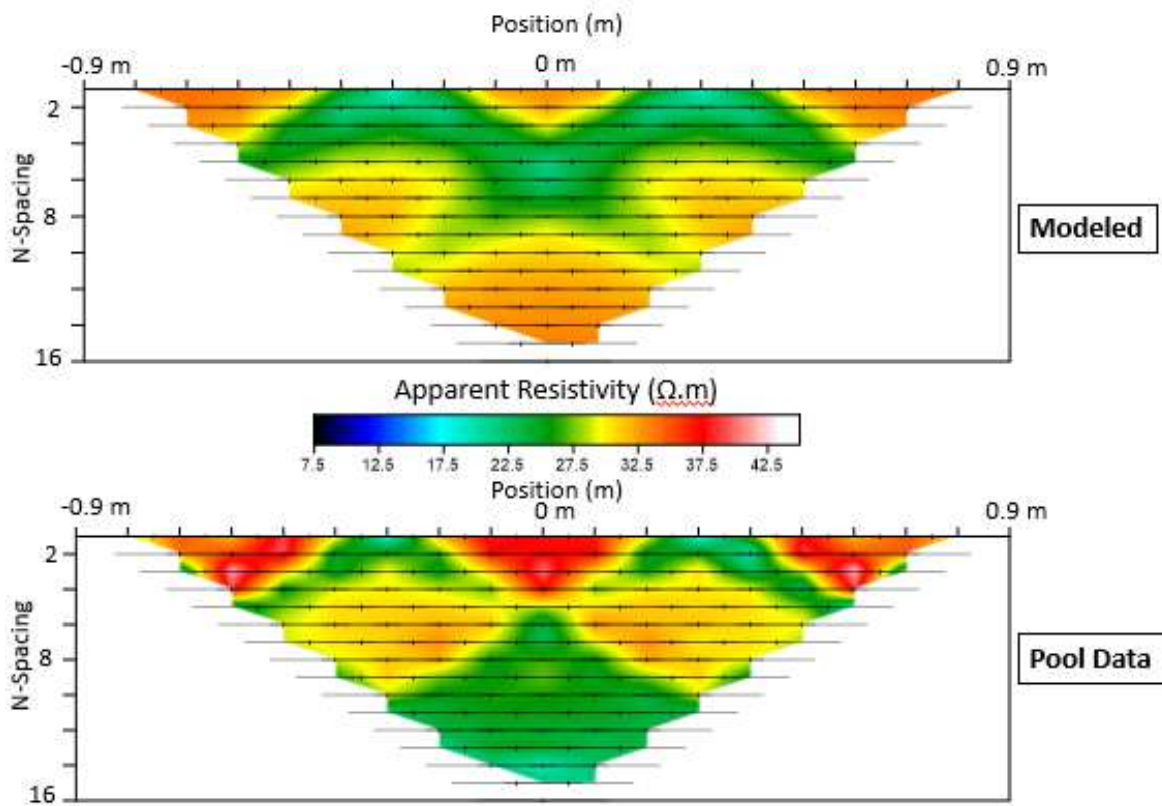


Figure 3.31: Experimental and MoM model apparent resistivity pseudosections of two vertical reference casings positioned beneath electrodes seven and thirteen. There is a combination of the two secondary responses at data level seven creating a third drop in apparent resistivity comparable to the maximum drop seen near the surface beneath each casing.

To begin the analysis, the individual responses themselves agree with that of the reference casing suspended by itself in both shape of response and magnitude of apparent resistivity drop. We

observe a decrease in apparent resistivity near the surface to $\sim 21 \Omega\text{m}$ as would be expected from our prior studies on this casing. However, the two secondary responses begin to combine with one another at data level seven producing a third zone with drops in apparent resistivity from the background of $34 \Omega\text{m}$ to $22.5 \Omega\text{m}$ similar to that seen near the surface.

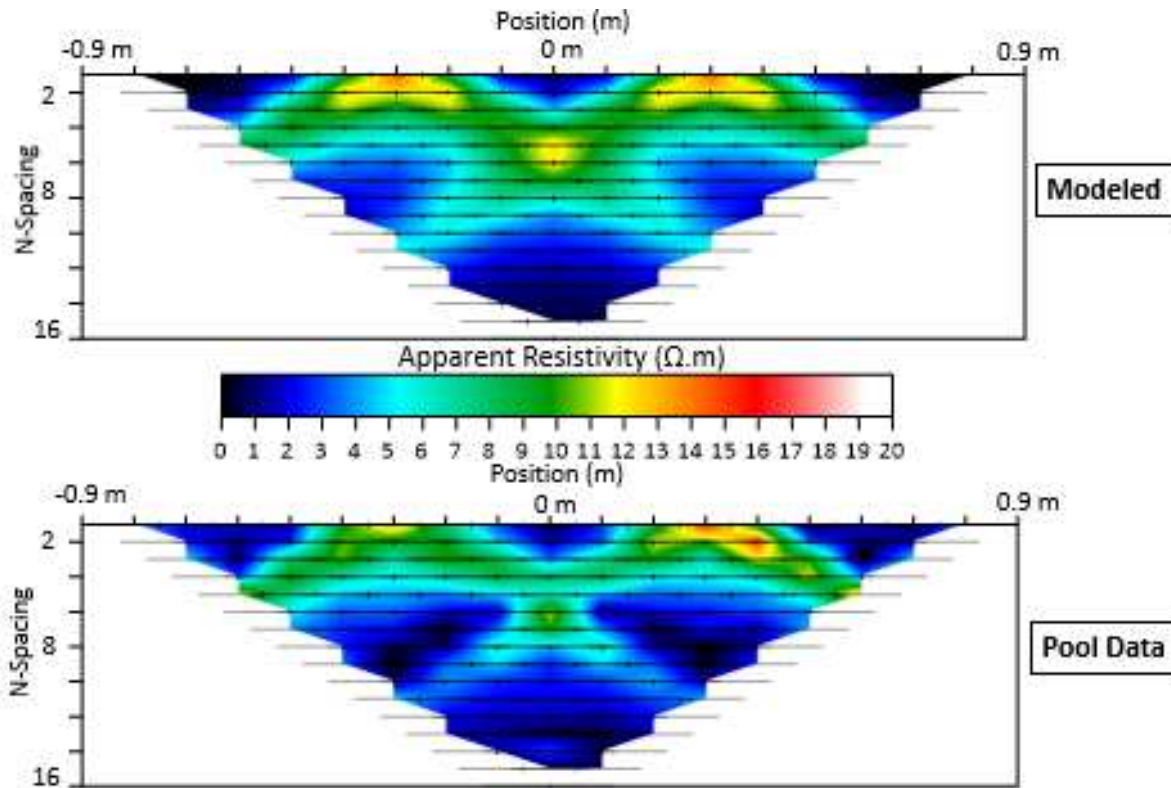


Figure 3.32: Isolated secondary response of dual vertical reference casings suspended beneath electrode seven and thirteen.

To more closely view the interaction between the two casings I have isolated secondary responses of both the MoM model and experimental data for this scenario (Figure 3.32). It can be seen that where the two responses meet there is a drop in apparent resistivity nearly equal to that observed near the surface location of the casings. There is an RMS misfit between the secondary responses of the MoM and experimental data of 0.246. A large portion of this is due to the weaker response seen in the left-most casing, which is likely due to small vertical positioning differences between the two casings.

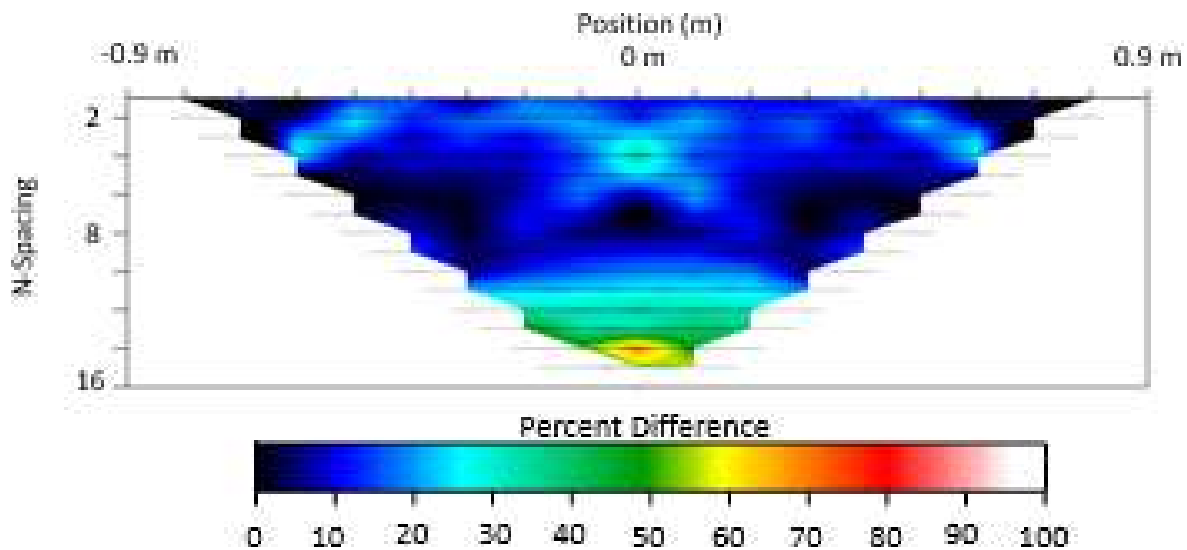


Figure 3.33: A point-by-point percent difference plot showing discrepancies between the MoM model and experimental data for our dual vertical casing scenario with the two suspended near one another. We see the largest percent differences (~35-40%) where the two secondary responses constructively interfere.

The point by point percent difference plot (Figure 3.33) produced between the numeric model and experimental data agree rather well in this case. Outside of the zone where we see resistive edge effects from the pool bottom, there is a maximum of ~40% difference where the two casings interfere. Another interesting observation can be made from the difference plot in this case; as there is a lower percent difference near the bottom of the pseudosection from the resistive edge effects. This is due to the constructive interference of the two secondary responses producing a drop in apparent resistivity similar to what we would expect from the pool bottom effect.

Next, I explore data with two of the control casings suspended vertically beneath electrodes four and sixteen, putting the edges of their individual responses just next to the edge of our apparent resistivity pseudosections (Figure 3.34).

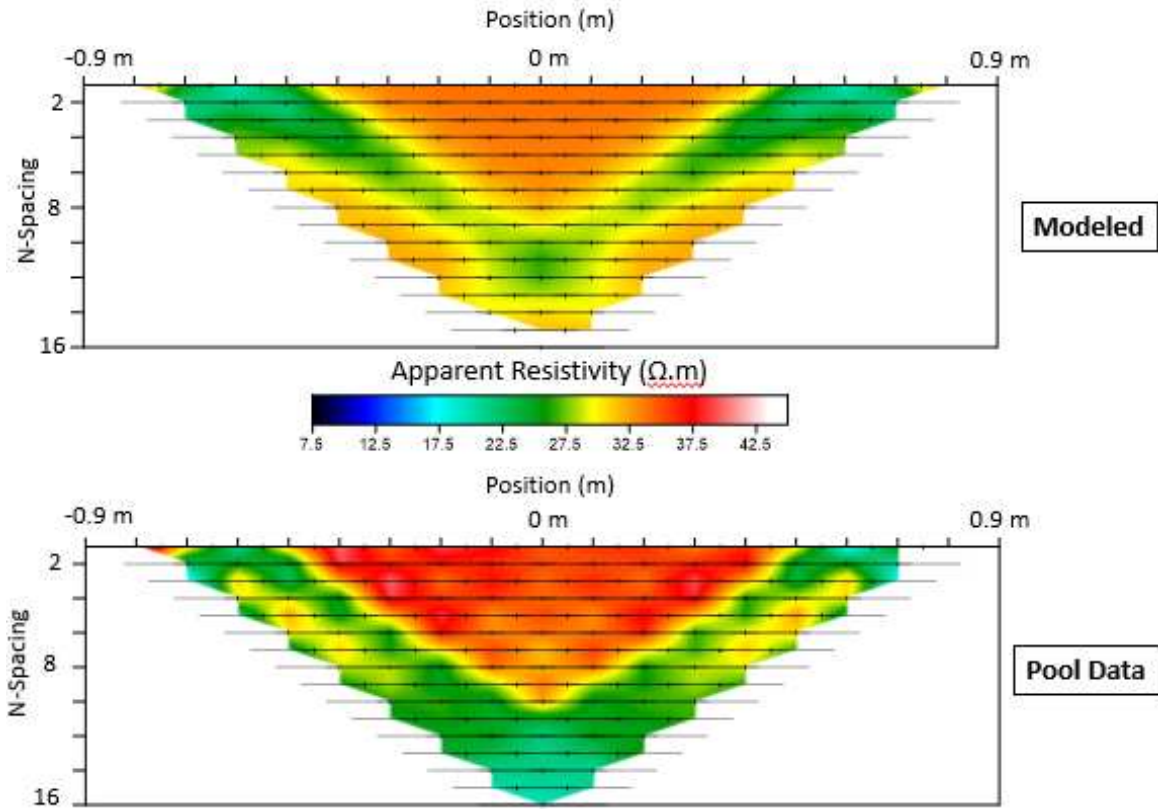


Figure 3.34: Experimental and MoM model apparent resistivity pseudosections of two vertical control casings positioned beneath electrodes four and sixteen. We again see constructive interference between the two secondary responses; however, in this case the interference occurs at a low data level, such that it is obscured by the resistive edge effects of the pool bottom.

This allows the majority of the secondary responses of each individual casing to be seen unhindered, with the two responses only beginning to combine near data level eleven. The two secondary responses interfere with one another constructively as they did in the near dual-vertical casing scenario. They produce a large zone of lower apparent resistivities as they merge with the resistive edge effects at the bottom of our section. Though the creation of a large zone of dropping apparent resistivity is still seen where the two responses interfere, it is not quite as clear in this case as the response begins to merge with the resistive edge effects produced by the bottom of the pool.

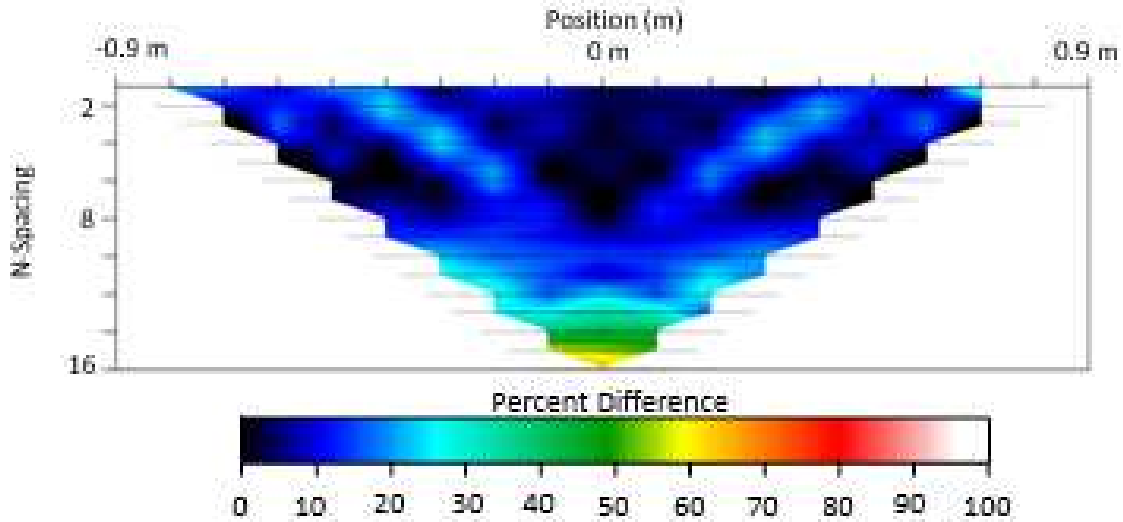


Figure 3.35: A point-by-point percent difference plot showing discrepancies between the MoM model and experimental data for the dual vertical casing scenario with the two suspended further from one another.

There are similar percent differences in the far dual vertical case (Figure 3.35) as observed in the section for the casings located closer to each other (Figure 3.33). The legs of the secondary response disagree by a maximum of $\sim 21\%$ at their peak and fall off to average 10% or less. There is a similar effect to that witnessed in the previous paragraph in that our interfering secondary responses with depth partially cancel out the resistive edge effects of the pool bottom and lower percent differences with deeper data levels to $\sim 10\%$.

I will now begin studies of a vertical casing adjacent to one of both a horizontal, and tilted orientation. I first discuss one vertical and one horizontal control casing in the geometry shown in figure 3.36.

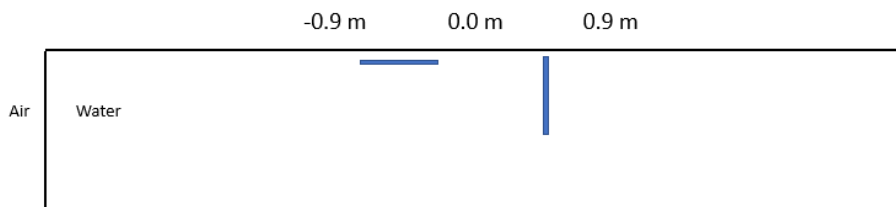


Figure 3.36: Schematic diagram of the multi-casing horizontal and vertical orientation survey.

Both casings are again identical regarding the dimensional and material properties. The vertical casing is suspended beneath electrode thirteen, and the horizontal one begins beneath electrode seven and extends in the negative X-direction.

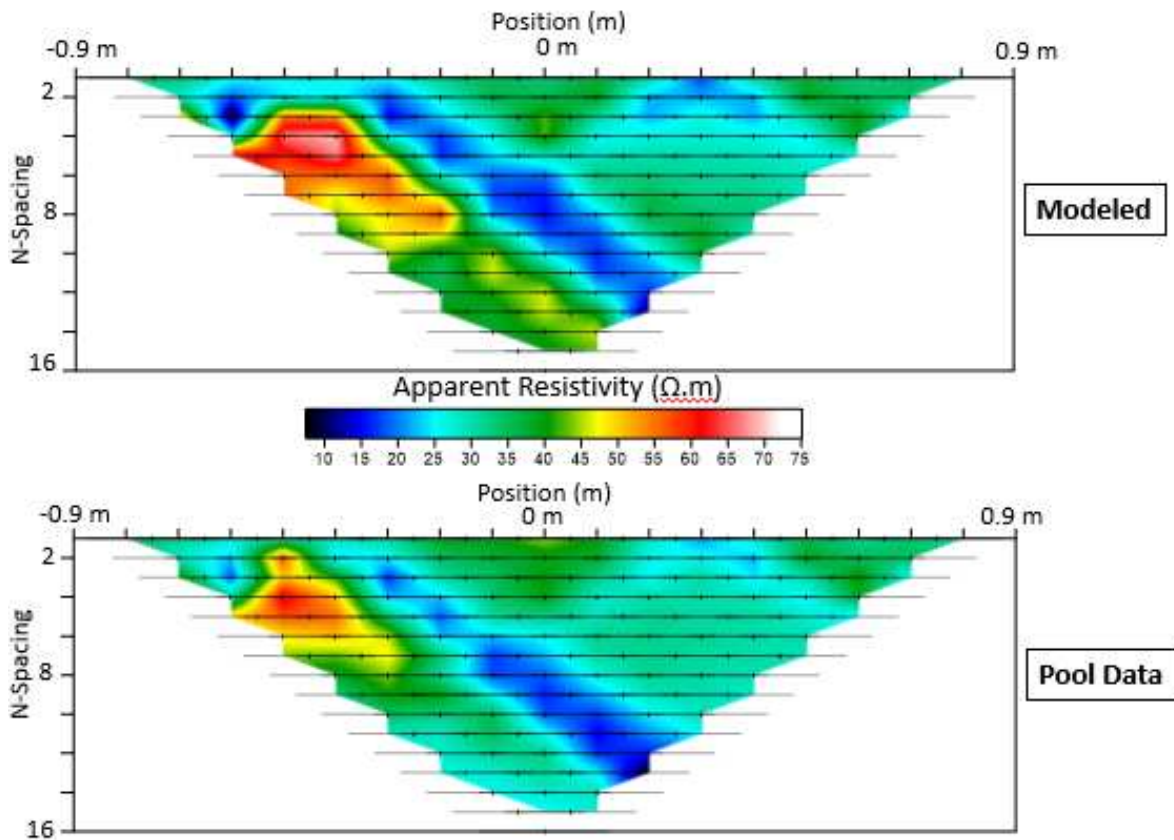


Figure 3.37: Experimental and MoM model apparent resistivity pseudosections of one vertical control casing beneath electrode thirteen and a horizontal control casing with its end beneath electrode seven and its length extending towards $X = -0.9$ m.

It is seen from the data again that the casings' individual secondary responses are similar to what was observed when they are suspended individually (Figure 3.37). As we found in the solo horizontal data of section 3.1.7, the secondary response from a horizontal casing produces much larger extremes in both high and low apparent resistivities with the leg of the maximum zone of response dropping to $15 \Omega\text{m}$ from a background of $34 \Omega\text{m}$. In contrast, the vertical casing produces a drop down to only $21 \Omega\text{m}$ at maximum. Because of this large discrepancy, where

the two responses interfere, in the center of the pseudosection at data level seven, the response of the horizontal casing dominates over that of the vertical casing.

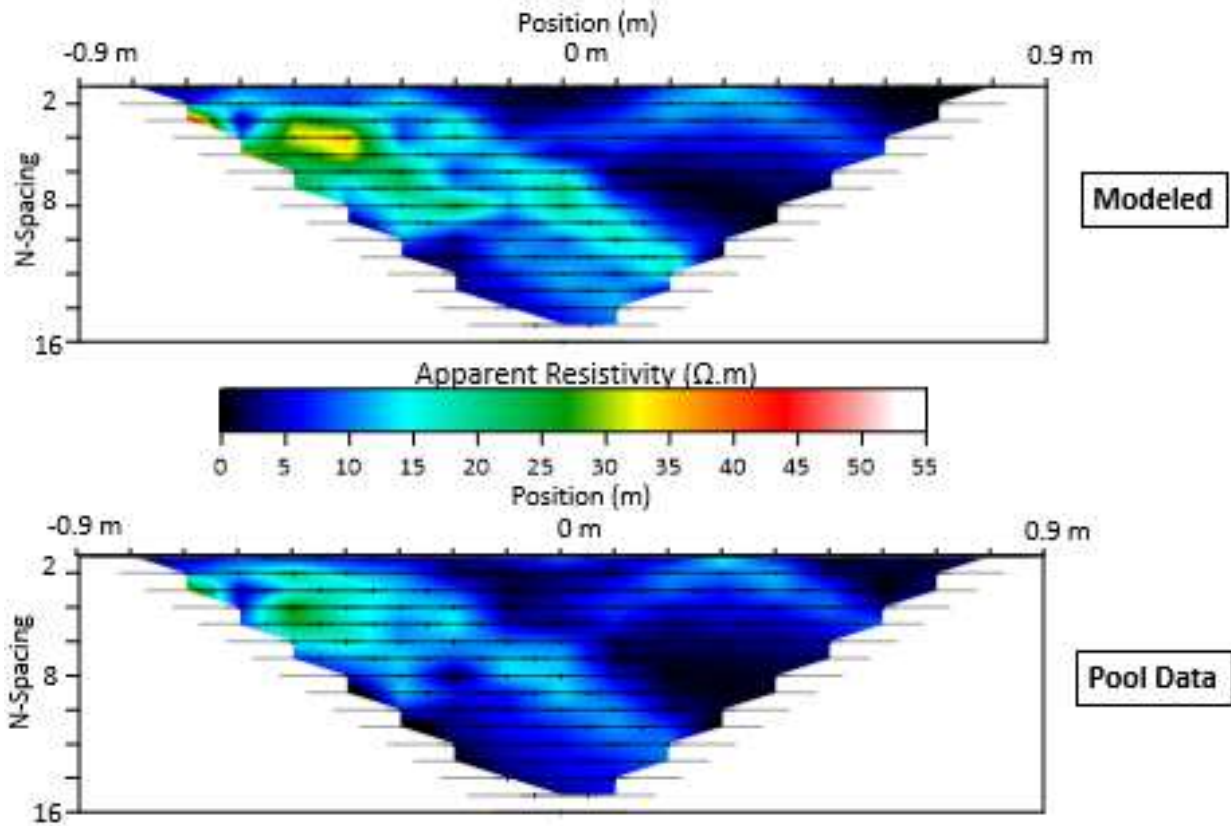


Figure 3.38: Isolated secondary response produced from adjacent horizontal and vertical reference casings.

Despite the overshadowing of the vertical response when compared to that of the horizontal response there is still a small constructive interference occurring near data level seven. Here the two secondary responses meet and produce a difference from the background apparent resistivity of $\sim 15 \Omega m$, compared to what is observed at the surface of the secondary response produced from the vertical reference casing.

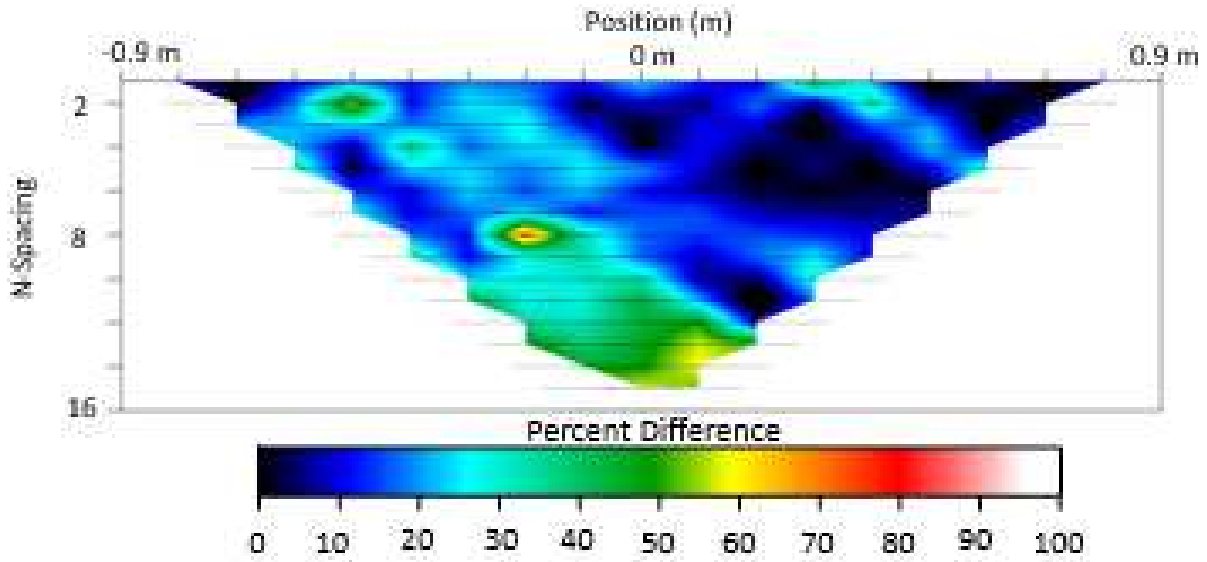


Figure 3.39: A point-by-point percent difference plot showing discrepancies between the MoM model and experimental data for our vertical and horizontal dual casing survey.

There are similar values within the percent difference plot (Figure 3.39) to what was observed in the dual vertical case. Along most of the secondary response produced from the vertical casings there are percent differences ranging from ~35-40%, however some regions reach as high as 70% which is likely due to small lateral offset between the two datasets.

I will now analyze data of an adjacent vertical and tilted casing. The tilted casing is again 60° from the vertical, except now tilted in the opposite direction as can be seen in figure 3.40, with its tip directly beneath electrode seven and the vertical casing suspended beneath electrode thirteen.

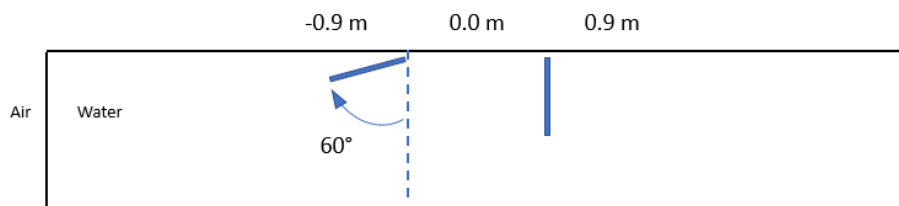


Figure 3.40: Schematic diagram showing the positions of the two casings for the vertical and tilted casing survey.

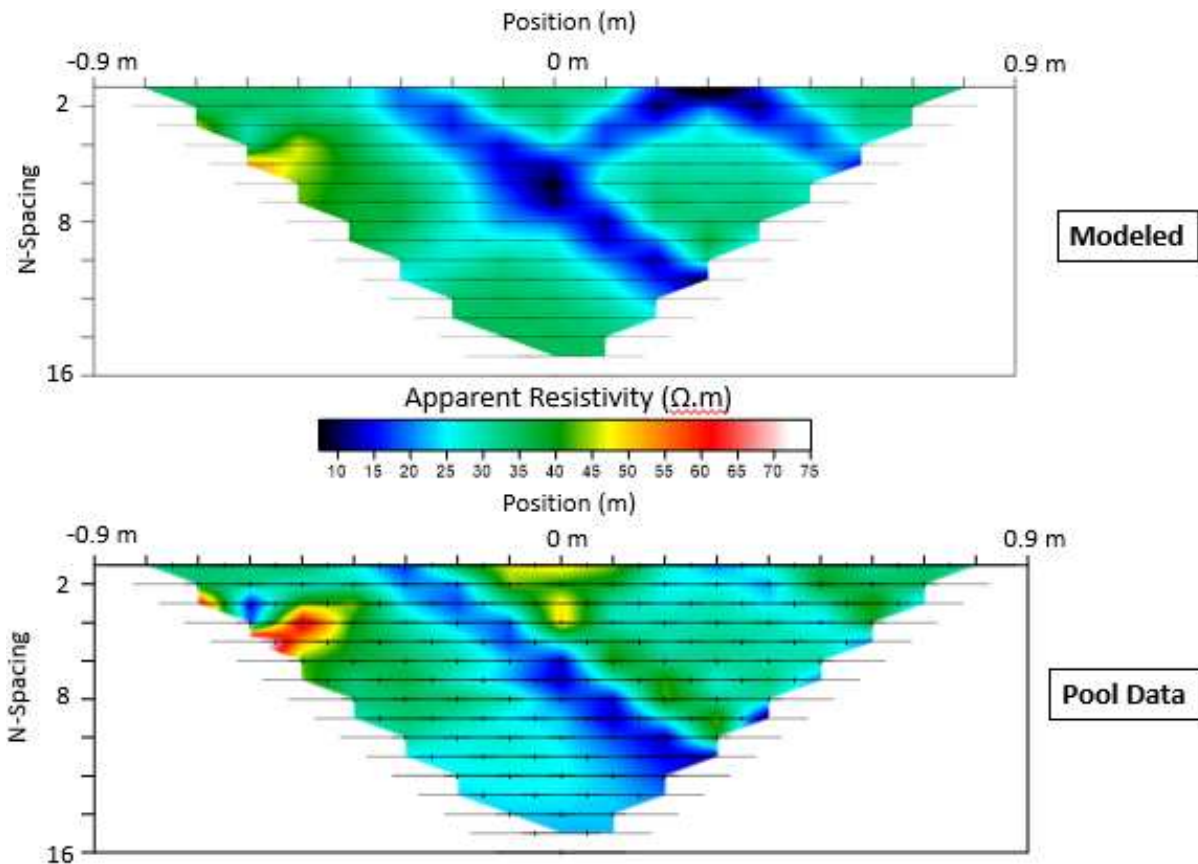


Figure 3.41: Experimental and MoM model apparent resistivity pseudosections of one vertical control casing beneath electrode thirteen and a tilted control casing with its end beneath electrode seven and its length extending diagonally in the negative X-direction.

Again, the individual secondary responses of the two casings are similar to their solo scenarios (Figure 3.41), with the tilted casing producing a zone of much lower apparent resistivities along the leg of the response than observed in the vertical case. Similarly to the adjacent horizontal and vertical case, the secondary response of the vertical casing gives a weak contribution where the two meet. This again reinforces the conclusion that in a field with complex infrastructure it is very important to have both a good understanding of the casings present as well as the expected secondary responses of those casings. Without this there is a very high risk of misinterpreting the data. Casings with weaker responses could modify a strong casing response, such as that from a horizontal or tilted casing, and mask targets in data even further.

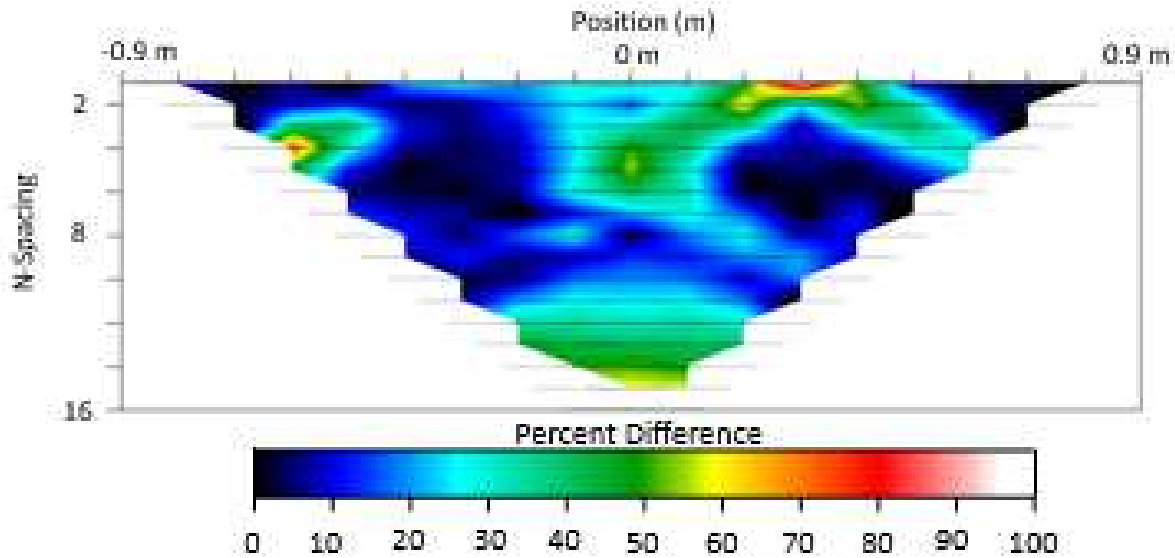


Figure 3.42: A point-by-point percent difference plot showing discrepancies between the MoM model and experimental data for the vertical and tilted dual casing survey.

There is a poor match between the numeric model and the experimental data again in this case. Much of this is due to the washout of the secondary response of the vertical casing when it comes into interference with that of the tilted, or horizontal. There is also a significant misfit with the vertical casing which is producing a weak response in the experimental data likely due to vertical positioning errors. The vertical-tilted case in particular has been modelled through more iterations than any other case, but persistently proves exceedingly difficult to achieve a good fit. For the two vertical casings where the two responses constructively interfered with one another, the amplification of the magnitude of response was handled well by the MoM modelled approach. However, with the complex orientations of the vertical-tilted and vertical-horizontal cases the large amount of uncertainties regarding their exact orientation for use as MoM parameters providing larger misfits in both cases.

3.1.10: Lab-Scale Experiment Conclusions

The flexibility and homogeneous background of the lab-scale pool experiment has allowed for the survey of casings with many different dimensions, material properties and orientations. It has led to a significant number of conclusions regarding secondary responses to be expected from a given change in these properties. Within this section I will discuss findings

and then provide an RMS error analysis regarding the misfits of our experimental data to the MoM numerical models produced for each case.

Many of the secondary responses will be compared to the reference casing of length 0.3048 m, outer radius 0.0164 m and inner radius 0.0131 m. This is due to its intermediate physical dimensions and material properties when compared to all other casings explored. I begin by discussing the effects of a changing casing width on the secondary fields while keeping the wall thickness and length nearly equal to that of the reference casing. From experiments with narrow and wide barreled casings I found that physical dimensions of casings affect the same dimension of the secondary response within apparent resistivity pseudosections. When viewing the narrow casing I observed that width of the zone of highest secondary response (corresponding to the zone of largest drop in apparent resistivity) began to pinch out and start returning to background resistivity near data level eight. Though this effect is diminished in the experimental data by the resistive edge effects of the pool bottom there is still a noticeable thinning of the maximum response with data-level particularly when compared with the wide barrel casing. I observed a similarly linear effect between a wider casing and the thickness of the zone of maximum response in apparent resistivity pseudosections in both experimental data and the MoM model. Even at the greatest data level at which the response can be observed, it extends laterally ~0.2 m in the model. The same amount of lateral growth in the experimental data led to the response merging with the resistive edge effect originating from the bottom of the pool and covering the entire area beneath the center of the pseudosection with a large drop in apparent resistivity excluding a small area in the center between the secondary response and the pool bottom effect.

The next physical property studied was casing length. Similar linear trends were observed with changing length as we found in the case of a changing diameter. The shortest casing, at 0.254 m, displayed a weak secondary response directly beneath the top-center of our pseudosection. This area was found to scale with the length of the casing in a similar way the legs of the secondary response scaled with casing width. The zone of strongest secondary response in the top-central area of the pseudosection extended only to the third data level within experimental data, and to the fourth (though fading at this point) within the MoM model. I then explored the data from a casing of length 0.6096 m and found the corresponding effect to be true

with a growing casing length. This casing, two times the length of the reference and 2.5 times the length of the shortest casing, produced a secondary response visible within a large region underneath the central part of the electrode array. The zone impacted by strong casing response connected with the zone impacted by strong resistive edge effects of the pool bottom and filled in the area beneath top center entirely from top to bottom with a large drop in apparent resistivity. Despite the differences in geometry of the casing response, the maximum magnitude of the response was similar for casings of different sizes.

I will now explore the findings from a change in material properties of the casing. I discussed in section 3.1.7 a casing made of brass with a conductivity 2.5 times larger than that of the reference casing and dimensions (except for wall thickness) similar to those of the reference casing. Although we may expect that difference in conductivity to be insignificant from the analytical and numerical studies in Chapter 2, I found this change to make a difference in apparent resistivity pseudosections. In the scenario of the reference casing I observed a maximum drop from the background of $34 \Omega\text{m}$ to an apparent resistivity of $\sim 21.5 \Omega\text{m}$ or 37%. For the brass casing in the same background of $34 \Omega\text{m}$ I found values as low as $18 \Omega\text{m}$ or a total drop from the background of 48%. This was consistent over multiple surveys of the same casings. This discovery leads the conclusion that though the physical dimensions of the casing being surveyed largely controls the shape of the secondary response observed, the material of the casing itself is one of the largest contributors to the magnitude of the response.

To answer the question of the effect of total volume of metal on secondary response I also surveyed two aluminum casings 0.6096 m long with outer radii of 0.0065 m. One has an inner radius of 0.0045 m and the other is solid. I found that there is not only a slightly wider secondary response within the data collected over the solid casing, but also a stronger drop in apparent resistivity from the background. This indicates that it is not strictly the material properties of the casing that determine the magnitude of a given secondary response, but also the amount of that material present.

Finally, I studied the effects of multiple adjacent casings suspended within the experiment and surveyed simultaneously. I found casings of equal secondary response magnitude, such as dual-vertical scenarios, to enhance one another where they intersect creating a zone at deeper data levels similar in magnitude to the casing response at the surface. The dual-

vertical casings near one another discussed in section 3.1.8 for example produce a centralized zone of constructive interference at data level six with a maximum drop in apparent resistivity of 34% from the background of 34 Ωm as compared to the 38% drop from the background resistivity produced by the casings at data levels one and two. For our more complex geometries such as a vertical casing adjacent to one of tilted or horizontal orientation, I found that the secondary response from the vertical casing was often overshadowed in magnitude by the tilted or horizontal. The drop in apparent resistivity produced from tilted and horizontal casings within their zones of maximum response averaged 50% and 66% from the background resistivity respectively over the 35-40% drop seen with vertical casings of the same dimensions and material properties. This led to the adjacent vertical responses either blending into or being cut off by the significantly larger drops in apparent resistivity produced by the tilted or horizontal orientations.

Though I have provided percent difference plots for each individual experiment and MoM model that gives an idea of the level of disagreement between each it is useful and concise to describe the misfit of each scenario with a single value. To provide a quantitative sense of how well our MoM models have fit their respective experiments and present them in a concise way I have produced an RMS error value for each case.

Table 3.2: Calculated RMS error values between our MoM models and experimental data for each lab scale survey discussed. Scenarios with “Es” tag are isolated secondary responses.

	RMS		RMS
Background	0.357	Brass	0.423
Reference	0.377	Brass Es	0.19
Reference Es	0.091	Tilted	0.467
Long	0.296	Horizontal	0.638
Short	0.327	Vertical + Vertical Near	0.513
Wide	0.312	Vertical + Vertical Near Es	0.246
Narrow	0.41	Vertical + Vertical Far	0.408
Hollow	0.392	Vertical Tilted	0.617
Hollow Es	0.319	Vertical + Horizontal	0.637
Solid	0.443	Vertical + Horizontal Es	0.43
Solid Es	0.322		

Table 3.2 lists each casing I have studied and its associated RMS value. I used equation (3.1). There is a general trend of better fit when modelling the simple vertical casings. An important point to also consider is the asymmetry artifact that so strongly effected the hollow, solid and brass casings. The more complex casing orientations present slightly higher RMS errors on average. With the highest belonging to the horizontal orientation and the vertical-tilted and vertical-horizontal scenarios. The horizontal case presents a variety of challenges in modelling as a slight skew in any direction will produce strong variations in the casing response. I have tried adjusting the casing location in our MoM model slightly to improve the match between the MoM and experimental data, but that is a time-consuming and tedious process

3.2: Introduction of Mid-Scale Experimental and Method of Moments Data

During the construction of the CoorsTek Center for Applied Science and Engineering on the Colorado School of Mines campus, an adjacent grassy field known as Kafadar Commons was stripped as a staging ground for construction equipment. During construction Dr. Richard Krahenbuhl of the CSM Geophysics department proposed the construction of an underground laboratory to be buried beneath Kafadar during this time that includes various geophysical field work targets with a number of material and dimensional properties seen in figure 3.43.

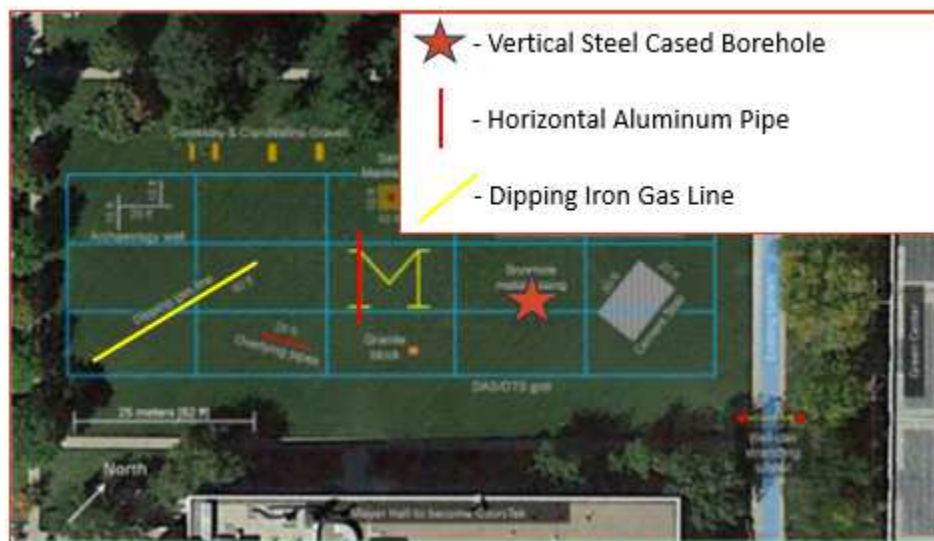


Figure 3.43: Plan view map of the Kafadar Commons buried geophysical laboratory on the Colorado School of Mines Campus (Krahenbuhl et al., 2018).

Of the many targets buried beneath this field, three are of particular interest to this study: a 15 m vertical steel cased borehole, a 6 m horizontally oriented aluminum pipe, and a 27 m dipping iron gas line. Surveys covering all of these targets with the exception of the dipping iron gas line will be covered within section 3.2. The dipping iron gas line was excluded from being surveyed as it was kept true to working gas lines and wrapped in an electrically insulating lining to prevent corrosion. The vertical and horizontal pipes were both successfully surveyed with DC resistivity methods. The vertical casing is 15 m in length, with an outer diameter of 0.156 m, and an inner diameter of 0.1524. The horizontal aluminum casing presented a bit more of a challenge within its analysis; its length is known to be 6 m, and sub-mm accuracy GPS points have been gathered for its ends giving an excellent accuracy in survey setup, however its inner and outer diameter were not documented. Due to this several MoM models have been run and the casing's radial dimensions have been estimated by using the theory discussed in chapter 2.

3.2.1: Analysis of Vertical Borehole Survey

For the surveying of the 15 m vertical steel-cased borehole on Kafadar I again make use of AGI USA's SuperSting R8 DC resistivity instrument. I used 20 stainless-steel electrodes spaced at 1 m for a total array length of 19 m using the same array type utilized at the pool scale of dipole-dipole. To best understand the Kafadar experimental environment I took two parallel surveys spaced 3 m from one another. Care was taken in the design of the experiment to use our sub-mm accuracy GPS to ensure the survey crossed directly over the vertical borehole.

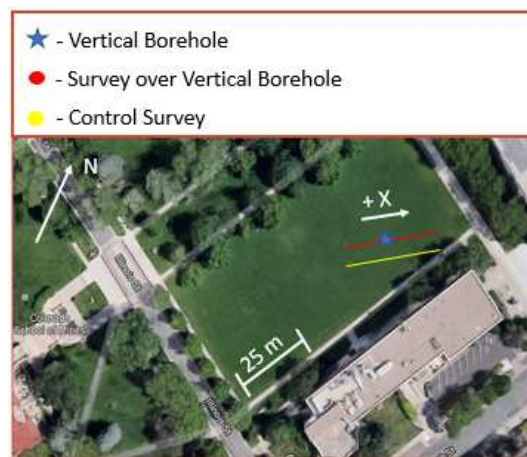


Figure 3.44: Plan view map of Kafadar Commons highlighting the location of the steel-cased vertical borehole, and its associated DC resistivity surveys. (Google Maps, 2019).

I will first discuss the control survey designated by the yellow line in figure 3.44. The control survey was designed to replicate the borehole setup exactly, but instead senses mainly the background conductivity structure of Kafadar Commons.

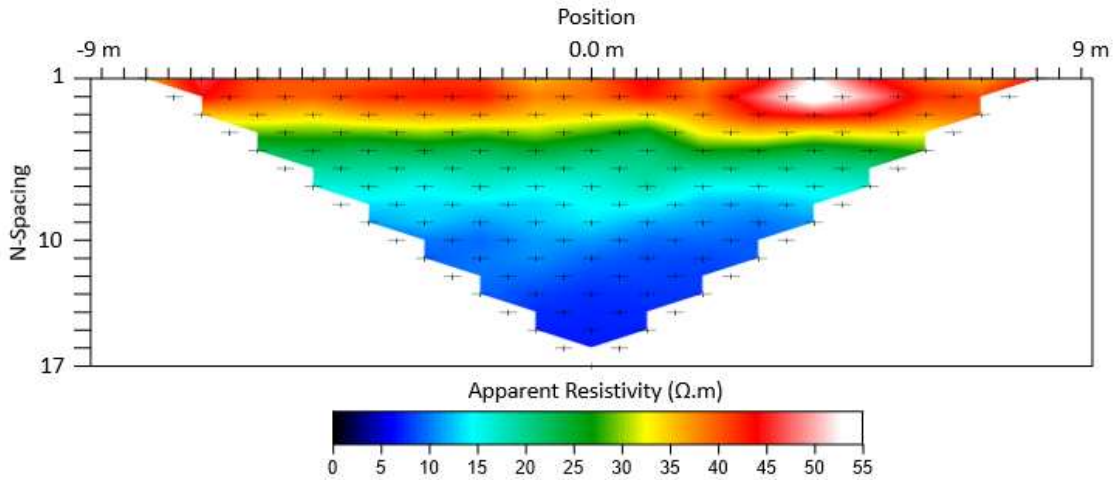


Figure 3.45: Apparent resistivity pseudosection of the control line parallel to and offset by 3 m from the vertical borehole survey. Gathered using AGI USA SuperSting R8 DC resistivity instrument, and 20 stainless-steel electrodes spaced at 1 m.

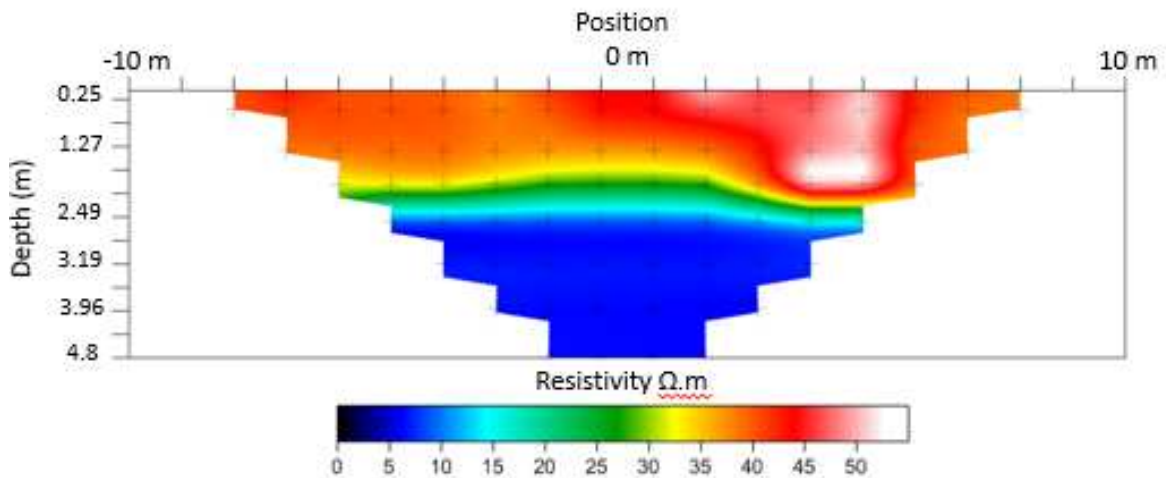


Figure 3.46: Inversion of the control survey. Created using 19 iterations within the DC resistivity software “RES2DINV” to an RMS value of 0.27%. A resistivity-depth profile derived from this section is used as input for the MoM modelling code.

Unlike the lab-scale experimental environment which provides a nearly homogeneous background to conduct experiments in, here I observe (in first order) a layered Earth response (Figure 3.45) which decreases in apparent resistivity with data level (i.e., resistivity decreases with depth). Though a layered Earth response was expected from the mid-scale field work, variations in apparent resistivity were stronger than expected. The MoM code can account for layering (a feature that was unnecessary at the lab-scale) which will create a better fit to our experimental data. However, as an input for the code I need depths and true electrical conductivity values, something which I do not receive from raw DC resistivity data. Using RES2DINV (Loke, M. H., 2010) I have inverted the raw data through 19 iterations and to an RMS error value of 0.27% to produce the resistivity-depth section shown in in figure 3.46. From this section I derived a layered Earth that was used as input for the MoM layered Earth solution. My layered model consists of of two layers over a halfspace. The first layer extends 2 m from the surface, the second extends 0.5 m from the base of the first, and halfspace begins from the base of the second with electrical resistivities of 42 Ωm , 25 Ωm and 7 Ωm , respectively.

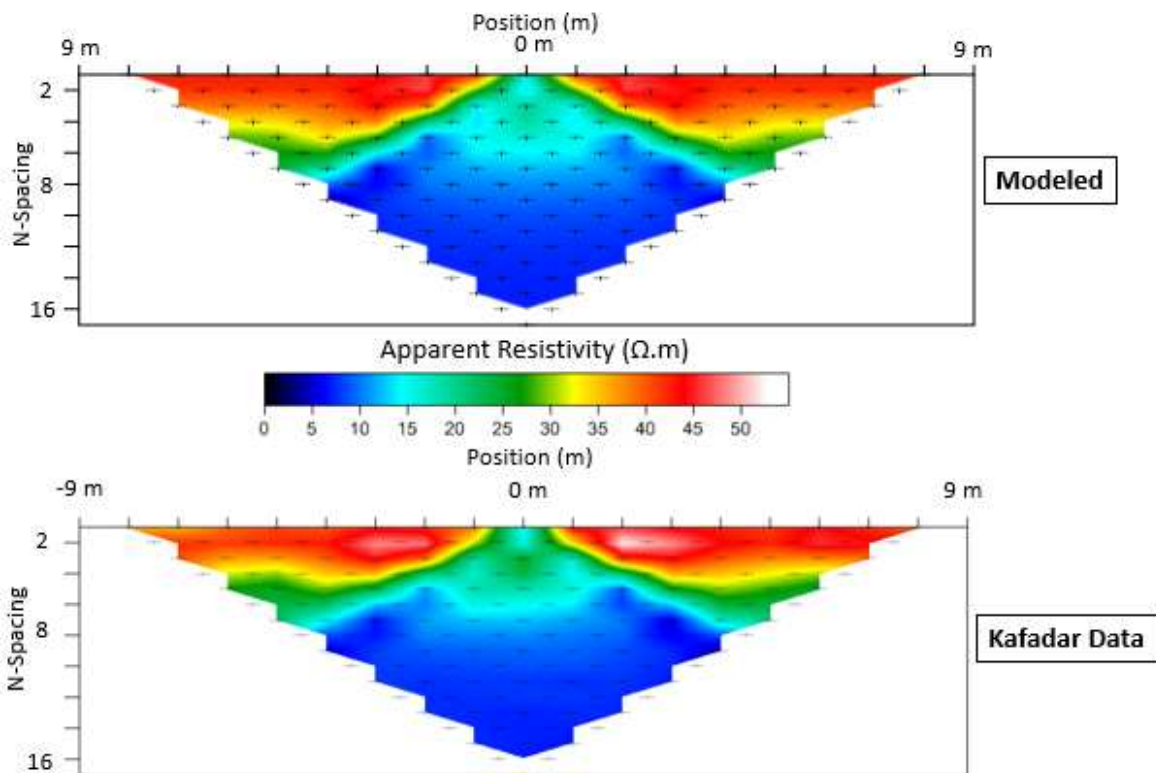


Figure 3.47: Apparent resistivity pseudosections produced from the MoM model and associated experimental data gathered over the steel-cased vertical borehole buried in Kafadar Commons.

When viewing the apparent resistivity pseudosection produced from the vertical borehole survey (Figure 3.47) I observe maximum drops in apparent resistivity from the background of ~63%. Due to the large decrease in apparent resistivity with pseudodepth I observe an interesting feature in that the secondary response begins to merge with the background. This produces an effect very similar to what was observed in the lab-scale data where the responses of the larger casings (length = 0.6096 m or outer radius = 0.0295 m) would merge with the resistive edge effects of the pool bottom at larger data levels.

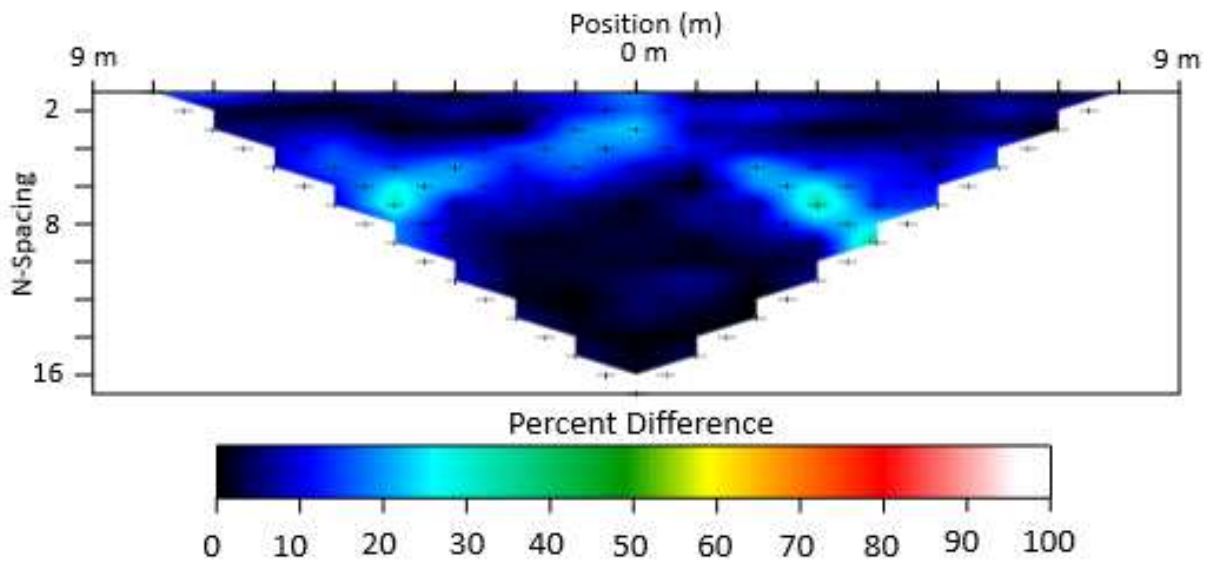


Figure 3.48: Point-by-point percent difference plot produced from the misfit between the MoM model and experimental data of the vertical borehole survey in Kafadar Commons.

Figure 3.48 shows percent differences of 30-40% at maximum along the zones of strongest secondary response. The layered Earth model fits well enough with experimental data that in zones outside of the secondary response we observe some 0% differences. Within the survey geometry the vertical casing is centered between electrodes ten and eleven. This means having one of the dipole centers exactly above the center of the casing. The Hankel integrations that take place within our MoM modelling code are not yet handled correctly and return unrealistically high secondary field values when the casing center is in the same lateral location

as one of the dipole centers. To mitigate this issue, I have shifted the casing out of line from the electrode array along the y-axis by 0.20 m (Figure 3.49).

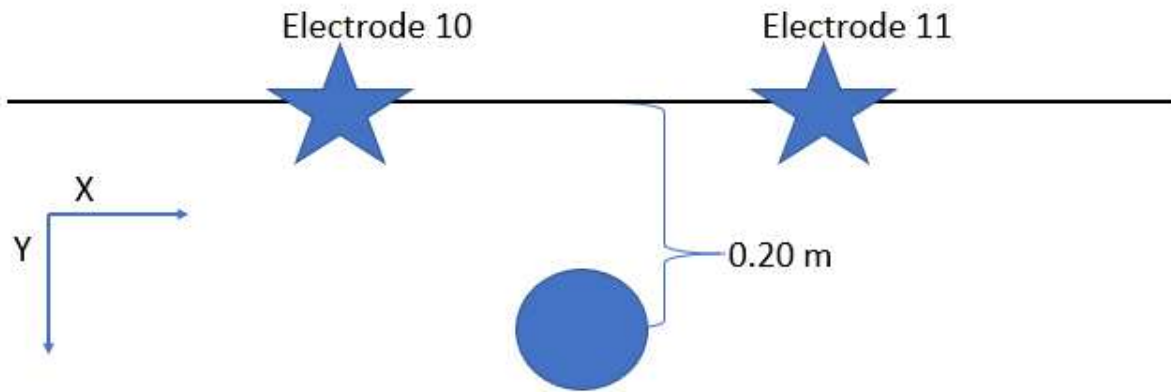


Figure 3.49: Schematic diagram illustrating the out-of-line offset used in the MoM modelling of the vertical borehole in Kafadar Commons.

This level of offset produces a secondary response in good agreement with that of the field data, while avoiding the issue produced from Hankel integrations breaking down at near zero X-axis offsets.

3.2.2: Analysis of Horizontal Aluminum Pipe Survey

A large level of creativity went into the planning of what has affectionately become known as the geophysics playground buried beneath Kafadar Commons. One of the most creative of which is a large “M,” representative of “Mines,” centered under the field. The “M,” approximately 7.5 m by 7.5 m was constructed such that each leg of the letter is made of a different material to produce a variety of targets for geophysical instruments. These range from clay, cement, aluminum, iron, railroad ties and both an air and salt water filled PVC pipe. Our horizontal aluminum pipe makes up the longer left leg of the “M.” The horizontal pipe presented several challenges as the inner and outer radii of the pipe, as well as its depth of burial were unknown.

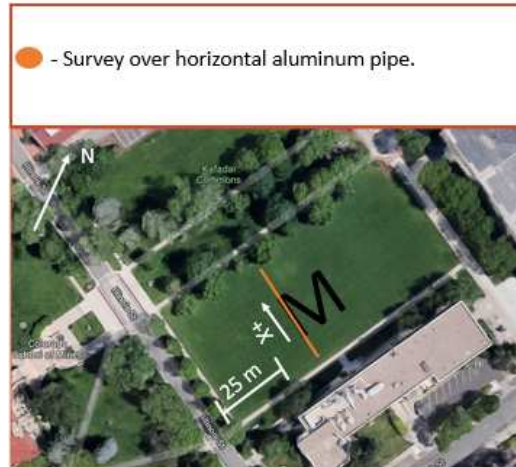


Figure 3.50: Plan view map showing the location of the buried horizontal aluminum pipe in Kafadar Commons and its associated DC resistivity survey.

A similar survey geometry was used for the case of the horizontal aluminum pipe to that used for the vertical casing, however it needed to be altered slightly to better represent data observed at the lab-scale. It was observed from trying arrays of several lengths that the survey line needs to extend significantly beyond the ends of the pipe when surveying in line along a horizontal pipe to view the full secondary response. In the lab-scale scenario the horizontal casing was centered beneath an array six times its own full length; for the case of the Kafadar Commons survey it is only possible to reach an array length of four times the length of the buried aluminum casing before the survey approaches the sidewalks on either side of the field. I used 24 stainless-steel electrodes spaced at 1 m in line with the casing. With this array length I observe a horizontal casing secondary response (Figure 3.51) very similar to what was found at the lab scale. Due to nearby buried objects there was no room for a control survey in this case so a background similar to that used in the vertical borehole case was used here as well with slightly thicker layers of 2.5 and 2 m over a halfspace. Through multiple iterations of modelling the horizontal pipe with the MoM code outer and inner radii of 0.0381 and 0.03048m were used respectively with a burial depth of 0.9 m. The aluminum of this horizontal pipe was assumed to have equal electrical conductivity of the aluminum casings survey at the lab-scale of 3.5×10^7 S/m.

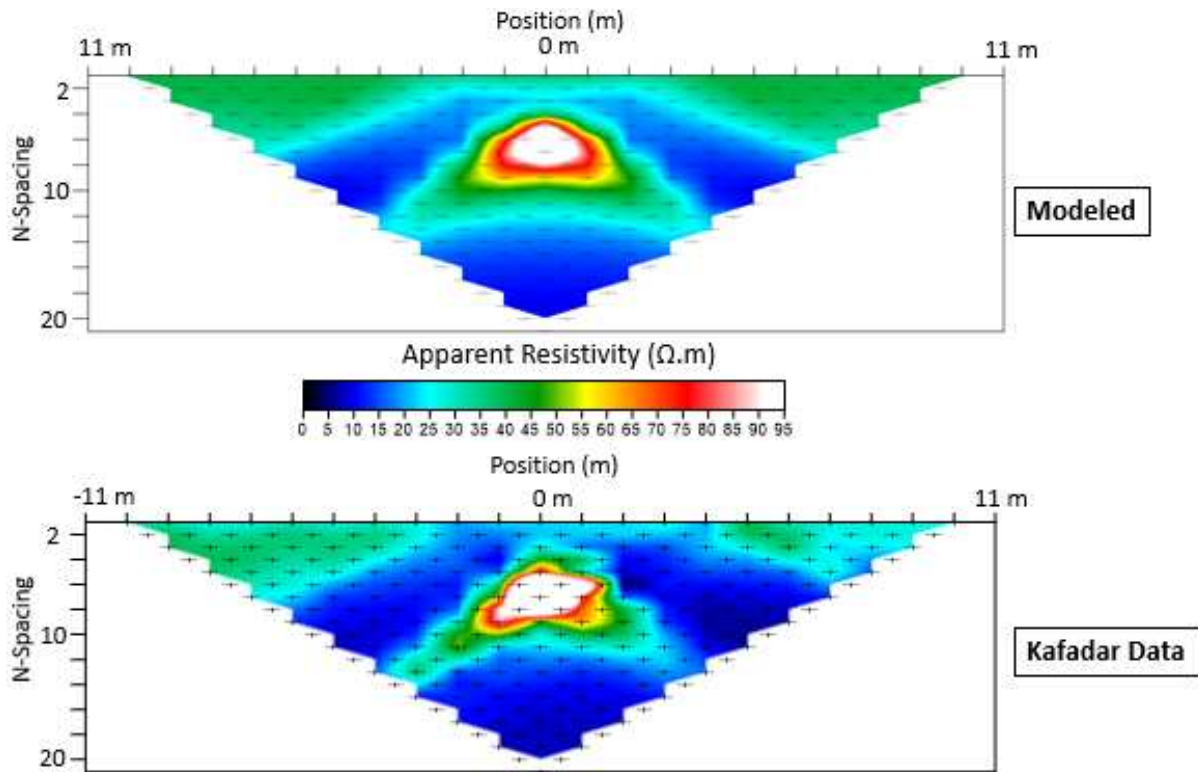


Figure 3.51: Apparent resistivity pseudosections produced from the MoM model and associated experimental data gathered over the 6 m long horizontal aluminum pipe buried in Kafadar Commons.

Thick, strong decreases in apparent resistivity are seen along the legs of the response dropping from the background of $\sim 40 \Omega\text{m}$ to $10 \Omega\text{m}$ in some places or a total of 75%. There is deviation from the ideal horizontal secondary response in the experimental data which among other uncertainties, could likely be due to the upper left corner of the M that corresponds to the right-hand side of the experimental data section. This upper left-hand section of the M is composed of a clay pipe perpendicular to the aluminum being targeted. The left-most middle section of the M is a wooden railroad tie also electrically resistive. It is very likely it has introduced artifacts into our dataset. There is also the familiar zone of very high apparent resistivity within the central zone of the response as was observed in the pool experiment. Again, when conducting a DC resistivity survey inline along a horizontal pipe the injected current is channeled into the casing and then laterally through the medium it is suspended within leaving a region of low current density corresponding to the high apparent resistivities present. It is also apparent that I again find the effects of the layered background of Kafadar Commons. In the lab-scale pool

experiment there is a return to the background apparent resistivity beneath the region of very high apparent resistivities, however the drop in apparent resistivity with pseudodepth produced from the layered Earth ties into the zones of strongest secondary response with the horizontal pipe as it did with the vertical borehole in the Kafadar experiments.

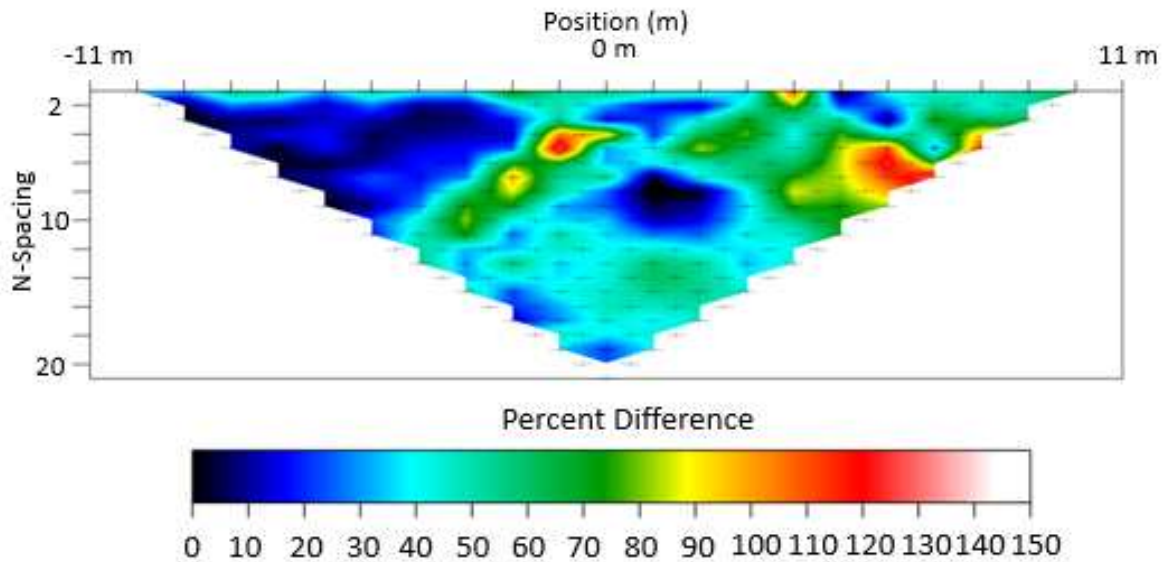


Figure 3.52: Point-by-point percent difference plot produced from the misfit between the MoM model and experimental data of the horizontal aluminum pipe survey on Kafadar Commons.

Though there is a reasonable qualitative match between the field and MoM data (Figure 3.52), percent differences are significantly higher in the horizontal case than for the vertical casing. This is due to the uncertainties in the dimensional properties of the aluminum casing as well as the adjacent section of the buried M which is a perpendicular, electrically resistive pipe. For both vertical and horizontal scenarios only their lengths and materials were known with full certainty, however for the vertical borehole I was able to remove the cap where the casing reaches the surface and measure its inner and outer radius. For the horizontal scenario its exact position and length are known, however its inner and outer radius, as well as its depth of burial is unknown. Through multiple iterations it was possible to calculate a MoM model near appropriate to the response observed from the experimental data by using the theory on variations in secondary fields with changing casing properties in chapter 2. Final inner and outer

radii values of 0.0381 and 0.03048 m with a burial depth of 0.9 m were used. However, there is still a level of misfit significantly greater than that of any of the other experiments which could be diminished by exhaustively modelling a wide variety of possible radii and burial depths as well as including adjacent buried objects in the model parameters.

3.2.3: Mid-Scale Conclusions

The underground laboratory constructed on Kafadar Commons at the CSM campus has provided an excellent opportunity to survey both vertical and horizontal casing targets at a scale larger than the lab-scale experiments, and with a more realistic background without having to travel to the large-scale field site and survey a full-scale abandoned oil and gas well. I found Kafadar to have a very layered resistivity structure decreasing quickly with depth from about 40 Ωm to below 10 Ωm . This provided an opportunity to test the MoM model with a layered Earth input which has proved quite effective. The 15 m long vertical steel-cased well produced maximum drops in apparent resistivity from the background of 63%. The MoM model in the presence of a layered earth produced slightly higher misfits, but still within the range of 40-50%. Using equation (3.1) I calculate an RMS misfit of 0.422. The 6 m horizontal aluminum casing surveyed produced maximum drops from the background of 75% showing similar trends to what was observed from horizontal casings in the pool experiment with much wider bands of dropping apparent resistivity and a very high apparent resistivity zone beneath this drop correlating to an area of low current density. There is a reasonable qualitative match between the MoM solution and the experimental data for the horizontal pipe but percent differences are high with values up to 120%. There is an RMS error in the horizontal case of 1.078.

3.3: Introduction of Large-Scale Experimental and Method of Moments Data

In November 2017 field work was conducted in eastern Colorado as the first ground truthing of the MoM modelling code. Using the Colorado Oil and Conservation Commission's (COGCC) vast database of active and abandoned/plugged wells many possible abandoned wells to potentially serve our purposes as a real-world scale field survey site were found. After a considerable amount of time finding the best field to conduct the survey in and calling landowners we identified a suitable site containing a vertical, steel-cased well that was abandoned in the 1980s. The COGCC database allowed us some certainty as well regarding the dimensional properties of the casing which had a length of 130 m and an outer and inner

diameter of 0.21 m and 0.19 m respectively. The field surrounding the casing is roughly 500 m X 500 m giving us room to design a survey of sufficient dimensions.

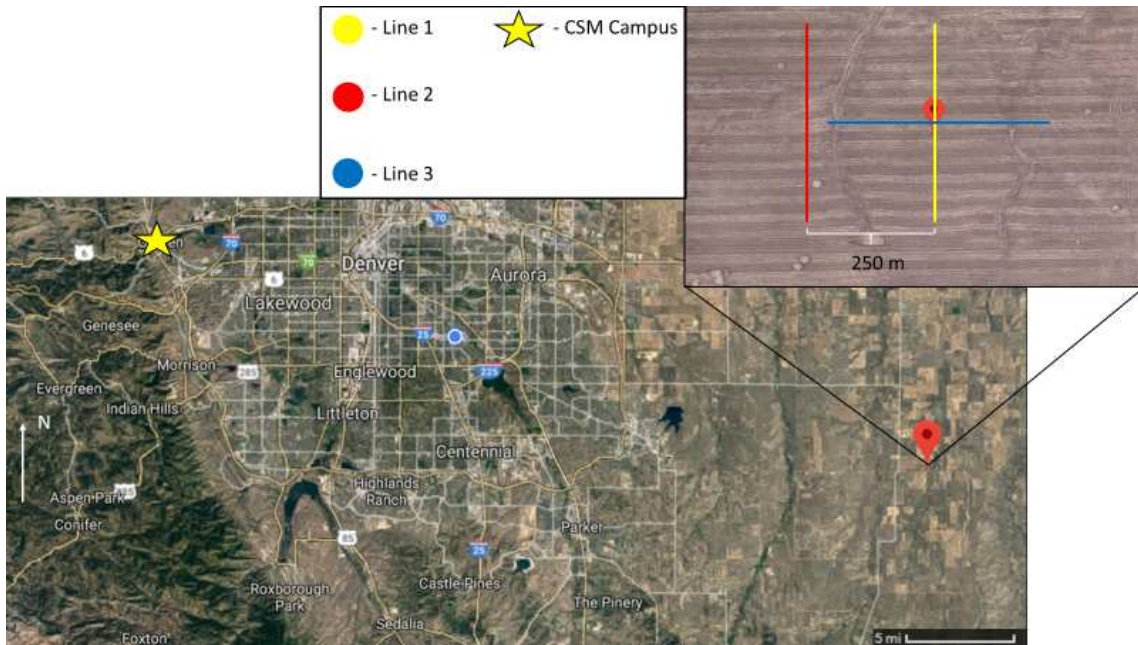


Figure 3.53: Map showing our large-scale field site in eastern Colorado in relation to the CSM campus. A pop-out map shows the location of three different DC resistivity surveys conducted.

This site is located roughly an hour's drive east of the CSM campus. Figure 3.53 shows the location and a pop-out map of the field site. We conducted three different DC resistivity surveys. Two survey lines are perpendicular to one another, and a third line is parallel to "line 1" and offset from the casing by 250 m. In the following sections I will discuss these three surveys as well as their associated MoM model.

3.3.1: Analysis of Large-Scale DC Resistivity Data

To accomplish the large-scale field work we decided to make use of the space we had available and use a 320 m long dipole-dipole array. The array was made up of 64 steel electrodes spaced at 5 m. The vertical, steel-cased well described in section 3.3 is centered (as near as possible) beneath the survey line. The well-head was found using GPS coordinates and a hand-held magnetometer. A key element in gathering DC resistivity data is a relatively

homogeneous background (as in the lab-scale experiments) or a layered-Earth environment (as in the mid-scale experiment); we were fortunate to find good conditions at this field site. This allowed for a simple analysis and modelling process.

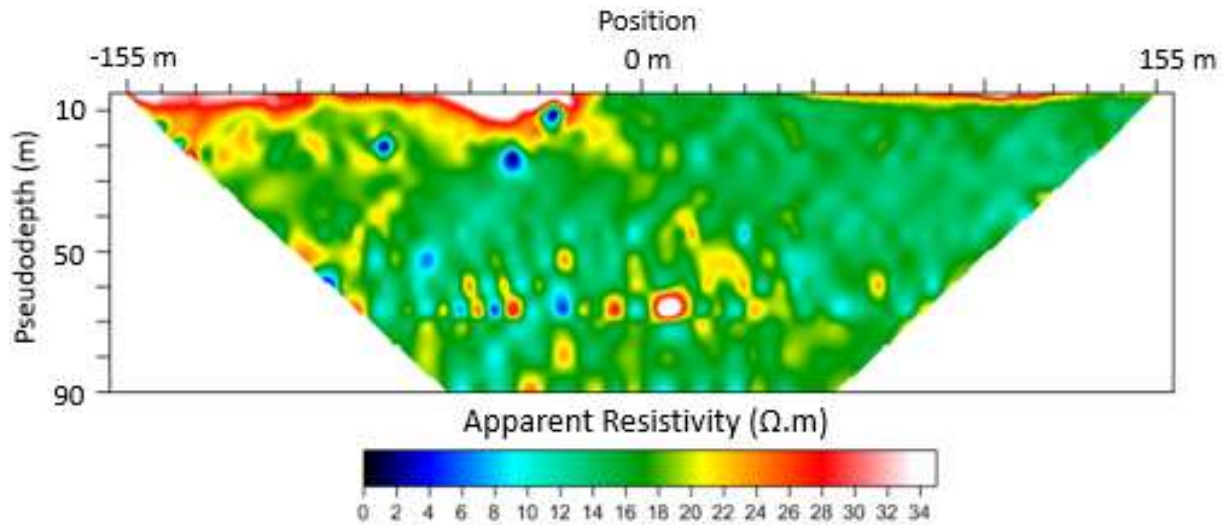


Figure 3.54: Apparent resistivity pseudosection of an offset and parallel control survey conducted to better understand the background conductivity structure of the large-scale field site.

As is observed from figure 3.54 the background is not perfectly homogeneous, but most of the pseudosection displays apparent resistivities of 15-16 Ωm . At ~ 70 m pseudodepth in all field data there is linear zone of noise that is likely due to variations in spontaneous potential (SP) between current and potential electrodes (Hoogervorst, 1975). At larger transmitter-receiver spacings (i.e., deeper pseudodepths) this effect is amplified. In our case it seems that one individual level of pseudodepth observed this effect more strongly than others. This could also have occurred due to an instrumentation interpolation error at this pseudodepth as the resistivity instrument used for the large-scale surveys changes its physical transmitter dipole lengths throughout the survey to minimize total data points leaving some zones of the dataset more finely sampled than others. This was accomplished by the two electrodes making up the dipole “A” being spacing further from one another than adjacent electrode spacing.

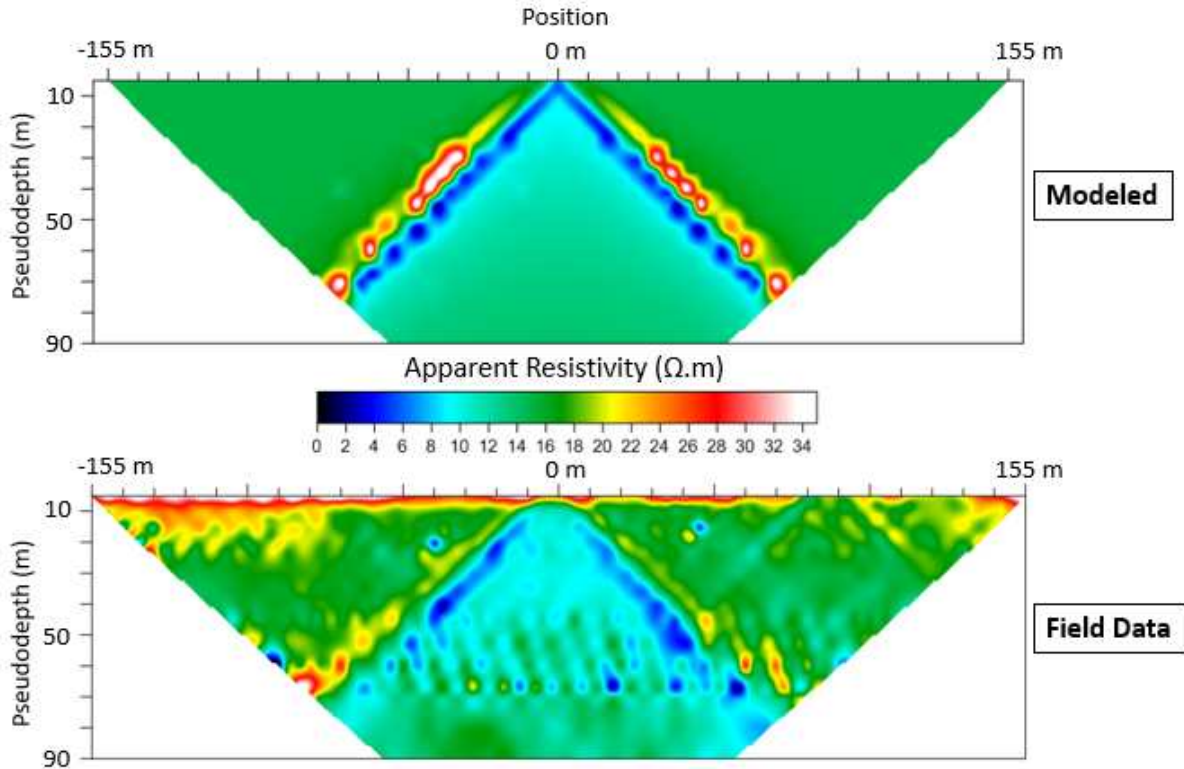


Figure 3.55: Apparent resistivity pseudosections produced by MoM and experimental data of line 1 from figure 3.53

Figure 3.55 shows MoM modelled and experimental data surveyed over the steel-cased well. There are noticeable misfits produced from inhomogeneities and noise in the experimental data, however there is still a good qualitative fit between the two datasets. There are maximum drops in apparent resistivity from the 15 Ωm background of 74%. The MoM model itself also shows a secondary response that is not perfectly smooth in this case. This is due to the aforementioned changing physical dipole length of the DC instrument used for these surveys. To create a model that uses the same datapoints as the field data for comparison between the two datasets it was necessary that there was not a uniform spacing between data points laterally nor vertically. This causes the appearance of the pseudosection to rely on the interpolation methods used in mapping software creating the image.

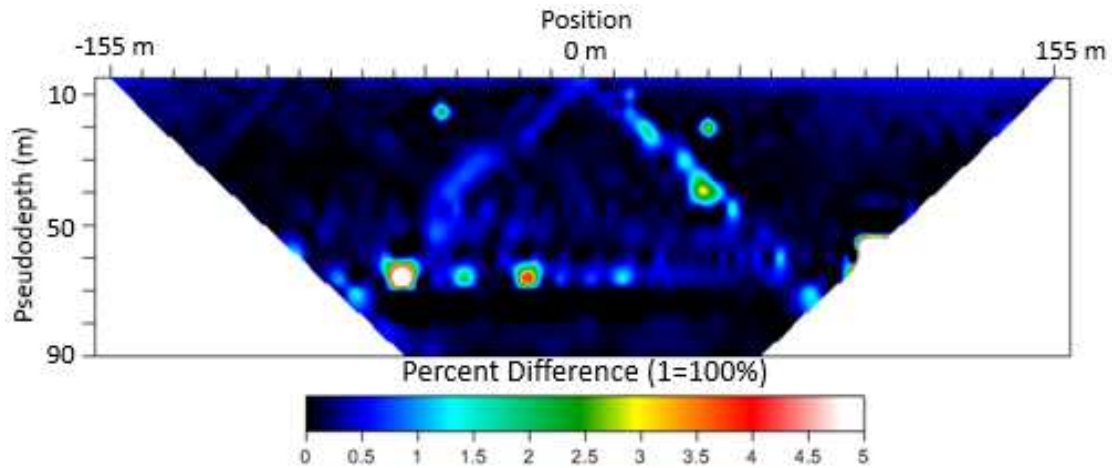


Figure 3.56: Point-by-point percent difference plot produced between the MoM solution and the experimental field data. Maximum discrepancies of ~50% are observed within the zone of secondary response.

Percent differences show a reasonable overall match between field and MoM (Figure 3.56). Several “blobs” of large misfit exist; however, they are isolated and are due to the inhomogeneous Earth, SP noise between transmitter and receiver electrodes, and instrumentation interpolation. The secondary response itself sees no more than ~50% misfit between the experimental and modelled data which is a good starting point for finding a real Earth and casing model that fit the field data. In an effort to improve this fit further I attempted to narrow down any uncertainty within the physical properties of the casings. From the COGCC database I was certain of all dimensional properties, yet an exact electrical conductivity of the steel used in the casing was not given. From running the MoM model at the $8E+06$ S/m seen above we also calculated the solution at $8E+07$ S/m and $8E+05$ S/m which all fit in the possible range of electrical conductivities of steel. RMS errors were calculated between these three solutions with a maximum discrepancy between any pair of the three of 0.287%. Overall fit was not better than that observed in figure 3.56. In figure 3.57 I display the response from the survey perpendicular to that in figure 3.55 and observe a similar response. This helps to cross-check the quality of the first data-set and further displays the quality of the background of the field-site. Although there is less noise in this dataset the linear artifact near pseudodepth of 70 m is still present.

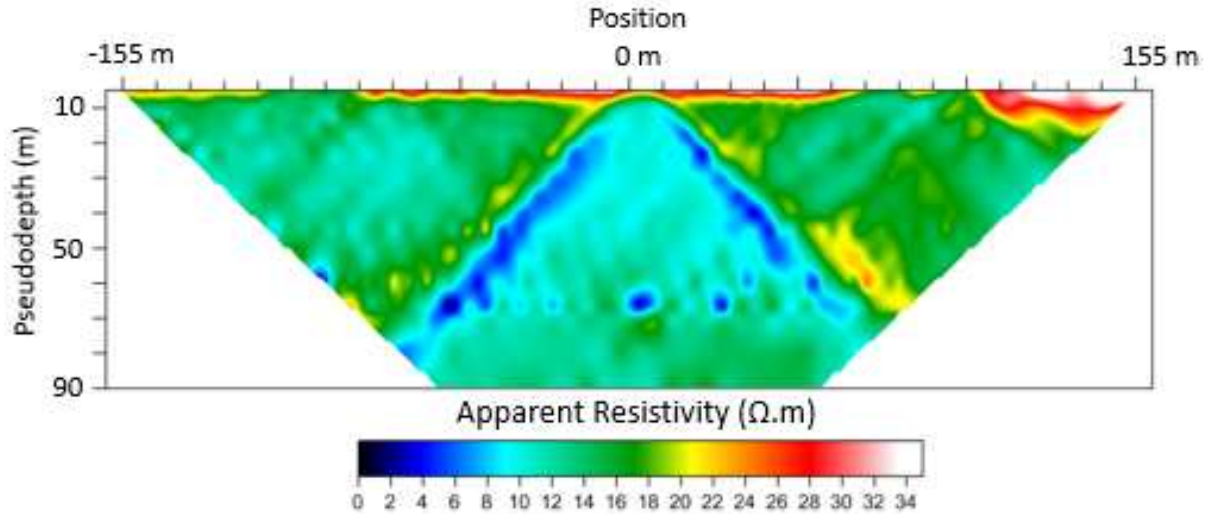


Figure 3.57: Apparent resistivity pseudosection section data collected along line 3 in figure 3.53 over our abandoned steel-cased well.

3.3.2: Large-Scale Experiment Conclusions

The large-scale field work in eastern Colorado provided an opportunity to test the MoM modelling approach against experimental data on a scale approaching that of real field scales that motivated the research carried out in this project and found it to be quite effective. The field site displays a fairly homogeneous background of 15-16 Ωm disregarding subsurface inhomogeneities and noise. Two perpendicular surveys over the abandoned steel-cased well showed similar responses, as we would expect, with maximum drops in apparent resistivity from the background of 74% along the zones of secondary response. A point-by-point percent difference plot created to observe the misfit between the experimental and MoM data shows maximum discrepancies of ~50% along the zones of secondary response, suggesting an overall reasonable match given I have assumed a simple homogeneous background and not carried out any inversion of the field data. Using $RMS = \frac{1}{n} \sqrt{\sum_{i=1}^n (M - R)^2}$ an error of 0.205 for line 1 and 0.209 for line 3 was found between the real and MoM apparent resistivities.

CHAPTER 4

AC MODELLING

4.1 Lab-Scale (Pool) AC Modelling

The added complexity of the AC regime within the pool requires additional tests to be carried out before beginning surveys. Given the scale of the pool environment it is known that a considerably high transmitting frequency may be necessary to observe AC behavior within survey results. This presents a notable issue as the Metronix Geophysics ADU-07e recording device used at Mines has a maximum sampling frequency of ~262 kHz meaning if AC behavior is not reached prior to ~130 kHz (the instruments Nyquist frequency), then the experiment would be impossible to carry out at the lab-scale without the use of a much higher sampling recording device such as appropriate ground-penetrating radar (GPR) instruments. To determine what this frequency may be I have made use of the MoM numerical modelling code to test multiple increasing frequencies and analyze amplitude and phase variations to determine at what frequency range we start seeing AC behavior. These tests are run in the presence of the steel control casing from chapter 3.1.

4.1.1: High Frequency to DC Amplitude Ratios and Phase Difference

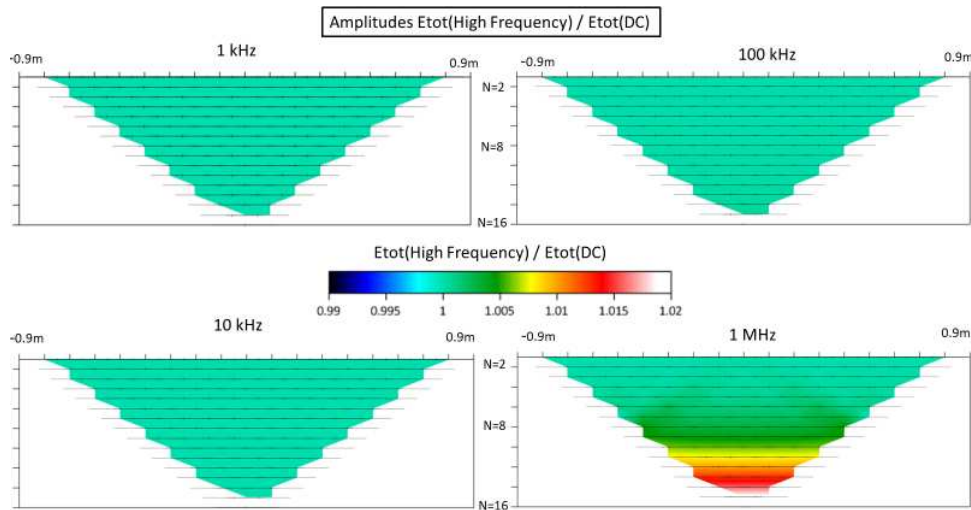


Figure 4.1: Lab-scale $E_{tot}(\text{High Frequency})/E_{tot}(\text{DC})$ amplitudes at full range of tested frequencies.

I begin first by studying ratios of the total electric field amplitudes to the amplitudes of the primary electric fields. When the necessary transmitting frequency is reached I expect to see large amplitude fluctuations laterally within the zone of response. Above I show $E_{tot}(\text{High Frequency})/E_{tot}(\text{DC})$ amplitude plots for frequencies 1kHz, 10 kHz, 100 kHz and 1MHz. From an AC response I would expect amplitude fluctuations within the plots that would show themselves as a fading in and out along the zone of response to a ratio of one and then to near zero. From these plots (Figure 4.1) there are no changes between plots until we reach the MHz range suggesting that the scale of the pool allows to see only near-field components and that we are still in the DC regime at this frequency. To study further I will also investigate the phase difference between $E_{tot}(\text{High Frequency})$ and $E_{tot}(\text{DC})$.

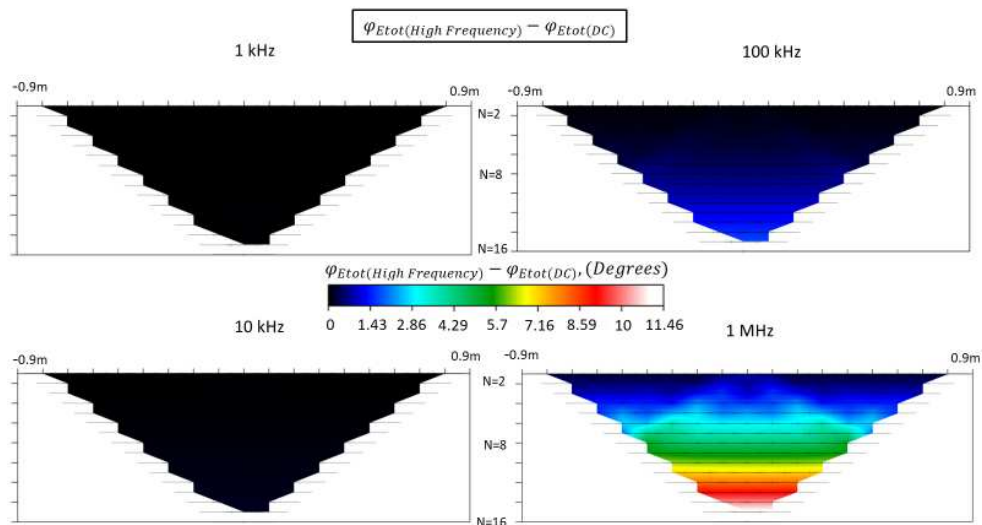


Figure 4.2: Lab-scale phase difference between $E_{tot}(\text{High Frequency})$ and $E_{tot}(\text{DC})$ at full range of tested frequencies.

Here we see little to no phase change with increasing frequency in figure 4.2. At 100 kHz we see nearly 1.4° at depth, at 1 MHz there is a maximum of 11.4° which is a significant level of phase change. Given I have begun to reach the MHz range at this point, however, I would have to use specialized equipment such as GPR data loggers to even record this minimal level AC behavior. To verify this further, I have also split the primary, secondary, and total amplitudes into their own plots and associated phases and analyzed their behavior.

4.1.2: Primary Field Amplitudes and Phase

First, I will examine amplitudes (Figure 4.3) and phases (Figure 4.4) produced by the primary fields alone, again at the same frequencies of 10 Hz, 100 Hz, 1 kHz, 10 kHz, 100 kHz and 1 MHz.

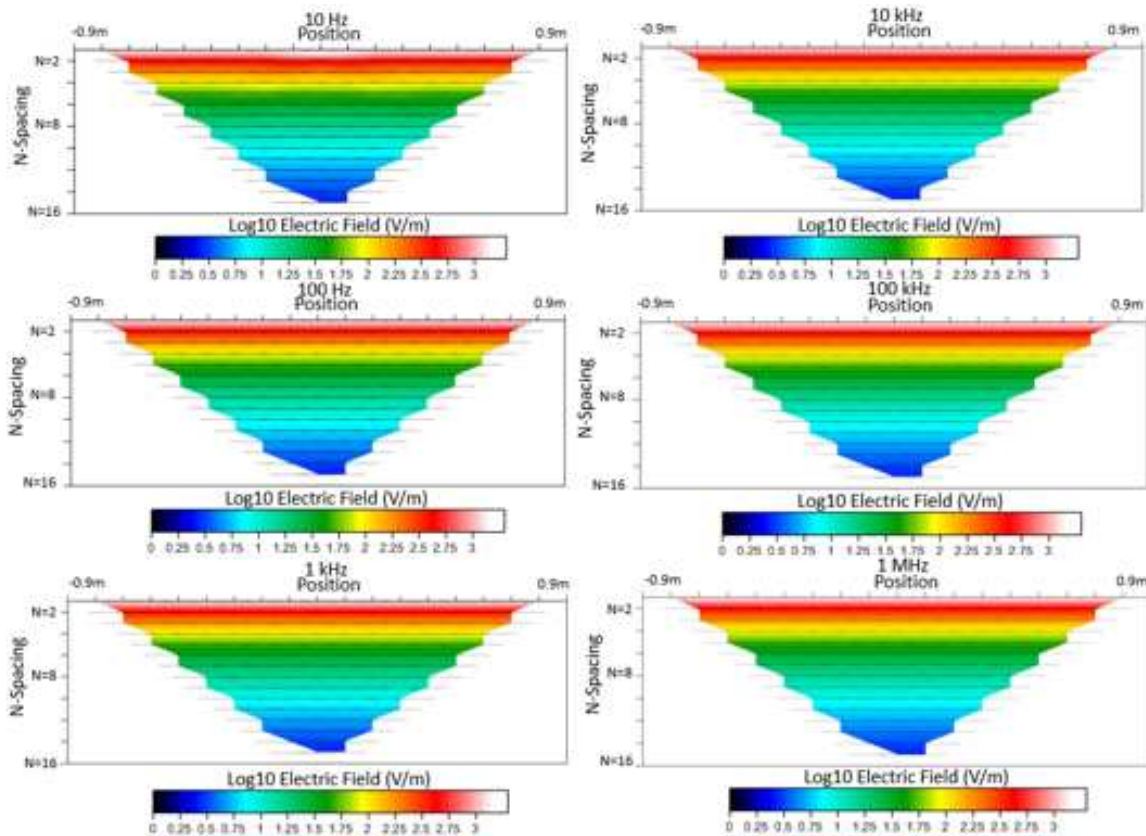


Figure 4.3: Lab-scale log(10) amplitudes of primary field at full range of tested frequencies.

The primary amplitude plots are in log(10) electric field (V/m) due to the wide range of primary field values in comparison to the ratio of E_{tot}/E_p used in section 4.1.1. I again observe no real amplitude fluctuations throughout the plots and see only a steadily decreasing value for primary electric field with pseudodepth, which is what we would expect given larger primary fields at smaller data levels where the transmitter and receiver dipole centers are closest to one another.

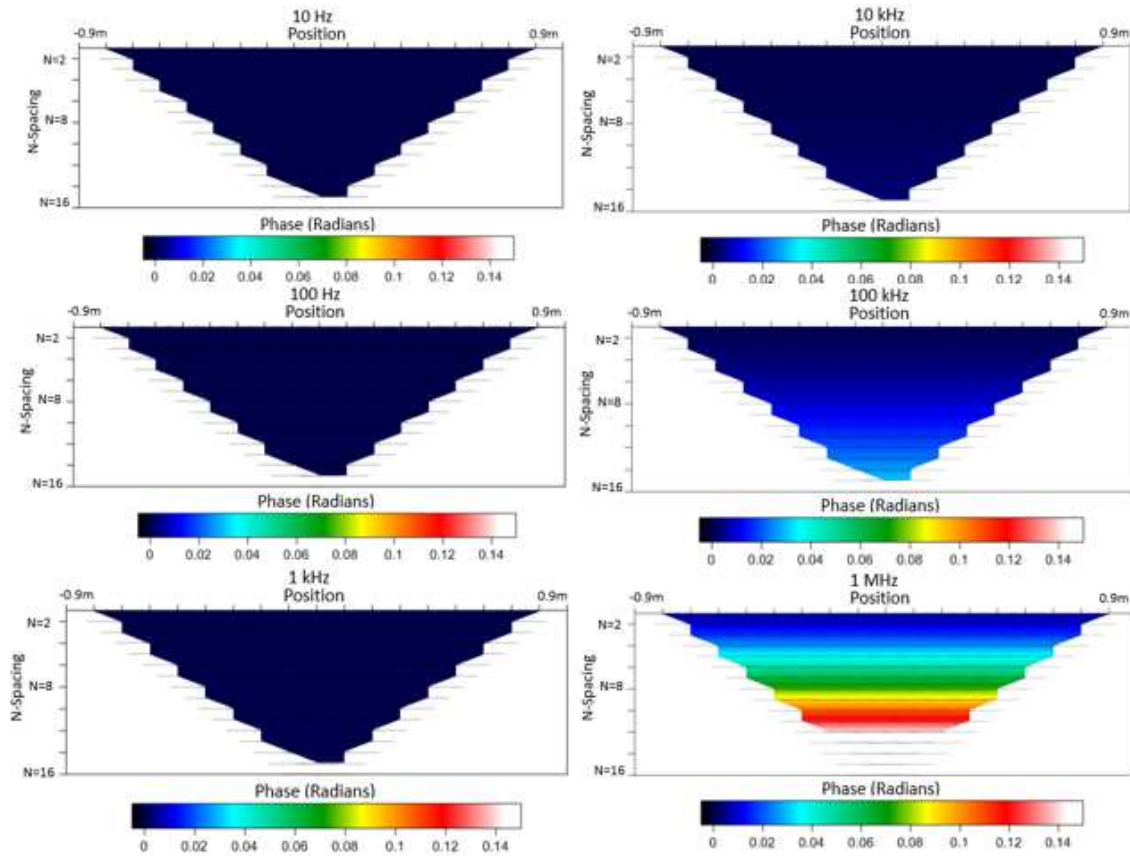


Figure 4.4: Lab-scale phase values in radians of primary field at full range of tested frequencies.

Similarly to what was observed from phase plots of section 4.1.1 I find little to no phase change from the primary fields until I reach the MHz range. Here, as in the case of primary amplitudes, I see the largest values increasing with pseudodepth to a maximum phase change from the primary field of 0.2 radians (i.e. ~ 11.5 degrees) from the surface where the phase is 0 radians.

4.1.3: Secondary Fields Amplitudes and Phase

I will now discuss the amplitudes and phases produced by the secondary fields at the same six frequencies. These fields correspond strictly to the electric field produced from the energized casing.

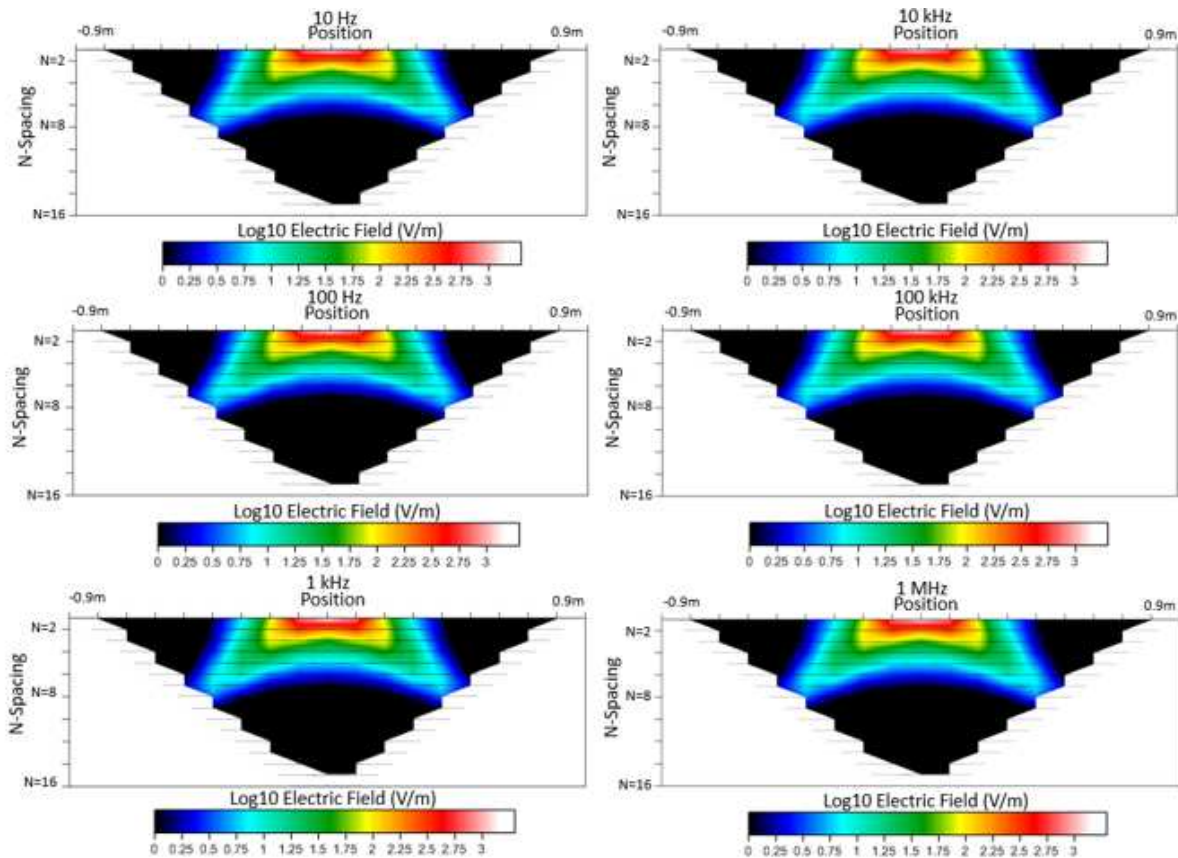


Figure 4.5: Lab-scale log(10) amplitudes of secondary field at full range of tested frequencies.

Again, I show the amplitudes with a log(10) scale of electric fields in V/m (Figure 4.5). Secondary electric amplitudes decay gradually away from the top-center of the pseudo-section, however, it is identical to that of a DC secondary response and shows no signs of AC behavior whatsoever throughout the entire range of frequencies. Next, I will show the phases associated with the secondary fields (Figure 4.6). The trend continues as I study the secondary field phase data. In this case, unlike that of the primary phase plots of section 4.1.2, there is no real phase change from the background of 0.0-0.004 radians until I reach 1 MHz where there is a bowl-shaped phase response spreading outward from the top center of the pseudo-section.

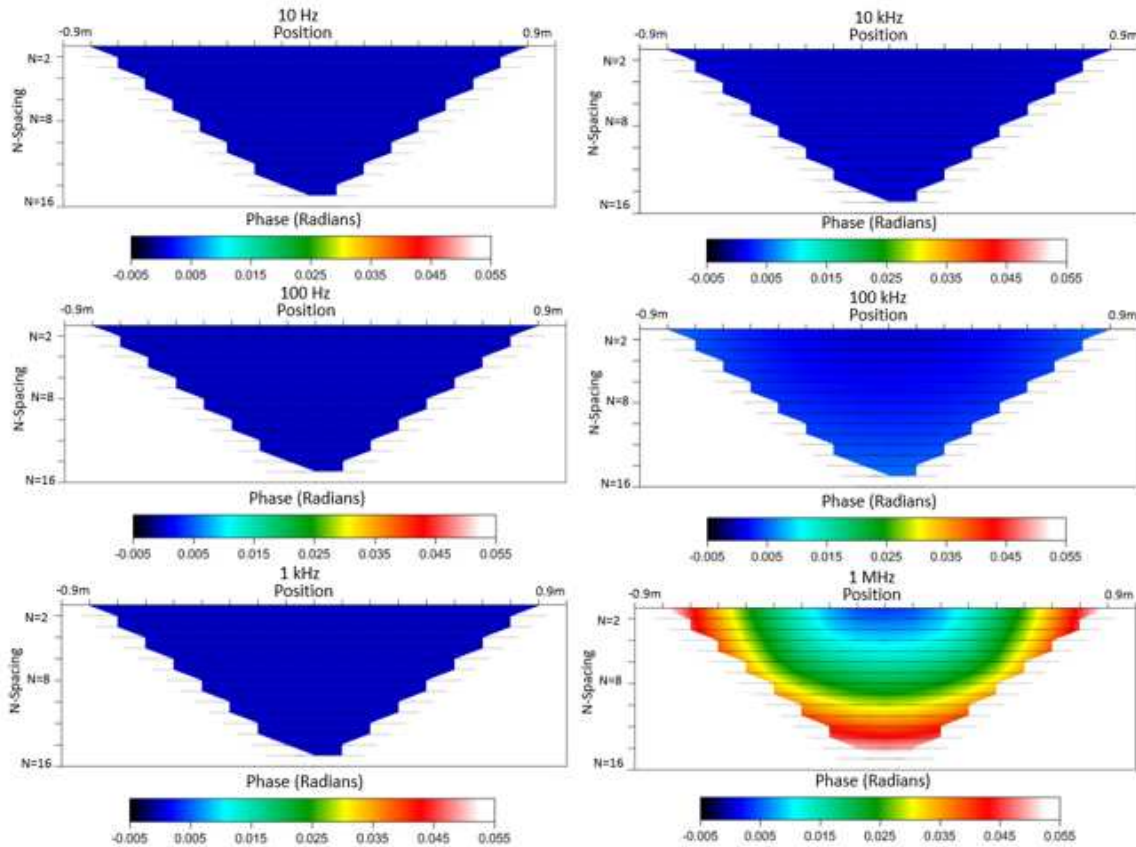


Figure 4.6: Lab-scale phase values in radians of secondary field at full range of tested frequencies.

There are maximum phase changes throughout the plot of only 0.054 radians at the furthest distances from the casing which would hardly be measurable AC behavior.

4.1.4: Total Fields Amplitudes and Phase

Finally, I will analyze amplitude and phase plots created from the total electric fields using the same six frequencies again. The total electric field is simply the sum of both primary and secondary fields discussed previously. I will use the same method of viewing the data at a $\log(10)$ electric field scale for the amplitude plots (Figure 4.7).

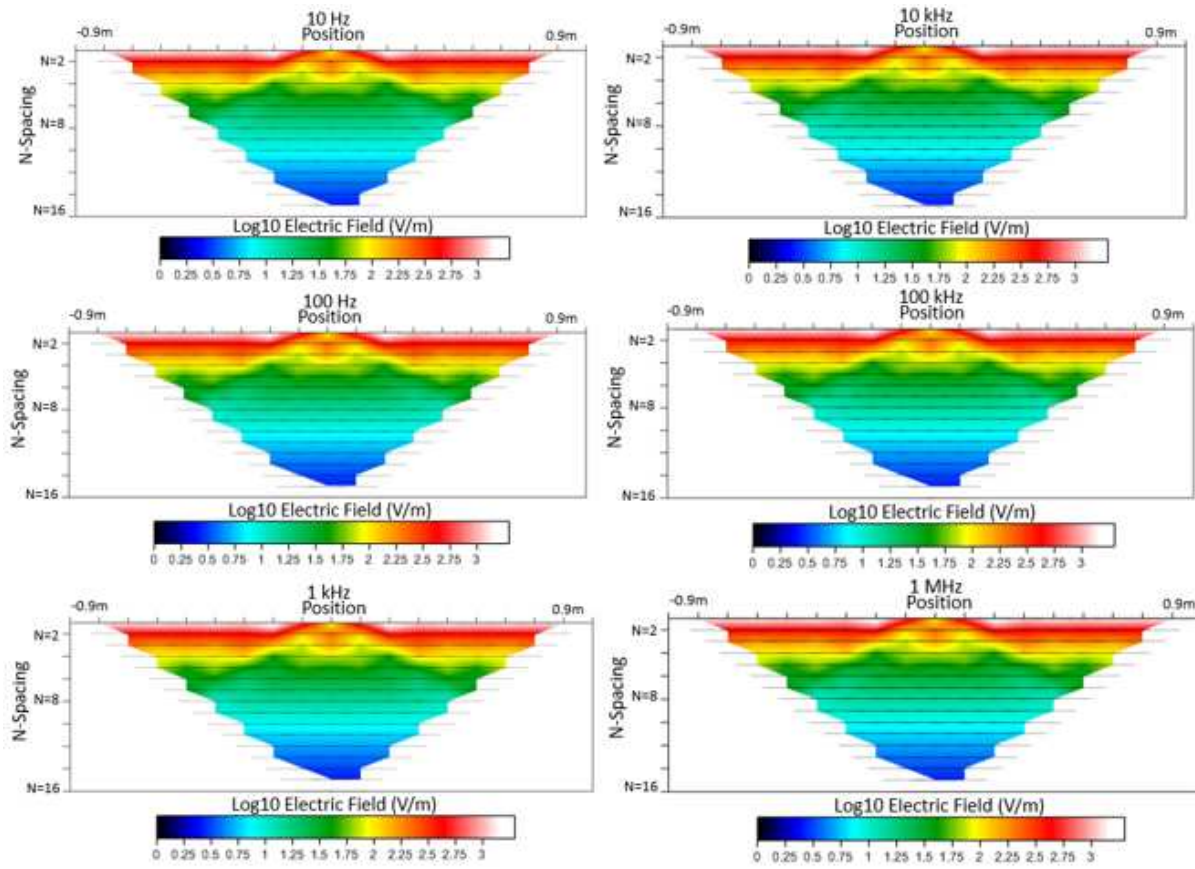


Figure 4.7: Lab-scale log(10) amplitudes of total field at full range of tested frequencies.

It is obvious that the vast majority of the total electric field amplitudes are dominated by the primary field in this case as the largest variations in amplitude occur with data level as observed in section 4.1.2. There is a notable contribution from the secondary field that can be seen in data levels one through five but fades to the primary background at larger pseudodepths. Again, there is no evident amplitude fluctuation throughout the entire range of frequencies. Now, I will discuss the phase changes produced from the total fields (Figure 4.8). Similarly to the amplitudes discussed in this section I expect the phases to be dominated by the primary field contributions. At 1 MHz there is maximum phase changes from the near surface of ~ 0.2 radians at the deepest data level.

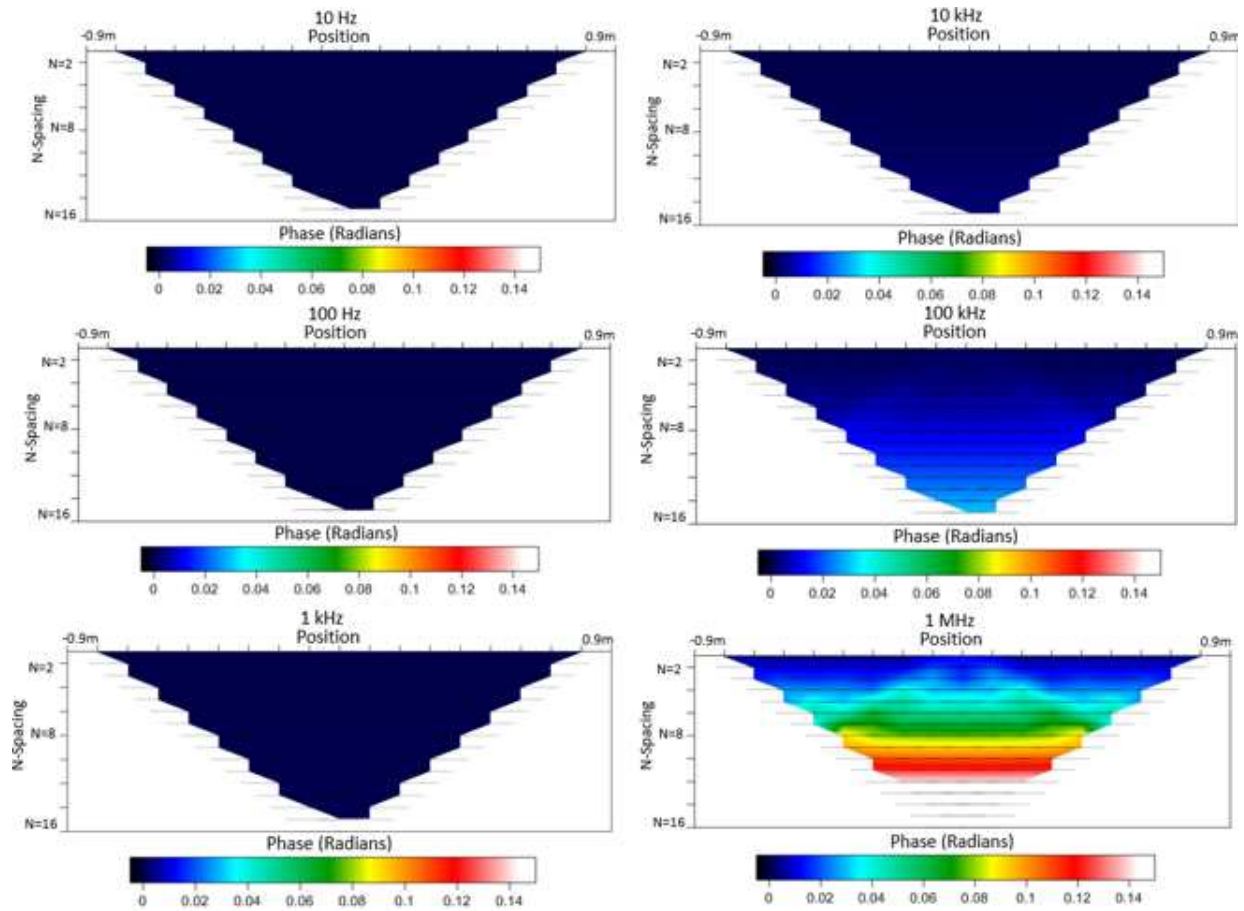


Figure 4.8: Lab-scale phase values in radians of total field at full range of tested frequencies.

It is obvious, as in the amplitude plot analysis, that the phase change is dominated by the primary fields. The secondary field contribution is noticeable but pales in comparison, showing itself only at the top center of the plots. As in the primary field section of 4.1.2 I note that this maximum phase change, though significant, would not be possible to efficiently record the equipment available at CSM.

4.1.5: Lab-Scale (Pool) Conclusions

The small scale of the lab experiment led to questions regarding the efficiency of an AC experiment within the pool, given the spacing of the electrodes and the rather shallow depth of the environment. It was assumed that a very high frequency signal may be necessary to escape the near-field and observe AC behavior in the pool. Considering this, it is necessary to find at what frequency range I enter the AC regime, as CSM's electromagnetic recording device, the

ADU-07e from Metronix Geophysics is capable of sampling only to a frequency of ~262 kHz. Through sections 4.1.1-4.1.4 I have tested for AC behavior in the lab-scale pool experiment at frequencies of 10 Hz, 100 Hz, 1 kHz, 10 kHz, 100 kHz and 1 MHz by analyzing E_{tot}/E_p amplitudes, primary electric field, secondary electric field and total electric field amplitudes as well as phases for the same scenarios. Though at the lab-scale I begin to see some level of AC behavior at 1 MHz, I would not be able to efficiently record such high frequencies without the use of additional equipment such as GPR recorders which would require a much more complex experiment. Considering this it has been decided that lab-scale AC experiments are outside of the scope of this thesis.

4.2: Mid-Scale (Kafadar Commons) AC Modelling

Following the findings from section 4.1 it was decided to also investigate at what frequency ranges AC behavior starts for both mid and large-scales. The results of section 4.1 have shown that potential unseen difficulties may arise from the AC regime and thus gathering as much knowledge about future field work at both larger scales is important. Within this section I will explore the same set of tests conducted at the lab-scale now for the mid-scale AC field experiment on Kafadar Commons. These tests will be held in the presence of a casing with the exact same dimensions as the steel-cased vertical borehole study carried out in section 3.2.1 with a length of 15 m, and outer and inner radii of 0.078 m and 0.062 m respectively. I also make use of the same survey geometry of 20 electrodes spaced at 1 m.

4.2.1: High Frequency to DC Amplitude Ratios and Phase Difference

I will begin in the same manner as in the lab-scale by analyzing amplitude plots created from taking the ratio of the total electric field amplitudes at a high frequency to that of the total electric field amplitudes at 10 Hz. Given the same limit is set on the recorders sampling rate of 262 kHz I will test frequencies of 1 kHz, 10 kHz, 20 kHz, 30 kHz, 40 kHz and 50 kHz.

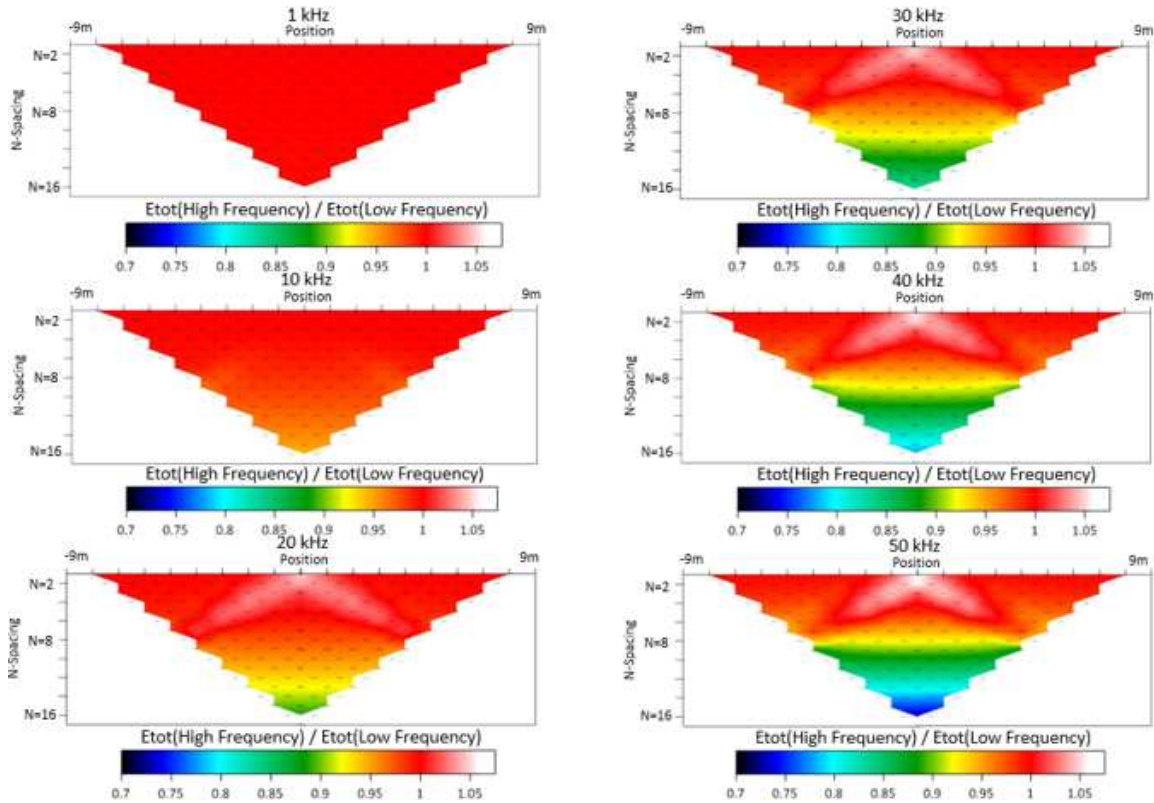


Figure 4.9: Mid-scale $E_{tot}(\text{High Frequency})$ to $E_{tot}(\text{Low Frequency})$ amplitude ratios at full range of tested frequencies.

Like the lab-scale case there is little to no change in the amplitude ratios before 10 kHz in figure 4.9. However, it is immediately obvious, particularly after viewing the lack of AC response at the lab-scale, to observe AC behavior beginning at 10 kHz. In comparison to the continuous $E_{tot}(\text{high frequency})/E_{tot}(\text{low frequency})$ ratio in the 1 kHz case there is clear AC behavior at 10 kHz that continues to increase towards 50 kHz. This shows that I am well within the AC regime for the case of Kafadar Commons by 10 kHz. In addition to observing amplitude fluctuations I will now study the phase difference between $\phi_{total}(\text{High Frequency})$ and $\phi_{total}(\text{Low Frequency})$.

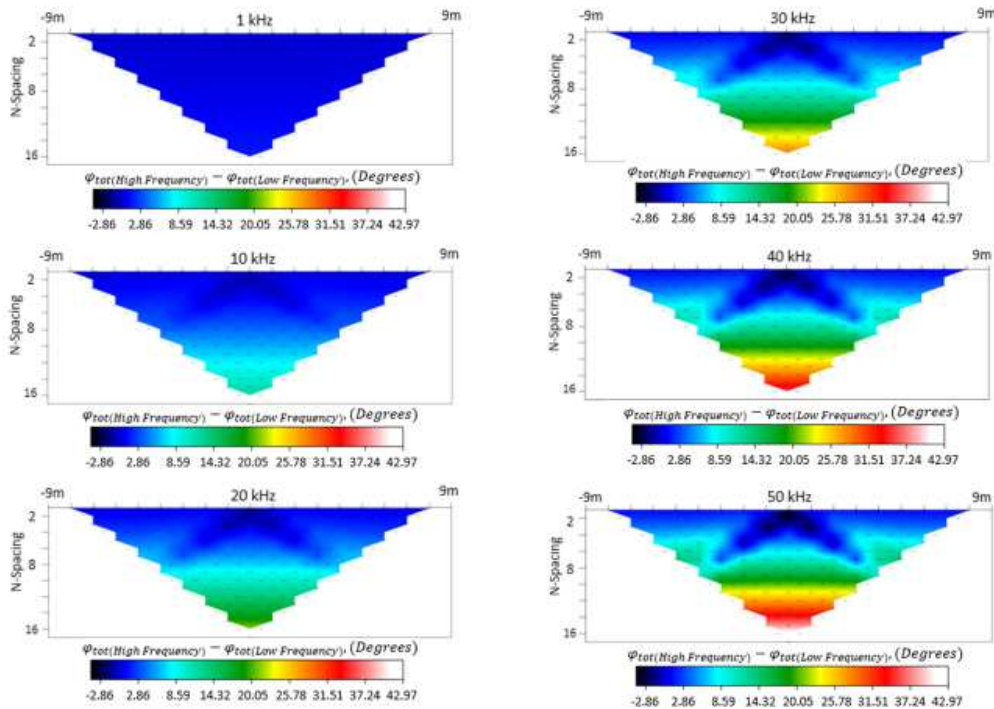


Figure 4.10: Mid-scale phase difference values between $E_{tot}(\text{High Frequency})$ and $E_{tot}(\text{Low Frequency})$ at full range of tested frequencies.

Similar to what was observed within the amplitude ratio plots, there is little to no significant phase difference throughout the plots until I reach the 10 kHz scale (Figure 4.10) where the AC behavior begins. Large phase shifts begin to take place throughout the section from 20 kHz forward. At 50 kHz there is a max phase change within the zone of secondary response of 0.1 radians (5.7 degrees) and up to 0.65 radians (37.24 degrees) with depth. This means that a mid-scale survey on the CSM campus is highly possible and will fit well within the sampling limits of our ADU-07e

4.2.2: Mid-Scale (Kafadar Commons) Conclusions

Unlike the lab-scale scenario, I observed significant AC behavior on Kafadar Commons. Until 10 kHz there are no real amplitude fluctuations or notable phase differences. However, when I increase the frequency to 10 kHz and beyond there are immediately differences in ratio plots displaying significant AC behavior. Though it was found I am well within the AC regime by 10 kHz we see our strongest AC behavior at 50 kHz. Given CSM's use of a Metronix ADU-07e to record AC signals, which samples to a maximum frequency of 262 kHz meaning a

Nyquist Frequency of 130 kHz, it was concluded that AC experiments on Kafadar Commons are very possible within the range of 10-50 kHz.

4.3: Large-Scale AC Modelling

Moving forward I have one final scenario at which to investigate the bounds of the AC regime. Potentially the most interesting case due to its density of data points, and depth of investigation I will now carry out the same AC tests conducted at the lab and mid-scale level for the largest scale. These tests will be completed with the same survey geometry used in section 3.3 in the presence of a 130 m long vertical steel-cased well with an outer diameter of 0.21 m and an inner diameter of 0.19 m.

4.3.1: High Frequency to DC Amplitude Ratios and Phase Difference

As in both smaller scales I will attempt to find at what frequency we enter the AC regime when considering the large-scale experiment.

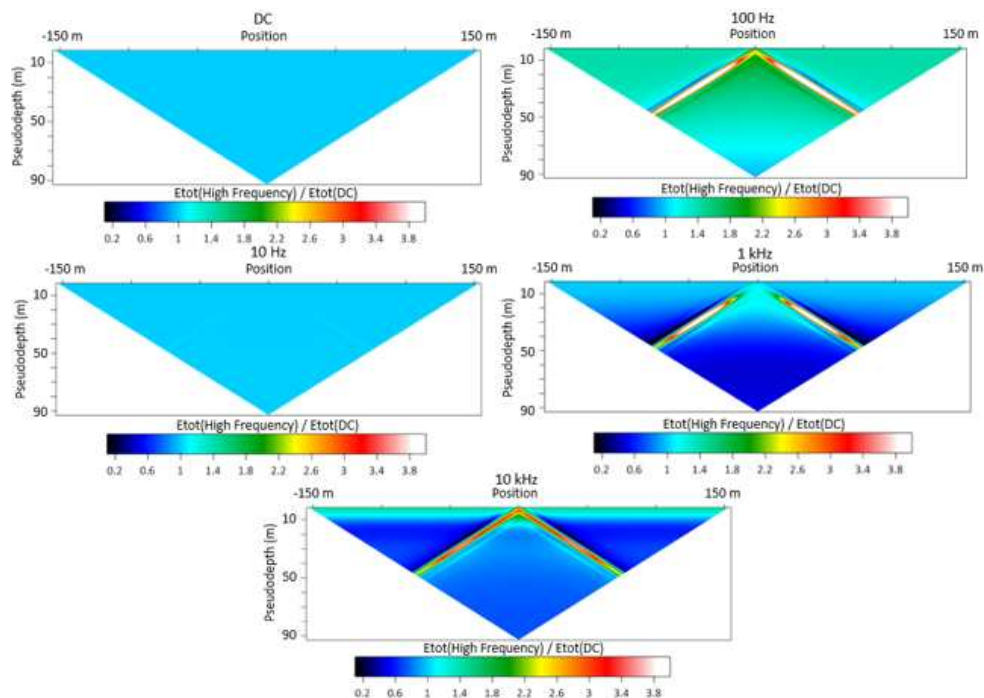


Figure 4.11: Large-scale $E_{tot}(\text{High Frequency})$ to $E_{tot}(\text{DC})$ amplitude ratios at full range of tested frequencies.

I will analyze first plots of E_{tot} (high frequency) to $E_{tot}(DC)$ amplitudes and phase differences (Figure 4.11) between $\phi_{total}(\text{High Frequency})$ and $\phi_{total}(DC)$. For the large-scale I should enter the AC regime sooner than that of our other tests and will therefore test frequencies of 10 Hz, 100 Hz, 1 kHz and 10 kHz. For each frequency I will observe where there are discrepancies from $E_{tot}(\text{High Frequency})/E_{tot}(DC) = 1$ as this means that there are amplitude fluctuations indicative of AC behavior. At the large scale we see the beginnings of AC behavior much earlier than that observed at the two smaller tested scales with some phase change amplitude fluctuations as early as 10 Hz. Although it is mild figure 4.11 shows that we are already observing AC behavior at 10 Hz near pseudodepth 50 m. As I increase frequency another order of magnitude to 100 Hz the AC behavior is abundant showing strong differences from that observed at the DC level showing no amplitude oscillations.

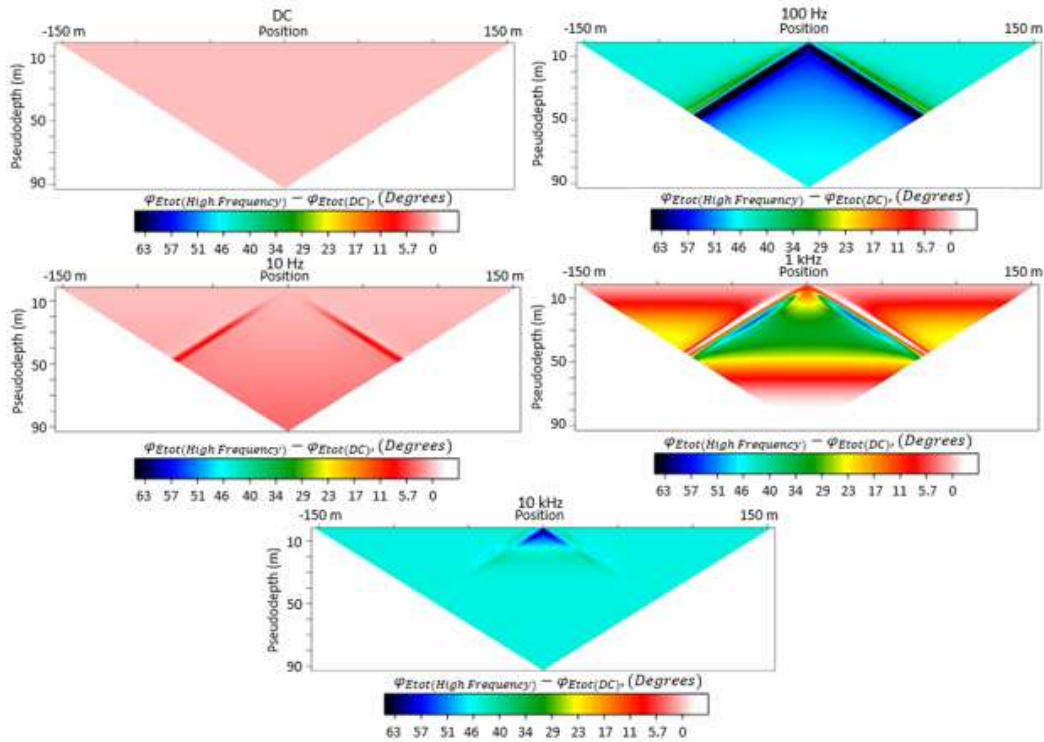


Figure 4.12: Large-scale phase difference between $E_{tot}(\text{High Frequency})$ and $E_{tot}(DC)$ for full range of tested frequencies.

Given the much larger scale of this data there are some very interesting phase plots. There is a small amount of phase difference at depth with our lower frequencies of 10 Hz and as we increasing and order of magnitude there are large lateral phase differences at 100 Hz of ~0.7 radians. At 1 kHz there are large vertical variations in phase and differences within the secondary response zone over 1 radian (~57 degrees).

4.3.2 Large-Scale Conclusions

In the large-scale field work case I found significant amplitude fluctuations as well as phase differences at a much lower frequencies than observed for both lab and mid-scale experiments due to the scale of the large field work. By 100 Hz there were large $E_{tot}(\text{high frequency}) / E_{tot}(\text{DC})$ amplitude fluctuations from, and phase differences. The greater depth of investigation allowed by the longer electrode array in our large-scale field work showed an excellent representation of the relationship between frequency and depth allowing me to see secondary response at deep pseudodepths with low frequencies and very near surface with our higher frequencies. With these studies it was found that large-scale field experiments can be efficiently conducted at a much wider range of frequencies given observed AC behavior at as low as 10 Hz.

CHAPTER 5

CONCLUSIONS

5.1: Summary of Work

Throughout this thesis we have explored a theoretical method of calculating primary and secondary electric fields to help us design our experiments and then understand their results. We have conducted DC resistivity experiments at the lab-scale in our pool where we studied the effects of a variety of different casing orientations, materials and physical dimensions on the secondary responses produced in pseudosections. A mid-scale study was completed on the Colorado School of Mines campus where we made use of a recently constructed underground laboratory to gather DC resistivity data over both a 15 m vertical steel-cased borehole, and an inline survey over a 6 m horizontal aluminum pipe. We presented datasets gathered in eastern Colorado over a full-scale abandoned, steel-cased oil and gas well where two perpendicular DC resistivity surveys were conducted over the well with a third survey offset 250 m from the borehole and parallel to the first showing us the background conductivity structure of the field site. At each scale MoM models were compared to analyze possible sources of misfit with experimental data. Finally, we discussed a series of AC modelling tests at each of our three scales so that future AC experiments may be conducted with prior knowledge of at what frequencies we enter respective AC regimes.

5.2: Conclusions and Speculations

Following initial struggles to conduct successful experiments at the lab-scale a theoretical study into the effects of variations in electric fields with changing casing properties was conducted. One element analytic expressions were derived in chapter 2 for the MoM approach to calculate secondary and primary electric fields. We used these expressions to create plots showing effects of a given change in casing property on the ratio of secondary fields to primary fields. While studying the effects of one casing property, length for example, every other property such as width, wall thickness, and material composition of the casing were kept constant. This allowed us to view the effects of just changing an individual parameter on our results. We compared the results from each test to that of a fully converged 100 element MoM solution to view the legitimacy of the analytic approximation. RMS error values for each test

suggested that though the analytic expressions would not provide exact estimates for values of secondary or primary electric fields, they share similar variations in these fields for certain parameters with lower RMS values. This allowed us to select casings for the experiment that would best represent the changes of these properties in our experimental data. The theoretical study also proved useful at the mid-scale level. We also made use of a DC resistivity finite-element modelling code developed by Thomas Günther of the Leibniz Institute of Applied Geophysics (Günther et al 2017). This allowed us to model the scale of the pool in comparison to a pseudo halfspace to study the resistive edge effects produced by the pool's boundaries. It showed we should expect a drop in apparent resistivity with pseudodepth in the pool of at least 8% but allowed us to understand these effects in our experimental data.

Experimental DC resistivity data collected at the lab, mid, and large-scale provided opportunities to survey a wide variety of casings in many orientations. From experiments, I found that the most important parameters affecting casing responses are the orientation of the casing with respect to survey geometry, total volume of metal present in the casing, and the casing material. Studies of both horizontal and tilted casings found larger secondary responses than generated by vertical casings due to the more efficient electrical coupling between horizontal or subhorizontal targets and the inline electrodes. Maximum drops in apparent resistivity of 42% occur in both horizontal and tilted scenarios compared to the 20% of an identical casing suspended vertically. Studies analyzing casing wall thickness using two otherwise identical casings, one solid and one hollow, produce maximum drops in apparent resistivity of 45% and 20% for the solid and hollow, respectively. This shows that variations in total volume of metal in a target significantly affect secondary response. Surveys were also conducted on casings of identical dimensions made of steel and brass. The higher electrical conductivity of brass led to maximum drops in apparent resistivity of 47% compared to the 20% observed by steel.

To further assess model fit I have conducted an RMS error analysis for each individual experiment at all three scales.

Table 5.1: Table of RMS error values for each experiment at all three scales.

Lab-Scale		RMS		RMS
	Background	0.357	Brass	0.423
	Reference	0.377	Brass Es	0.19
	Reference Es	0.091	Tilted	0.467
	Long	0.296	Horizontal	0.638
	Short	0.327	Vertical + Vertical Near	0.513
	Wide	0.312	Vertical + Vertical Near Es	0.246
	Narrow	0.41	Vertical + Vertical Far	0.408
	Hollow	0.392	Vertical Tilted	0.617
	Hollow Es	0.319	Vertical + Horizontal	0.637
	Solid	0.443	Vertical + Horizontal Es	0.43
	Solid Es	0.322		
Mid-Scale		RMS		RMS
	Vertical	0.183	Horizontal	1.078
	Control	0.295		
Large-Scale		RMS		RMS
	Line 1	0.205	Line 2	0.209
	Control	0.205		

RMS error was calculated using, (3.1). At the lab-scale values have been calculated of ~30-40% for the reference, the longest, the shortest, the narrowest and the widest casings. The reference casing's RMS was decreased to 9.1% by isolating the secondary fields. Hollow, solid and brass casings all have values slightly higher around 40% error. This is likely due to the asymmetry artifact that effects all three of these experiments strongly. The solo tilted and solo horizontal experiments show RMS error values of ~47% and 64%, respectively. A number of potential sources of error may affect these experiments such as inaccuracy in casing depth, imperfect lateral alignment beneath the electrode, and in the tilted case its exact angle from vertical. The dual vertical far case has an RMS value of 40%. The dual vertical near case presents a challenge of constructive interference between the two secondary responses. This likely causes its RMS error value of 50%. When compared the isolated secondary fields of the dual vertical near case an RMS error of 0.246 is found. The vertical-tilted and vertical-horizontal case suffer from the same issues of the solo complex orientation experiments resulting in RMS values of 62% and 64% respectively. Another factor increasing the RMS error values of every pool experiment is the resistive edge effects present at greater pseudodepths. Given the fit within our percent

difference plots in most cases of less than 10% it is likely that we would have very low RMS errors across the board if not for this artifact as was observed in the scenarios where I have subtracted out the primary fields to compare the secondary response between MoM model and experimental data.

In the mid-scale environment, we begin to deal with the true nature of the Earth. The drop in apparent resistivity with depth has been accounted for in both of our models but still produces some level of misfit from not being perfect in its MoM parameters. The vertical steel-cased borehole holds an RMS error of 42%. Factors adding to this value include both the layered Earth as well as the Y-axis offset applied to this model to avoid Hankel integration breakdown. The horizontal aluminum pipe holds the worst RMS error across all scales of experiments of 108%. This is largely due to dimensional uncertainties of the horizontal pipe as well as adjacent buried objects in the M such as the clay pipe discussed.

The large-scale has an RMS error at a value of ~20%. This is due to the excellent conditions of the field site, the absence of edge-effects, and the simple geometry presented by the abandoned well. The COGCC data provided for the well was thorough allowing for good accuracy in dimensional properties for the model. Another factor creating favorable RMS calculations in this case is the small portion of the section that is affected by the casing's secondary response leaving the majority of data points as a simple background which can be modelled very well.

5.3: Future Work

This marks the conclusion of all DC work, both modelled and gathered experimentally, to be completed within the greater project. Future work to be continued directly from this project relate to further modelling studies and the completion of the AC field work at all scales. A greater understanding likely needs to be gathered regarding the interaction of constructively interfering casing responses as seen in the lab-scale dual vertical near example. Consistently lower drops in apparent resistivity were calculated using the fully converged MoM code as opposed to experimental data when analyzing zones where secondary responses interfere and amplify one another.

AC experiments will need to be carried out at all scales in the future, which, as proved here, will be simple in some cases and more complicated in others. For the completion of lab-scale AC experiments it will be necessary to redesign the pool experiment significantly. With the knowledge of the ADU-07e not being able to sample the high frequencies necessary to gather AC data within the pool it is likely that GPR equipment will need to be used. Lab-scale GPR experiments have been conducted in the past such as that from Mangel et al. (2011) who detail efficient methods for experiments using such methods up to 900 MHz. The mid-scale case will be significantly more efficient as it was found that the ADU-07e could record transmission frequencies necessary to enter the AC regime over the 15 m vertical steel-cased borehole. The large-scale AC field work will be simple to achieve as we see AC behavior at as low as 10 Hz which is far beneath any sampling limits imposed by the available equipment.

REFERENCES CITED

- American Ground Water Trust, Well Casing – Steel or plastic, **The American Well Owner**, NO. 4. 2003.
- Baltar, D., and Roth, F., Reserves Estimation from 3D CSEM Inversion for Prospect Risk Analysis, **74th EAGE Conference and Exhibition**, 2012.
- Bateman, H., Tables of Integral Transforms, 2, Bateman manuscript project, **McGraw-Hill Book Company**, 1954.
- Boskovic, Z., Cebasek, V., Nuhanovic, S., Selection casing material depending of wells fluid corrosivity, **Archives for Technical Sciences**, 1(51), 2014
- Constable, S., and L. J. Srnka, An introduction to marine controlled-source electromagnetic methods for hydrocarbon exploration, **Geophysics**, 72, WA3-WA12, 2007.
- Constable, S., Ten years of marine CSEM for hydrocarbon exploration, **Geophysics**, 75, 75A67-75A81, 2010.
- Constable, S., Weiss, C., Mapping thin resistors and hydrocarbons with marine EM methods; insights from 1D modeling, **Geophysics**, 71(2), G43-G51, 2006.
- Cox, C.S., On the electrical conductivity of the oceanic lithosphere, **Phys. Earth Planet. Interiors**, 25(3), 1981, 196-201.
- Dragoset, B., A historical reflection on reflections, **The Leading Edge**, 24, s1, s1-s112, 2015.
- Ellingsrud, S., Eidesmo, T., Johansen, S., Singa, M. C., Macgregor, L. M., Constable, S., Remote sensing of hydrocarbon layers by seabed logging (SBL): Results from a cruise offshore Angola, **The Leading Edge**, 21(10), 945-1064, 2002.
- Filloux, J. H., Techniques and instrumentation for study of natural electromagnetic induction at sea, **Physics of the Earth and Planetary Interiors**, 7(3), 1973, 323-338.
- Frischknecht, F. C., Electromagnetic Physical Scale Modeling, *in* Electromagnetic Methods in Applied Geophysics, **Society of Exploration Geophysicists**, 1, 365-441, 1988.
- Gorujov, G., Anderson, E., Swidinsky, A., Towards modeling the electromagnetic response of complex pipelines using the Method of Moments, **SEG San Antonio 2019 Abstract Submission**, 2019.
- Günther, T., Boundless Electrical Resistivity Tomography BERT 2 – the user tutorial, **Leibniz Institute for Applied Geophysics**, Hannover, 2017.
- Harden, R. W., Fiberglass casing use in Texas Public Supply Wells, **Texas Water Development Board**, 2013.

- Hesthammer, J., Stefatos, A., Boulaenko, M., Fanavoll, S., Danielsen, J., CSEM performance in light of well results, **Leading Edge**, 29(1), 2010, 34-41.
- Holladay, J. S., and G. F. West, Effect of well casings on surface electrical surveys, **Geophysics**, 49, 1984, 177-188.
- Hoogervorst, G. H. T. C., Fundamental noise affecting signal-to-noise ratio of resistivity surveys, **Geophysical Prospecting**, 23(2), 1975, 380-390.
- Kohnke, Colton J., Electromagnetic Effects of Steel-Cased Wells, **Colorado School of Mines**, Arthur Lakes Library, Print, 2017.
- Krahenbuhl, R., Passerella, B., Flamme, H., Crookston, G., Sirota, D., Developing a large underground geophysical education laboratory at Colorado School of Mines, **SEG International Exposition and 88th Annual Meeting**, 2018, 269.
- Landro M. Veire H. H. Duffaut K. Najjar N., Discrimination between pressure and fluid saturation changes from marine multicomponent time-lapse seismic data, **Geophysics** , 68, 2003, 1592–1599.
- Lien, M., Mannseth, T., Sensitivity study of marine CSEM data for reservoir production monitoring, **Geophysics**, 73, 2008, F151-F163.
- Loke, M. H., Res2Dinv ver. 3.59 for Windows XP/Vista/7, 2010. Rapid 2-D resistivity and IP inversion using the least-squares method, **Geoelectrical Imaging 2D & 3D Geotomo Software**, 2010.
- Mangel, A., Moysey, S. M. J., Ryan, J. C., Tarbutton, J. A., Multi-offset Ground-Penetrating Radar imaging of a lab-scale infiltration test, **Hydrology and Earth System Sciences Discussions**, 8, 2011.
- Mittet, R., and Morten, J. P., 2012, Detection and imaging sensitivity of the marine CSEM method, **Geophysics**, 77(6), 2012, E411-E425.
- Morten, J. P., Roth, F., Karlsen, S. A., Timko, D., Pacurar, C., Olsen, P. A., Nguyen, A. K., Gjengedal, J., Ronen, S., Field appraisal and accurate resource estimation from 3D quantitative interpretation of seismic and CSEM data, **Leading Edge**, 31, 2012, 447-456.
- N. Edwards, R. Mir, E. Willoughby, K. Schwalenberg and C. Scholl, The assessment and evolution of offshore gas hydrate deposits using seafloor controlled source electromagnetic methodology, **OCEANS'10 IEEE SYDNEY**, 2010, 1-10.
- Orange, A., Key, K., Constable, S., The feasibility of reservoir monitoring using time-lapse marine CSEM, **Geophysics**, 74(2), 2009, F21-F29.
- Park, J., Fawad, M., Vikem, I., Aker, E., Bjørnarå, T. I., CSEM sensitivity study for Sleipner CO₂-injection monitoring, **Energy Procedia**, 37, 2013, 4199-4206.

- Price, A., Mikkelsen, G., Hamilton, M., 3D CSEM over Frigg – dealing with cultural noise, SEG Technical Program Expanded Abstracts 2010, **Society of Exploration Geophysicists**, 2010, 670-674.
- Rahman, S. S., and Chilingar, George V., Casing Design Theory and Practice, Amsterdam, **Elsevier**, 1995.
- Rücker, C., Günther, T., Spitzer, K., Three-dimensional modelling and inversion of dc resistivity data incorporating topography I. Modelling, **Geophysical Journal International**, 166, 2006, 495-505.
- Schamper, C., F. Rejiba, A. Tabbagh, and S. Spitz, Theoretical analysis of long offset time-lapse frequency domain-controlled source electromagnetic signals using the method of moments: Application to the monitoring of a land oil reservoir, **Journal of Geophysical Research**, 116, 2011, B03101.
- Sinha, M. Patel, P., Unsworth, M., Owen, T., Maccormack, M., Sinha, M., An active source electromagnetic sounding system for marine use, **Marine Geophysical Researches**, 12(1), 1990, 56-68.
- Srnka, J., Method and apparatus for offshore electromagnetic sounding utilizing wavelength effects to determine optimum source and detector positions, **Ocean Engineering**, 14(2), 1987.
- Swidinsky, A., C. Kohnke, and R. N. Edwards, The electromagnetic response of a horizontal electric dipole in a layered medium: A pedagogical perspective **Geophysical Prospecting**, 2016.
- Swidinsky, A., R. N. Edwards, and M. Jegen, The marine controlled source electromagnetic response of a steel borehole casing: applications for the NEPTUNE Canada gas hydrate observatory, **Geophysical Prospecting**, 61, 2013, 842-856.
- Tang, W., Y. Li, A. Swidinsky, and J. Liu, Three-dimensional controlled-source electromagnetic modelling with a well casing as a grounded source: a hybrid method of moments and finite element scheme, **Geophysical Prospecting**, 63, 2015, 1491-1507.
- Vasco D. W. Keers H. Khazanehdari J. Cooke A., Seismic imaging of reservoir flow properties: Resolving water influx and reservoir permeability, **Geophysics** , 73(1), 2008, O1–O13.
- Ward, S. H., and G. W. Hohmann, Electromagnetic Theory for Geophysical Applications, *in* Electromagnetic Methods in Applied Geophysics, **Society of Exploration Geophysicists**, 1, 1988, 130-311.
- Yang, W., C. Torres-Verdin, J. Hou, and Z. I. Zhand, 1D subsurface electromagnetic fields excited by energized steel casing, **Geophysics**, 74, 2009, E159-E180.

Zhenwei, G., Hefend, D., Jianxin, L., Comparison of marine controlled-source electromagnetic data acquisition systems by a reservoir sensitivity index: analyzing the effect of water depths, **Acta Oceanologica Sinica**, 35(11), 2016, 113-119.

Ziolkowski, A., and Wright, D., The Potential of the Controlled Source Electromagnetic Method: A Powerful Tool for Hydrocarbon Exploration, Appraisal, and Reservoir Characterization, **IEEE Signal Processing Magazine**, 29(4), 2012, 36-52.